

## The Vera C. Rubin Observatory Data Preview 1

1  
2  
3  
4  
5  
6  
7  
8  
9  
10  
11  
12  
13  
14  
15  
16  
17  
18  
19  
20  
21  
22  
23  
24  
25  
26  
27  
28  
29  
30  
31  
32  
33  
34  
35  
36  
37  
38  
39  
40  
41  
42  
43  
44  
45  
46  
47  
48  
49

VERA C. RUBIN OBSERVATORY TEAM,<sup>1</sup> TATIANA ACERO-CUELLAR <sup>2</sup> EMILY ACOSTA <sup>1</sup> CHRISTINA L. ADAIR <sup>3</sup>  
PRAKRUTH ADARI <sup>4</sup> JENNIFER K. ADELMAN-McCARTHY <sup>5</sup> ANASTASIA ALEXOV <sup>1</sup> RUSS ALLBERY <sup>1</sup>  
ROBYN ALLSMAN,<sup>1</sup> YUSRA ALSAYYAD <sup>6</sup> JHONATAN AMADO <sup>5</sup> NATHAN AMOUROUX <sup>7</sup> PIERRE ANTILOGUS <sup>8</sup>  
ALEXIS ARACENA ALCAYAGA,<sup>9</sup> GONZALO ARAVENA-ROJAS <sup>9</sup> CLAUDIO H. ARAYA CORTES,<sup>9</sup> ÉRIC AUBOURG <sup>10</sup>  
TIM S. AXELROD <sup>11</sup> JOHN BANOVETZ <sup>12</sup> CARLOS BARRÍA,<sup>9</sup> AMANDA E. BAUER <sup>13</sup> BRIAN J. BAUMAN,<sup>14</sup>  
ELLEN BECHTOL <sup>15</sup> KEITH BECHTOL <sup>1,16</sup> ANDREW C. BECKER <sup>17</sup> VALERIE R. BECKER <sup>18</sup>  
MARK G. BECKETT <sup>19</sup> ERIC C. BELLM <sup>20</sup> PEDRO H. BERNARDINELLI <sup>21</sup> FEDERICA B. BIANCO <sup>2,22,23</sup>  
ROBERT D. BLUM <sup>18</sup> JOANNE BOGART,<sup>24</sup> ADAM BOLTON <sup>3</sup> MICHAEL T. BOOTH,<sup>1</sup> JAMES F. BOSCH <sup>6</sup>  
ALEXANDRE BOUCAUD <sup>25</sup> DOMINIQUE BOUTIGNY <sup>7</sup> ROBERT A. BOVILL,<sup>1</sup> ANDREW BRADSHAW,<sup>3,24</sup>  
JOHAN BREGEON <sup>26</sup> MASSIMO BRESCIA <sup>27</sup> BRIAN J. BRONDEL <sup>28</sup> ALEXANDER BROUGHTON <sup>24</sup>  
AUDREY BUDLONG <sup>29</sup> DIMITRI BUFFAT,<sup>26</sup> RODOLFO CANESTRARI <sup>30</sup> NEVEN CAPLAR <sup>20</sup> JEFFREY L. CARLIN <sup>1</sup>  
ROSS CEBALLO <sup>18</sup> COLIN ORION CHANDLER <sup>31,20,32</sup> CHIHWAY CHANG <sup>33</sup> GLENAVER CHARLES-EMERSON,<sup>1</sup>  
HSIN-FANG CHIANG <sup>3</sup> JAMES CHIANG <sup>24</sup> YUMI CHOI <sup>34</sup> ERIC J. CHRISTENSEN,<sup>9</sup> CHARLES F. CLAVER,<sup>1</sup>  
ANDY W. CLEMENTS,<sup>1</sup> JOSEPH J. COCKRUM,<sup>1</sup> JOHANN COHEN-TANUGI <sup>35</sup> FRANCO COLLEONI,<sup>9</sup> CÉLINE COMBET <sup>26</sup>  
ANDREW J. CONNOLLY <sup>21</sup> JULIO EDUARDO CONSTANZO CORDOVA <sup>9</sup> HANS E CONTRERAS,<sup>9</sup>  
JOHN FRANKLIN CRENSHAW <sup>21</sup> SYLVIE DAGORET-CAMPAGNE <sup>36</sup> SCOTT F. DANIEL,<sup>20</sup> FELIPE DARUICH,<sup>9</sup>  
GUILLAUME DAUBARD <sup>8</sup> GREG DAUES,<sup>37</sup> ERIK DENNIHY <sup>1</sup> STEPHANIE J. H. DEPPE <sup>18</sup> SETH W. DIGEL <sup>3</sup>  
PETER E. DOHERTY,<sup>38</sup> ALEX DRLICA-WAGNER <sup>5</sup> GREGORY P. DUBOIS-FELSMANN <sup>39</sup> FROSSIE ECONOMOU <sup>1</sup>  
ORION EIGER <sup>3,24</sup> LUKAS EISERT <sup>3</sup> ALAN M. EISNER <sup>40</sup> ANTHONY ENGLERT <sup>41</sup> BADEN ERB,<sup>9</sup> JUAN A. FABREGA,<sup>9</sup>  
PARKER FAGRELIUS,<sup>1</sup> KEVIN FANNING <sup>3</sup> ANGELO FAUSTI NETO <sup>1</sup> PETER S. FERGUSON <sup>21,16</sup> AGNÈS FERTÉ <sup>3</sup>  
MERLIN FISHER-LEVINE <sup>42</sup> GLORIA FONSECA ALVAREZ <sup>34</sup> MICHAEL D. FOSS,<sup>3</sup> DOMINIQUE FOUCHEZ <sup>43</sup>  
DAN C. FUCHS <sup>3</sup> SHENMING FU <sup>24</sup> EMMANUEL GANGLER <sup>35</sup> IGOR GAPONENKO,<sup>3</sup> JULEN GARCIA <sup>44</sup>  
JOHN H GATES,<sup>3</sup> RANPAL K. GILL <sup>28</sup> ENRICO GIRO <sup>45</sup> THOMAS GLANZMAN <sup>3</sup> ROBINSON GODOY,<sup>9</sup> IAIN GOODENOW,<sup>1</sup>  
MIRANDA R. GORSUCH <sup>16</sup> MICHELLE GOWER <sup>37</sup> MELISSA L. GRAHAM <sup>20,21</sup> MIKAEL GRANVIK <sup>46,47</sup>  
SARAH GREENSTREET <sup>34</sup> WEN GUAN <sup>12</sup> THIBAUT GUILLEMIN <sup>7</sup> LEANNE P. GUY <sup>9</sup> DIANE HASCALL,<sup>3</sup>  
PATRICK A. HASCALL,<sup>3</sup> AREN NATHANIEL HEINZE <sup>21</sup> FABIO HERNANDEZ <sup>48</sup> KENNETH HERNER <sup>5</sup> ARDIS HERROLD,<sup>1</sup>  
CLARE R. HIGGS <sup>18</sup> JOSHUA HOBLITT <sup>1</sup> ERIN LEIGH HOWARD <sup>20</sup> MINHEE HYUN <sup>9</sup> PATRICK INGRAHAM <sup>11</sup>  
DAVID H. IRVING <sup>18</sup> ŽELJKO IVEZIĆ <sup>1,20</sup> SUZANNE H. JACOBY,<sup>1</sup> BUELL T. JANNUZI <sup>49</sup> SREEVANI JARUGULA <sup>5</sup>  
M. JAMES JEE <sup>50,51</sup> TIM JENNESS <sup>1</sup> TOBY C. JENNINGS <sup>3</sup> ANDREA JEREMIE <sup>7</sup> GARRETT JERNIGAN,<sup>52,\*</sup>  
DAVID JIMÉNEZ MEJÍAS,<sup>9</sup> ANTHONY S. JOHNSON <sup>3</sup> R. LYNNE JONES <sup>20</sup> ROGER WILLIAM LEWIS JONES <sup>53</sup>  
CLAIRE JURAMY-GILLES <sup>8</sup> MARIO JURIC <sup>21</sup> STEVEN M. KAHN <sup>54</sup> J. BRYCE KALMBACH <sup>3</sup> YIJUNG KANG <sup>24,9</sup>  
ARUN KANNAWADI <sup>55,6</sup> JEFFREY P. KANTOR,<sup>1</sup> EDWARD KARAVAKIS <sup>12</sup> KSHITIJA KELKAR <sup>9</sup> LEE S. KELVIN <sup>6</sup>  
IVAN V. KOTOV,<sup>12</sup> GÁBOR KOVÁCS <sup>21</sup> MIKOLAJ KOWALIK <sup>37</sup> VICTOR L. KRABBENDAM,<sup>1</sup> K. SIMON KRUGHOFF <sup>1,\*</sup>  
PETR KUBÁNEK <sup>9</sup> JACOB A. KURLANDER <sup>21</sup> MILE KUSULJA,<sup>26</sup> CRAIG S. LAGE <sup>51</sup> PAULO J. A. LAGO <sup>28</sup>  
KATHERINE LALIOSIS <sup>56</sup> TRAVIS LANGE <sup>3</sup> DIDIER LAPORTE,<sup>8</sup> RYAN M. LAU <sup>34</sup> JUAN CARLOS LAZARTE,<sup>3</sup>  
QUENTIN LE BOULC'H <sup>48</sup> PIERRE-FRANÇOIS LÉGET <sup>6</sup> LAURENT LE GUILLOU <sup>8</sup> BENJAMIN LEVINE <sup>4</sup> MING LIANG,<sup>1</sup>  
SHUANG LIANG,<sup>3</sup> KIAN-TAT LIM <sup>3</sup> ANJA VON DER LINDEN <sup>4</sup> HUAN LIN <sup>5</sup> MARGAUX LOPEZ <sup>3</sup>  
JUAN J. LOPEZ TORO,<sup>9</sup> PETER LOVE,<sup>53</sup> ROBERT H. LUPTON <sup>6</sup> NATE B. LUST <sup>6</sup> LAUREN A. MACARTHUR <sup>6</sup>  
SEAN PATRICK MACBRIDE <sup>57</sup> GREG M. MADEJSKI,<sup>24</sup> GABRIELE MAINETTI <sup>48</sup> STEVEN J. MARGHEIM <sup>28</sup>  
THOMAS W. MARKIEWICZ <sup>3</sup> PHIL MARSHALL <sup>3</sup> STUART MARSHALL,<sup>24</sup> GUIDO MAULEN,<sup>9</sup> MORGAN MAY,<sup>58,12</sup>  
JEREMY McCORMICK <sup>3</sup> DAVID MCKAY <sup>59</sup> ROBERT MCKERCHER,<sup>1</sup> GUILLEM MEGIAS HOMAR <sup>60</sup>  
AARON M. MEISNER <sup>34</sup> FELIPE MENANTEAU,<sup>37</sup> HEATHER R. MENTZER <sup>40</sup> KRISTEN METZGER,<sup>18</sup>  
JOSHUA E. MEYERS <sup>24</sup> MICHELLE MILLER,<sup>34</sup> DAVID J. MILLS,<sup>1</sup> JOACHIM MOEYENS <sup>21</sup> MARC MONIEZ,<sup>36</sup>  
FRED E. MOOLEKAMP <sup>61</sup> C. A. L. MORALES MARÍN <sup>9</sup> FRITZ MUELLER <sup>3</sup> JAMES R. MULLANEY <sup>62</sup>  
FREDDY MUÑOZ ARANCIBIA,<sup>1</sup> KATE NAPIER <sup>24</sup> HOMER NEAL,<sup>3</sup> ERIC H. NEILSEN, JR. <sup>5</sup> JEREMY NEVEU <sup>36</sup>  
TIMOTHY NOBLE,<sup>63</sup> ERFAN NOURBAKHSH <sup>6</sup> KNUT OLSEN <sup>34</sup> WILLIAM O'MULLANE <sup>9</sup> DMITRY ONOPRIENKO,<sup>3</sup>  
MARCO ORIUNNO <sup>3</sup> SHAWN OSIER,<sup>3</sup> RUSSELL E. OWEN,<sup>20</sup> AASHAY PAI <sup>33</sup> JOHN K. PAREJKO <sup>20</sup> HYE YUN PARK <sup>55</sup>  
JAMES B. PARSONS,<sup>37,\*</sup> MARIA T. PATTERSON <sup>20</sup> MARINA S. PAVLOVIC <sup>9</sup> KARLA PEÑA RAMÍREZ <sup>9</sup>

Corresponding author: Leanne P. Guy; Tim Jenness; James Mullaney

JOHN R. PETERSON <sup>64</sup>, STEPHEN R. PIETROWICZ <sup>37</sup>, ANDRÉS A. PLAZAS MALAGÓN <sup>3,24</sup>, REBEKAH POLEN,<sup>55</sup>  
 HANNAH MARY MARGARET POLLEK,<sup>3</sup> PAUL A. PRICE <sup>6</sup>, BRUNO C. QUINT <sup>1</sup>, JOSÉ MIGUEL QUINTERO MARIN,<sup>9</sup>  
 MARKUS RABUS <sup>65</sup>, BENJAMIN RACINE <sup>43</sup>, VELJKO RADEKA,<sup>12</sup> MANON RAMEL,<sup>26</sup> ARIANNA RANABHAT <sup>66</sup>,  
 ANDREW P. RASMUSSEN <sup>24</sup>, DAVID A. RATHFELDER,<sup>67</sup> MEREDITH L. RAWLS <sup>20,21</sup>, SOPHIE L. REED <sup>6</sup>,  
 KEVIN A. REIL <sup>3</sup>, DAVID J. REISS,<sup>20</sup> MICHAEL A. REUTER <sup>1</sup>, TIAGO RIBEIRO <sup>1</sup>, MICKAEL RIGAUT <sup>68</sup>,  
 VINCENT J. RIOT <sup>14</sup>, STEVEN M. RITZ <sup>40</sup>, MARIO F. RIVERA RIVERA,<sup>9</sup> BRANT E. ROBERTSON <sup>40</sup>,  
 WILLIAM ROBY <sup>39</sup>, GABRIELE RODEGHIERO <sup>69</sup>, AARON ROODMAN <sup>24</sup>, LUCA ROSIGNOLI <sup>70,69</sup>, CÉCILE ROUCELLE <sup>25</sup>,  
 MATTHEW R. RUMORE <sup>12</sup>, STEFANO RUSSO,<sup>8</sup> ELI S. RYKOFF <sup>24</sup>, ANDREI SALNIKOV <sup>3</sup>, BRUNO O. SÁNCHEZ <sup>43</sup>,  
 DAVID SANMARTIM <sup>9</sup>, CLARE SAUNDERS <sup>6</sup>, RAFE H. SCHINDLER,<sup>24</sup> SAMUEL J. SCHMIDT <sup>51</sup>, JACQUES SEBAG,<sup>9</sup>  
 NIMA SEDAGHAT <sup>20</sup>, BRIAN SELVY,<sup>1</sup> EDGARD ESTEBAN SEPULVEDA VALENZUELA,<sup>9</sup> GONZALO SERICHE <sup>9</sup>,  
 JACQUELINE C. SERON-NAVARRETE <sup>9</sup>, IGNACIO SEVILLA-NOARBE <sup>71</sup>, ALYSHA SHUGART <sup>9</sup>, JONATHAN SICK <sup>72,1</sup>,  
 CRISTIÁN SILVA <sup>9</sup>, MATHEW C. SIMS <sup>73</sup>, JALADH SINGHAL <sup>39</sup>, KEVIN BENJAMIN SIRUNO,<sup>9</sup> COLIN T. SLATER <sup>20</sup>,  
 BRIANNA M. SMART <sup>20</sup>, ADAM SNYDER <sup>51</sup>, CHRISTINE SOLDAHL,<sup>3</sup> IOANA SOTUELA ELORRIAGA <sup>9</sup>, BRIAN STALDER <sup>1</sup>,  
 HERNAN STOCKEBRAND <sup>9</sup>, ALAN L. STRAUSS <sup>18</sup>, MICHAEL A. STRAUSS <sup>6</sup>, KRZYSZTOF SUBERLAK <sup>20</sup>,  
 IAN S. SULLIVAN <sup>20</sup>, JOHN D. SWINBANK <sup>74,6</sup>, DIEGO TAPIA <sup>9</sup>, ALESSIO TARANTO <sup>69,70</sup>, DAN S. TARANU <sup>6</sup>,  
 JOHN GREGG THAYER <sup>3</sup>, SANDRINE THOMAS <sup>1</sup>, ADAM J. THORNTON <sup>1</sup>, ROBERTO TIGHE,<sup>9</sup>  
 LAURA TORIBIO SAN CIPRIANO,<sup>71</sup> TE-WEI TSAI <sup>1</sup>, DOUGLAS L. TUCKER <sup>5</sup>, MAX TURRI,<sup>3</sup> J. ANTHONY TYSON <sup>51</sup>,  
 ELANA K. URBACH <sup>75</sup>, YOUSUKE UTSUMI <sup>76</sup>, BRIAN VAN KLAVEREN,<sup>3</sup> WOUTER VAN REEVEN <sup>9</sup>,  
 PETER ANTHONY VAUCHER <sup>3</sup>, PAULINA VENEGAS,<sup>9</sup> APRAJITA VERMA <sup>77</sup>, ANTONIA SIERRA VILLARREAL <sup>3</sup>,  
 STELIOS VOUTSINAS <sup>1</sup>, CHRISTOPHER W. WALTER <sup>55</sup>, YUANKUN (DAVID) WANG <sup>21</sup>, CHRISTOPHER Z. WATERS <sup>6</sup>,  
 CHRISTINA C. WILLIAMS <sup>34</sup>, BETH WILLMAN <sup>78</sup>, MATTHIAS WITTGEN <sup>3</sup>, W. M. WOOD-VASEY <sup>79</sup>, WEI YANG <sup>3</sup>,  
 ZHAOYU YANG <sup>12</sup>, BRIAN P. YANNY <sup>5</sup>, PETER YOACHIM <sup>20</sup>, TIANQING ZHANG <sup>79</sup> AND CONGHAO ZHOU <sup>40</sup>

<sup>1</sup>Vera C. Rubin Observatory Project Office, 950 N. Cherry Ave., Tucson, AZ 85719, USA

<sup>2</sup>Department of Physics and Astronomy, University of Delaware, Newark, DE 19716-2570, USA

<sup>3</sup>SLAC National Accelerator Laboratory, 2575 Sand Hill Rd., Menlo Park, CA 94025, USA

<sup>4</sup>Department of Physics and Astronomy, Stony Brook University, Stony Brook, NY 11794, USA

<sup>5</sup>Fermi National Accelerator Laboratory, P. O. Box 500, Batavia, IL 60510, USA

<sup>6</sup>Department of Astrophysical Sciences, Princeton University, Princeton, NJ 08544, USA

<sup>7</sup>Université Savoie Mont-Blanc, CNRS/IN2P3, LAPP, 9 Chemin de Bellevue, F-74940 Annecy-le-Vieux, France

<sup>8</sup>Sorbonne Université, Université Paris Cité, CNRS/IN2P3, LPNHE, 4 place Jussieu, F-75005 Paris, France

<sup>9</sup>Vera C. Rubin Observatory, Avenida Juan Cisternas #1500, La Serena, Chile

<sup>10</sup>Université Paris Cité, CNRS/IN2P3, CEA, APC, 4 rue Elsa Morante, F-75013 Paris, France

<sup>11</sup>Steward Observatory, The University of Arizona, 933 N. Cherry Ave., Tucson, AZ 85721, USA

<sup>12</sup>Brookhaven National Laboratory, Upton, NY 11973, USA

<sup>13</sup>Yerkes Observatory, 373 W. Geneva St., Williams Bay, WI 53191, USA

<sup>14</sup>Lawrence Livermore National Laboratory, 7000 East Avenue, Livermore, CA 94550, USA

<sup>15</sup>Wisconsin IceCube Particle Astrophysics Center, University of Wisconsin—Madison, Madison, WI 53706, USA

<sup>16</sup>Department of Physics, University of Wisconsin-Madison, Madison, WI 53706, USA

<sup>17</sup>Amazon Web Services, Seattle, WA 98121, USA

<sup>18</sup>Vera C. Rubin Observatory/NSF NOIRLab, 950 N. Cherry Ave., Tucson, AZ 85719, USA

<sup>19</sup>Institute for Astronomy, University of Edinburgh, Royal Observatory, Blackford Hill, Edinburgh EH9 3HJ, UK

<sup>20</sup>University of Washington, Dept. of Astronomy, Box 351580, Seattle, WA 98195, USA

<sup>21</sup>Institute for Data-intensive Research in Astrophysics and Cosmology, University of Washington, 3910 15th Avenue NE, Seattle, WA 98195, USA

<sup>22</sup>Joseph R. Biden, Jr., School of Public Policy and Administration, University of Delaware, Newark, DE 19717 USA

<sup>23</sup>Data Science Institute, University of Delaware, Newark, DE 19717 USA

<sup>24</sup>Kavli Institute for Particle Astrophysics and Cosmology, SLAC National Accelerator Laboratory, 2575 Sand Hill Rd., Menlo Park, CA 94025, USA

<sup>25</sup>Université Paris Cité, CNRS/IN2P3, APC, 4 rue Elsa Morante, F-75013 Paris, France

<sup>26</sup>Université Grenoble Alpes, CNRS/IN2P3, LPSC, 53 avenue des Martyrs, F-38026 Grenoble, France

<sup>27</sup>Department of Physics "E. Pancini", University Federico II of Napoli, Via Cintia, 80126 Napoli, Italy

<sup>28</sup>Vera C. Rubin Observatory/NSF NOIRLab, Casilla 603, La Serena, Chile

<sup>29</sup>University of Washington, Dept. of Physics, Box 351580, Seattle, WA 98195, USA

<sup>30</sup>INAF Istituto di Astrofisica Spaziale e Fisica Cosmica di Palermo, Via Ugo la Malfa 153, 90146, Palermo, Italy

<sup>31</sup>LSST Interdisciplinary Network for Collaboration and Computing, Tucson, USA

<sup>32</sup>Department of Astronomy and Planetary Science, Northern Arizona University, P.O. Box 6010, Flagstaff, AZ 86011, USA

- 106 <sup>33</sup>*Department of Astronomy and Astrophysics, University of Chicago, 5640 South Ellis Avenue, Chicago, IL 60637, USA*  
 107 <sup>34</sup>*NSF NOIRLab, 950 N. Cherry Ave., Tucson, AZ 85719, USA*
- 108 <sup>35</sup>*Université Clermont Auvergne, CNRS/IN2P3, LPCA, 4 Avenue Blaise Pascal, F-63000 Clermont-Ferrand, France*  
 109 <sup>36</sup>*Université Paris-Saclay, CNRS/IN2P3, IJCLab, 15 Rue Georges Clemenceau, F-91405 Orsay, France*  
 110 <sup>37</sup>*NCSA, University of Illinois at Urbana-Champaign, 1205 W. Clark St., Urbana, IL 61801, USA*  
 111 <sup>38</sup>*Smithsonian Astrophysical Observatory, 60 Garden St., Cambridge MA 02138, USA*  
 112 <sup>39</sup>*Caltech/IPAC, California Institute of Technology, MS 100-22, Pasadena, CA 91125-2200, USA*
- 113 <sup>40</sup>*Santa Cruz Institute for Particle Physics and Physics Department, University of California–Santa Cruz, 1156 High St., Santa Cruz,*  
 114 *CA 95064, USA*
- 115 <sup>41</sup>*Department of Physics, Brown University, 182 Hope Street, Providence, RI 02912, USA*
- 116 <sup>42</sup>*D4D CONSULTING LTD., Suite 1 Second Floor, Everdene House, Deansleigh Road, Bournemouth, UK BH7 7DU*  
 117 <sup>43</sup>*Aix Marseille Université, CNRS/IN2P3, CPPM, 163 avenue de Luminy, F-13288 Marseille, France*  
 118 <sup>44</sup>*C. Iñaki Goenaga, 5, 20600, Guipúzcoa, Spain*
- 119 <sup>45</sup>*INAF Osservatorio Astronomico di Trieste, Via Giovan Battista Tiepolo 11, 34143, Trieste, Italy*  
 120 <sup>46</sup>*Department of Physics, P.O. Box 64, 00014 University of Helsinki, Finland*
- 121 <sup>47</sup>*Asteroid Engineering Laboratory, Luleå University of Technology, Box 848, SE-981 28 Kiruna, Sweden*  
 122 <sup>48</sup>*CNRS/IN2P3, CC-IN2P3, 21 avenue Pierre de Coubertin, F-69627 Villeurbanne, France*
- 123 <sup>49</sup>*University of Arizona, Department of Astronomy and Steward Observatory, 933 N. Cherry Ave, Tucson, AZ 85721, USA*  
 124 <sup>50</sup>*Department of Astronomy, Yonsei University, 50 Yonsei-ro, Seoul 03722, Republic of Korea*  
 125 <sup>51</sup>*Physics Department, University of California, One Shields Avenue, Davis, CA 95616, USA*  
 126 <sup>52</sup>*Space Sciences Lab, University of California, 7 Gauss Way, Berkeley, CA 94720-7450, USA*  
 127 <sup>53</sup>*Lancaster University, Lancaster, UK*
- 128 <sup>54</sup>*Physics Department, University of California, 366 Physics North, MC 7300 Berkeley, CA 94720, USA*  
 129 <sup>55</sup>*Department of Physics, Duke University, Durham, NC 27708, USA*
- 130 <sup>56</sup>*Center for Cosmology and Astro-Particle Physics, The Ohio State University, Columbus, OH 43210, USA*  
 131 <sup>57</sup>*Physik-Institut, University of Zurich, Winterthurerstrasse 190, 8057 Zurich, Switzerland*  
 132 <sup>58</sup>*Department of Physics Columbia University, New York, NY 10027, USA*  
 133 <sup>59</sup>*EPCC, University of Edinburgh, 47 Potterrow, Edinburgh, EH8 9BT, UK*
- 134 <sup>60</sup>*Division of Physics, Mathematics and Astronomy, California Institute of Technology, Pasadena, CA 91125, USA*  
 135 <sup>61</sup>*soZen Inc., 105 Clearview Dr, Penfield, NY 14526*
- 136 <sup>62</sup>*Astrophysics Research Cluster, School of Mathematical and Physical Sciences, University of Sheffield, Sheffield, S3 7RH, United*  
 137 *Kingdom*
- 138 <sup>63</sup>*Science and Technology Facilities Council, Rutherford Appleton Laboratory, Harwell, UK*
- 139 <sup>64</sup>*Department of Physics and Astronomy, Purdue University, 525 Northwestern Ave., West Lafayette, IN 47907, USA*
- 140 <sup>65</sup>*Departamento de Matemática y Física Aplicadas, Facultad de Ingeniería, Universidad Católica de la Santísima Concepción, Alonso de*  
 141 *Rivera 2850, Concepción, Chile*
- 142 <sup>66</sup>*Australian Astronomical Optics, Macquarie University, North Ryde, NSW, Australia*  
 143 <sup>67</sup>*AURA, 950 N. Cherry Ave., Tucson, AZ 85719, USA*
- 144 <sup>68</sup>*Université Claude Bernard Lyon 1, CNRS/IN2P3, IP2I, 4 Rue Enrico Fermi, F-69622 Villeurbanne, France*  
 145 <sup>69</sup>*INAF Osservatorio di Astrofisica e Scienza dello Spazio Bologna, Via P. Gobetti 93/3, 40129, Bologna, Italy*  
 146 <sup>70</sup>*Department of Physics and Astronomy (DIFA), University of Bologna, Via P. Gobetti 93/2, 40129, Bologna, Italy*  
 147 <sup>71</sup>*Centro de Investigaciones Energéticas, Medioambientales y Tecnológicas, Av. Complutense 40, 28040 Madrid, Spain*  
 148 <sup>72</sup>*J.Sick Codes Inc., Penetanguishene, Ontario, Canada*
- 149 <sup>73</sup>*Science and Technology Facilities Council, UK Research and Innovation, Polaris House, North Star Avenue, Swindon, SN2 1SZ, UK*  
 150 <sup>74</sup>*ASTRON, Oude Hoogeveensedijk 4, 7991 PD, Dwingeloo, The Netherlands*  
 151 <sup>75</sup>*Department of Physics, Harvard University, 17 Oxford St., Cambridge MA 02138, USA*
- 152 <sup>76</sup>*National Astronomical Observatory of Japan, Chile Observatory, Los Abedules 3085, Vitacura, Santiago, Chile*  
 153 <sup>77</sup>*Department of Physics, University of Oxford, Denys Wilkinson Building, Keble Road, Oxford, OX1 3RH, UK*  
 154 <sup>78</sup>*LSST Discovery Alliance, 933 N. Cherry Ave., Tucson, AZ 85719, USA*  
 155 <sup>79</sup>*Department of Physics and Astronomy, University of Pittsburgh, 3941 O'Hara Street, Pittsburgh, PA 15260, USA*

156 (Dated: February 19, 2026)

## 157 ABSTRACT

158 We present Rubin Data Preview 1 (DP1), the first data from the NSF-DOE Vera C. Rubin Ob-  
 servatory, comprising raw and calibrated single-epoch images, coadds, difference images, detection

catalogs, and ancillary data products. DP1 is based on 1792 optical/near-infrared exposures acquired over 48 distinct nights by the Rubin Commissioning Camera, LSSTComCam, on the Simonyi Survey Telescope at the Summit Facility on Cerro Pachón, Chile in late 2024. DP1 covers  $\sim 15$  deg<sup>2</sup> distributed across seven roughly equal-sized non-contiguous fields, each independently observed in six broad photometric bands, *ugrizy*. The median FWHM of the point-spread function across all bands is approximately 1''14, with the sharpest images reaching about 0''58. The  $5\sigma$  point source depths for coadded images in the deepest field, the Extended Chandra Deep Field South, are:  $u = 24.55, g = 26.18, r = 25.96, i = 25.71, z = 25.07, y = 23.1$ . Other fields are no more than 2.2 magnitudes shallower in any band, where they have nonzero coverage. DP1 contains approximately 2.3 million distinct astrophysical objects, of which 1.6 million are extended in at least one band in coadds, and 431 solar system objects, of which 93 are new discoveries. DP1 is approximately 3.5 TB in size and is available to Rubin data rights holders via the Rubin Science Platform, a cloud-based environment for the analysis of petascale astronomical data. While small compared to future LSST releases, its high quality and diversity of data support a broad range of early science investigations ahead of full operations in 2026.

*Keywords:* Rubin Observatory – LSST

## 1. INTRODUCTION

The National Science Foundation (NSF)–Department of Energy (DOE) Vera C. Rubin Observatory is a ground-based, wide-field optical/near-infrared facility located on Cerro Pachón in northern Chile. Named in honor of Vera C. Rubin, a pioneering astronomer whose groundbreaking work in the 20th century provided the first convincing evidence for the existence of dark matter (V. C. Rubin & W. K. Ford 1970; V. C. Rubin et al. 1980), the observatory’s prime mission is to carry out the Legacy Survey of Space and Time (LSST) (Ž. Ivezić et al. 2019a). This 10-year survey is designed to obtain rapid-cadence, multi-band imaging of the entire visible southern sky approximately every 3–4 nights. Over its main 18,000 deg<sup>2</sup> footprint, the LSST is expected to reach a depth of  $\sim 27$  magnitude in the r-band, with  $\sim 800$  visits per pointing in all filters (F. B. Bianco et al. 2022).

The Rubin Observatory system consists of four main components: the Simonyi Survey Telescope, featuring an 8.4 m diameter (6.5 m effective aperture) primary mirror that delivers a wide field of view; the 3.2-gigapixel LSST Science Camera (LSSTCam), capable of imaging 9.6 square degrees per exposure<sup>80</sup> with seeing-limited quality in six broadband filters, *ugrizy* (320–1050 nm); an automated Data Management System that processes and archives tens of terabytes of data per night, gen-

erating science-ready data products within minutes for a global community of scientists; and an Education and Public Outreach (EPO) program that provides real-time data access, interactive tools, and educational content to engage the public. The integrated system’s étendue<sup>81</sup> of 319 m<sup>2</sup> deg<sup>2</sup>, is over an order of magnitude larger than that of any previous optical observatory, enabling a fast, large-scale survey with exceptional depth in a fraction of the time compared to other observatories.

The observatory’s design is driven by four key science themes: probing dark energy and dark matter; taking an inventory of the solar system; exploring the transient and variable optical sky; and mapping the Milky Way (Ž. Ivezić et al. 2019a). These themes inform the optimization of a range of system parameters, including image quality; photometric and astrometric accuracy; single-visit depth; coadded survey depth; the filter complement; the total number of visits per pointing and their distribution on the sky; and total sky coverage. Additionally, they inform the design of the data processing and access systems. By optimizing the system parameters to support a wide range of scientific goals, we maximize the observatory’s scientific output across all areas, making Rubin a powerful discovery machine capable of addressing a broad range of astrophysical questions.

Throughout the duration of the LSST, Rubin Observatory will issue a series of Data Releases, each representing a complete reprocessing of all LSST data collected up to that point. Prior to the start of the LSST

\* Author is deceased

<sup>80</sup> We define an “exposure” as the process of exposing all detectors in the focal plane. It is synonymous with the term “visit” in DP1. By contrast, an “image” is the output of a single detector following an exposure.

<sup>81</sup> The product of the primary mirror area and the angular area of its field of view for a given set of observing conditions.

survey, commissioning activities generated a significant volume of science-grade data. To make this early data available to the community, the Rubin Early Science Program (L. P. Guy et al. 2026) was established. One key component of this program is a series of Data Previews; early versions of the LSST Data Releases. These previews include preliminary data products derived from both simulated and commissioning data, which, together with early versions of the data access services, are intended to support high-impact early science, facilitate community readiness, and inform the development of Rubin’s operational capabilities ahead of the start of full survey operations. All data and services provided through the Rubin Early Science Program are offered on a shared-risk basis<sup>82</sup>.

This paper describes Rubin’s second of three planned Data Previews: Data Preview 1 (DP1) (NSF-DOE Vera C. Rubin Observatory 2025a). The first, Data Preview 0 (DP0), contained data products produced from the processing of simulated LSST-like data sets. These were released together with a very early version of the Rubin Science Platform (RSP) (M. Jurić et al. 2019), which provided the data access services. DP0 was released in multiple phases; DP0.1, DP0.2, and DP0.3, each building upon the previous and incorporating new data and functionalities. DP0.1 and DP0.2 uses data from the cosmoDC2 simulations (LSST Dark Energy Science Collaboration (LSST DESC) et al. 2021) prepared by the Dark Energy Science Collaboration (DESC), whereas DP0.3 is based on simulated datasets from the Solar System Science Collaboration (SSSC). Online documentation for DP0 is available at <https://dp0.lsst.io>.

DP1 contains data products derived from the reprocessing of science-grade exposures acquired by the Rubin Commissioning Camera (LSSTComCam) in late 2024. The third and final Data Preview, Data Preview 2 (DP2), is planned to be based on a reprocessing of all science-grade data taken with Rubin’s LSSTCam during commissioning.

All Rubin Data Releases and Previews are subject to a two-year proprietary period, with immediate access granted exclusively to LSST data rights holders<sup>83</sup>(R. Blum & the Rubin Operations Team 2020). After the two-year proprietary period, DP1 will be made public. However, even once the data become public, access

for individuals without data rights will not be provided through Rubin Data Access Centers in the US and Chile (R. Blum & the Rubin Operations Team 2020). Alternative access mechanisms are still under discussion and have not yet been finalized.

In this paper, we describe the contents and validation of Rubin DP1, the first Data Preview to deliver data derived from observations conducted by the Vera C. Rubin Observatory, as well as the data-access mechanisms and community-support services that accompany it. DP1 is based on the reprocessing of 1792 science-grade exposures acquired during the first on-sky commissioning campaign, conducted over 48 nights between 2024-10-24 and 2024-12-11. It covers a total area of approximately  $\sim 15$  deg<sup>2</sup> distributed across seven distinct non-contiguous fields. The data products include raw and calibrated single-epoch images, coadded images, difference images, detection catalogs, and other derived data products. DP1 is about 3.5 TB in size and contains around 2.3 million distinct astronomical objects, detected in 2644 coadded images. Full DP1 release documentation is available at <https://dp1.lsst.io>. Despite Rubin Observatory still being in commissioning and not yet complete at the time the observations were acquired, Rubin DP1 provides an important first look at the data, showcasing its characteristics and capabilities.

The structure of this paper is as follows. In section 2 we describe the observatory system and overall construction and commissioning status at the time of data acquisition, the seven fields included in DP1, and the observing strategy used. Section 3 summarizes the contents of DP1 and the data products contained in the release. The data processing pipelines are described in section 4, followed by a description of the data validation and performance assessment in section 5. Section 6 describes the RSP, a cloud-based data science infrastructure that provides tools and services to Rubin data rights holders to access, visualize and analyze peta-scale data generated by the LSST. Section 7 presents Rubin Observatory’s model for community support, which emphasizes self-help via documentation and tutorials, and employs an open platform for issue reporting that enables crowd-sourced solutions. Finally, a summary of the DP1 release and information on expected future releases of data is given in section 8. The appendix contains a useful glossary of terms used throughout this paper.

All magnitudes quoted are in the AB system (J. B. Oke & J. E. Gunn 1983), unless otherwise specified.

<sup>82</sup> Shared risk means early access with caveats: the community benefits from getting a head start on science, preparing analyses, and providing feedback, while also accepting that the system may not work as well as it will during full operations.

<sup>83</sup> Individuals or institutions with formal authorization to access proprietary data collected by the Vera C. Rubin Observatory. See <https://www.lsst.org/scientists/international-drh-list>

## 2. ON-SKY COMMISSIONING CAMPAIGN

The primary objective of the first Rubin on-sky commissioning campaign was to optically align the Simonyi Survey Telescope and verify its ability to deliver acceptable image quality using the Commissioning Camera, *LSSTComCam*. Additionally, the campaign provided valuable operational experience to support commissioning the LSST Science Camera, *LSSTCam* (T. Lange et al. 2024; A. Roodman et al. 2024). We note that commissioning *LSSTComCam* was not an objective of the campaign; rather *LSSTComCam* was used as a tool to support broader observatory commissioning, including early testing of the *Active Optics System* (AOS) (§2.1) and the LSST Science Pipelines (§2.4). As a result, many artifacts present in the data are specific to *LSSTComCam* and will be addressed only if they persist with *LSSTCam*. Accordingly, the image quality achieved during this campaign, and in the *DP1* data, may not reflect the performance ultimately expected from *LSSTCam*.

Approximately 16,000 exposures<sup>84</sup> were collected during this campaign, the majority in support of AOS commissioning, system-level verification, and end-to-end testing of the telescope’s hardware and software. This included over 10000 exposures for AOS commissioning, more than 2000 bias and dark calibration frames, and over 2000 exposures dedicated to commissioning the LSST Science Pipelines. For *DP1*, we have selected a subset of 1792 science-grade exposures from this campaign that are most useful for the community to begin preparing for early science.

At the time of the campaign, the observatory was still under construction, with several key components, such as dome thermal control, full mirror control, and the final AOS configuration either incomplete or still undergoing commissioning. As a result, image quality varied widely throughout the campaign and exhibited a broader distribution than is expected with *LSSTCam*. Despite these limitations, the campaign successfully demonstrated system integration and established a functional observatory.

### 2.1. *Simonyi Survey Telescope*

The Simonyi Survey Telescope (B. Stalder et al. 2024) features a unique three-mirror design, including an 8.4-meter *Primary Mirror Tertiary Mirror* (M1M3) fabricated from a single substrate and a 3.5-meter *Secondary*

*Mirror* (M2). This compact configuration supports a wide 3.5-degree field of view while enabling exceptional stability, allowing the telescope to slew and settle in under five seconds. To achieve the scientific goals of the 10-year LSST, the Observatory must maintain high image quality across its wide field of view (Ž. Ivezić et al. 2019b). This is accomplished through the AOS (B. Xin et al. 2015; G. Megias Homar et al. 2024), which corrects, between successive exposures, wavefront distortions caused by optical misalignments and mirror surface deformations, primarily due to the effect of gravitational and thermal loads.

The AOS, which comprises an open-loop component and a closed-loop component, optimizes image quality by aligning the camera and M2 relative to M1M3, as well as adjusting the shapes of all three mirrors to nanometer precision. The AOS open-loop component corrects for predictable distortions and misalignments, while the closed-loop component addresses unpredictable or slowly varying aberrations using feedback from the corner wavefront sensors. The closed-loop wavefront sensing technique is curvature wavefront sensing, which infers wavefront errors in the optical system by analyzing extra- and intra-focal star images (S. Thomas et al. 2023). Since *LSSTComCam* lacks dedicated wavefront sensors, wavefront errors were instead estimated by defocusing the telescope  $\pm 1.5$  mm on either side of focus and applying the curvature wavefront sensing pipeline to the resulting images. Each night began with an initial alignment correction using a laser tracker to position the system within the capture range of the closed-loop algorithm (G. Megias Homar et al. 2024). Once this coarse alignment was complete, the AOS refined the optical alignment and applied mirror surfaces corrections to optimize the image quality across the *LSSTComCam* field of view.

During LSST Science Pipelines commissioning (§2.4), observations were conducted using the AOS in open-loop mode only, without closed-loop corrections between exposures. Closed-loop operation, which requires additional intra- and extra-focal images with *LSSTComCam*, was not compatible with the continuous data acquisition needed by the pipelines. The image quality for these data was monitored by measuring the *Point Spread Function* (PSF) at *Full Width at Half-Maximum* (FWHM), and closed-loop sequences were periodically run when image quality degradation was observed.

### 2.2. *The LSST Commissioning Camera*

*LSSTComCam* (B. Stalder et al. 2022, 2020; J. Howard et al. 2018; SLAC National Accelerator Laboratory & NSF-DOE Vera C. Rubin Observatory 2024) is

<sup>84</sup> We define an exposure as the process of exposing all *LSSTComCam* detectors. It is synonymous with visit in *DP1*. By contrast, an image is the output of a single *LSSTComCam* detector following an exposure.

423 a 144-megapixel version of the 3.2-gigapixel **LSSTCam**.  
 424 It covers approximately 5% of the **LSSTCam** focal plane  
 425 area, with a field of view of  $\sim 0.5 \text{ deg}^2$  ( $40' \times 40'$ ), com-  
 426 pared to **LSSTCam**'s  $9.6 \text{ deg}^2$ . It was developed to val-  
 427 idate camera interfaces with other observatory compo-  
 428 nents and evaluate overall system performance prior to  
 429 the start of **LSSTCam** commissioning. Although **LSST-**  
 430 **ComCam** has a smaller imaging area, it shares the same  
 431 plate scale of  $0''.2$  per pixel and is housed in a support  
 432 structure that replicates the mass, center of gravity, and  
 433 physical dimensions of **LSSTCam**. All mechanical and  
 434 utility interfaces to the telescope are implemented iden-  
 435 tically, enabling full end-to-end testing of observatory  
 436 systems, including readout electronics, image acquisi-  
 437 tion, and data pipelines. Although the **LSSTComCam**  
 438 cryostat employs a different cooling system (Cryotels) to  
 439 that of **LSSTCam**, it included a refrigeration pathfinder  
 440 to validate the cryogenic system intended for **LSSTCam**.

441 The **LSSTCam** focal plane comprises 25 modular rafts  
 442 arranged in a  $5 \times 5$  grid, of which 21 are science rafts ded-  
 443 icated to imaging and 4 are corner rafts used for guid-  
 444 ing and wavefront sensing. **LSSTCam** employs CCD  
 445 sensors from two vendors: **Imaging Technology Labora-**  
 446 **tory, University of Arizona (UA)** (ITL) and **Teledyne**  
 447 **(E2V)**. In contrast, **LSSTComCam** contains only a single  
 448 science raft equipped exclusively with ITL sensors.  
 449 **Figure 1** presents a schematic of the **LSSTCam** focal  
 450 plane, with the **LSSTComCam** raft positioned at the  
 451 center, corresponding to the **LSSTCam** central science  
 452 raft location. The perspective is from above, looking  
 453 down through the **LSSTComCam** lenses onto the focal  
 454 plane.

455 Each science raft is a self-contained unit compris-  
 456 ing nine  $4\text{K} \times 4\text{K}$  **Charge-Coupled Device (CCD)** (G. E.  
 457 **Smith 2010**) sensors arranged in a  $3 \times 3$  mosaic, complete  
 458 with integrated readout electronics and cooling systems.  
 459 Each sensor is subdivided into 16 segments arranged in  
 460 a  $2 \times 8$  layout, with each segment consisting of  $512 \times 2048$   
 461 pixels and read out in parallel using individual ampli-  
 462 fiers. This design is identical across all science rafts.  
 463 To maintain uniform performance and **calibration**, each  
 464 raft is populated exclusively with sensors from a single  
 465 vendor.

466 **LSSTComCam** consists of a single science raft, desig-  
 467 nated Raft 22 (R22), equipped solely with ITL sensors.  
 468 These sensors were selected from the best-performing re-  
 469 maining ITL devices after the **LSSTCam** rafts were fully  
 470 populated. Some exhibit known issues such as high read-  
 471 out noise (e.g., Detector 8) and elevated **Charge Transfer**  
 472 **Inefficiency (CTI)** (e.g., Detector 5). Consequently, cer-  
 473 tain image artifacts present in the **DP1** dataset may be  
 474 specific to **LSSTComCam**. **Figure 2** shows the **LSST-**  
 475

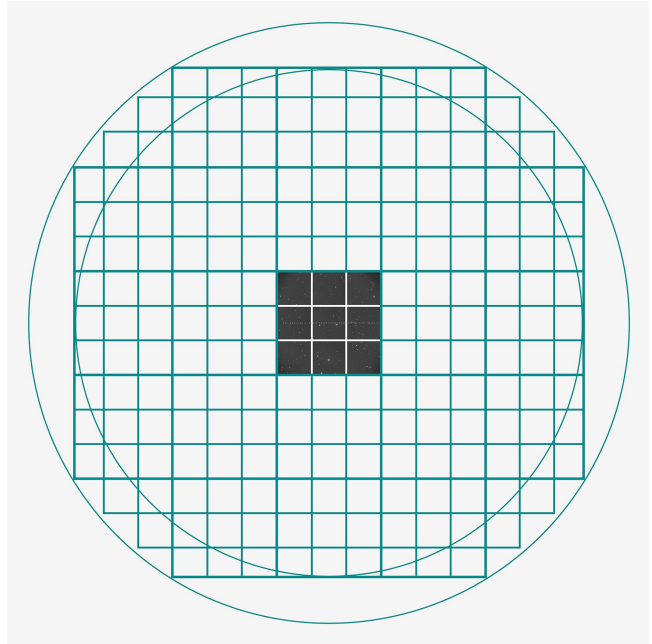


**Figure 1.** **LSSTComCam** focal plane layout illustrating the  
 placement of its nine sensors, shown in gray, which form a  
 raft. The view is looking down from above the focal plane  
 through the **LSSTComCam** lenses. **LSSTComCam** is Raft  
 22 (R22). We also indicate the location of the **LSSTCam**  
 sensors (open squares) to highlight the field-of-view of **LSST-**  
**ComCam** in relation to that of **LSSTCam**.

476 **ComCam** R22 focal plane layout and the placement and  
 477 numbering scheme of sensors (S) and amplifiers (C).  
 478 This configuration is identical across all science rafts  
 479 in **LSSTCam**. The **LSSTCam** and **LSSTComCam** focal  
 480 planes are described in detail in A. A. Plazas Malagón  
 481 et al. (2025).

### 2.2.1. Filter Complement

482 **LSSTComCam** supports imaging with six broadband  
 483 filters *ugrizy* spanning 320–1050 nm, identical in de-  
 484 sign to **LSSTCam**. However, its filter exchanger can  
 485 hold only three filters at a time, compared to five with  
 486 **LSSTCam**. The full-system throughput of the six **LSST-**  
 487 **ComCam** filters, which encompasses contributions from  
 488 a standard atmosphere at airmass 1.2, telescope op-  
 489 tics, camera surfaces, and the mean ITL detector quan-  
 490 tum efficiency is shown in **Figure 3**. The corresponding  
 491 transmission curves are provided as a **DP1** data product  
 492 (§3.6.1).

### 2.2.2. Timing Calibration

493 The absolute time accuracy of data taken with **LSST-**  
 494 **ComCam** relies on the **Network Time Protocol (NTP)**  
 495 for clock synchronization, which should be accurate  
 496 to approximately 1 millisecond. In order to evaluate  
 497 the absolute timing accuracy of the entire system we  
 498  
 499  
 500  
 501

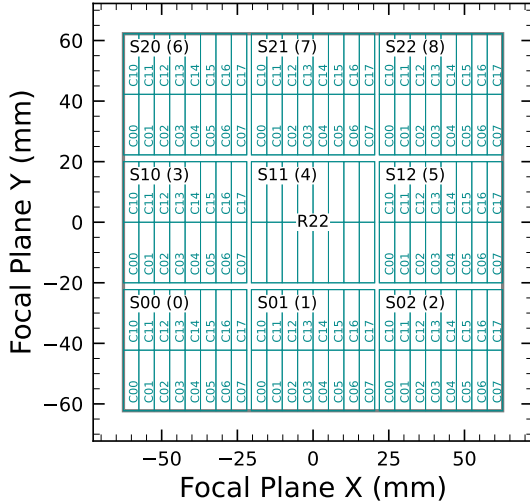


**Figure 2.** LSSTComCam focal plane layout, showing Raft 22 (R22) and the placement and numbering scheme of sensors (S) and amplifiers (C). The view is from above, looking through the LSSTComCam lenses onto the focal plane. Each sensor contains 16 amplifiers, and the raft is composed of a  $3 \times 3$  array of sensors. The detector number for each sensor is indicated in parentheses.

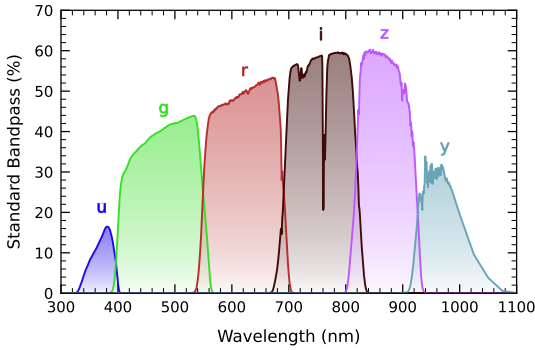


**Figure 3.** LSSTComCam standard bandpasses, illustrating full system throughput. The bandpasses include a standard atmosphere at airmass 1.2, telescope optics, camera surfaces, and mean ITL detector quantum efficiency. The corresponding transmission curves are provided as a DP1 data product.

502 observed the geosynchronous satellite EUTELSAT 117  
 503 West B with a set of 10 usable 10-second exposures over  
 504 two nights. EUTELSAT 117 West B is part the **Global**  
 505 **Positioning System (GPS)** system and serves as one of  
 506 the **Wide Area Augmentation System (WAAS)** satellites  
 507 operated for the **U.S. Federal Aviation Administration**  
 508 **(FAA)** and used to broadcast **GPS** corrections to air  
 509 traffic.

510 As these satellites are part of the **GPS** system, their  
 511 positions are tracked very precisely and the record of  
 512 their locations is published after the fact and can be  
 513 downloaded. Following the technique previously em-

514 ployed by other surveys, (J. L. Tonry et al. 2018), we  
 515 observed the satellite while tracking the sky and then  
 516 downloaded the data-files with its precise locations from  
 517 the National Satellite Test Bed web site<sup>85</sup>. By compar-  
 518 ing the measured and predicted locations of the start  
 519 of the satellite track on the sky, we determined that  
 520 (relative to the start of integration-time recorded in the  
 521 **Flexible Image Transport System (FITS)** headers) our  
 522 time was accurate to  $53.6 \pm 11.0$  milliseconds.

523 This work continues to be an area of ongoing study,  
 524 with the exact timing of when the shutter open com-  
 525 mand is issued, and the complete profile of the shutter  
 526 movement not yet determined. However the open com-  
 527 mand is on average near 29 milliseconds later. Incorpor-  
 528 ating the delays into the fit reduces the offset to  $24.8$   
 529  $\pm 11.0$  milliseconds.

530 The full shutter takes approximately 396 milliseconds  
 531 to completely open. As the LSSTComCam sensors are  
 532 centered in the aperture, the center of the focal plane  
 533 should be exposed about half-way through the shutter  
 534 open procedure, 198 milliseconds after the open com-  
 535 mand. There are uncertainties on the full motion pro-  
 536 file, and the blade direction motions are currently not  
 537 known, but the fraction of the shutter aperture sub-  
 538 tended by the focal plane is 52%. This implies that that  
 539 the shutter will pass any pixel between  $198 \pm 103$  mil-  
 540 liseconds. Subtracting this from the fitted delay of 24.8  
 541 milliseconds and adding the fitted error of 11.0 mil-  
 542 liseconds in quadrature, results in a current conservative es-  
 543 timate of the delay of  $-173.2 \pm 104.1$  milliseconds, con-  
 544 sistent with and smaller than the constraints on the tim-  
 545 ing offset determined using astrometric residuals from  
 546 known asteroid associations presented in §5.9.2.

### 2.3. Flat Field System

547  
 548 During the on-sky campaign, key components of the  
 549 Rubin calibration system (P. Ingraham et al. 2022),  
 550 including the flat field screen, had not yet been in-  
 551 stalled. As a result, flat fielding for DP1 relied en-  
 552 tirely on twilight flats. While twilight flats pose chal-  
 553 lenges such as non-uniform illumination and star print-  
 554 through, they were the only available option during  
 555 LSSTComCam commissioning and for DP1 processing.  
 556 To mitigate these limitations, dithered, tracked expo-  
 557 sures were taken over a broad range of azimuth and rota-  
 558 tor angles to construct combined flat calibration frames.  
 559 Exposure times were dynamically adjusted to reach tar-  
 560 get signal levels of between 10,000 and 20,000 electrons.  
 561 Future campaigns with LSSTCam will benefit from more

<sup>85</sup> <https://www.nstb.tc.faa.gov/nstbarchive.html>

562 stable and uniform flat fielding using the Rubin flat field  
563 system, described in P. Fagrelus & E. S. Rykoff (2025).

#### 564 2.4. LSST Science Pipelines Commissioning

565 Commissioning of the LSST Science Pipelines, (Rubin  
566 Observatory Science Pipelines Developers 2025), began  
567 once the telescope was able to routinely deliver sub-  
568 arcsecond image quality. The goals included testing the  
569 internal astrometric and photometric calibration across  
570 a range of observing conditions, validating the difference  
571 image analysis and prompt processing (K.-T. Lim 2023)  
572 framework, and accumulating over 200 visits per band  
573 to evaluate deep coadded images with integrated expo-  
574 sure times roughly equivalent to those of the planned  
575 LSST Wide-Fast-Deep (WFD) 10-year depth. To sup-  
576 port these goals, seven target fields were selected that  
577 span a range of stellar densities, overlap with external  
578 reference datasets, and collectively span the full breadth  
579 of the four primary LSST science themes. These seven  
580 fields form the basis of the DP1 dataset. Figure 4 shows  
581 the locations of these seven fields on the sky, overlaid on  
582 the LSST baseline survey footprint (R. L. Jones et al.  
583 2021; P. Yoachim 2022; Rubin’s Survey Cadence Opti-  
584 mization Committee et al. 2022, 2023, 2025), along with  
585 the sky coverage of both the LSSTCam and LSSTCom-  
586 Cam focal planes. Each of the seven target fields was  
588 observed repeatedly in multiple bands over many nights.  
589 A typical observing epoch on a given target field con-  
590 sisted of 5-20 visits in each of the three loaded filters.  
591 Only images taken as 1x30 second exposures have been  
592 included in DP1. All images were acquired using the  
593 Rubin Feature-Based Scheduler (FBS), version 3.0 (E.  
594 Naghib et al. 2019; P. Yoachim et al. 2024). Table 1 lists  
595 the seven DP1 fields and their pointing centers, and pro-  
596 vides a summary of the band coverage in each.

597 Figure 5 shows the temporal sampling of observations  
598 by filter and by night. The figure indicates the dates  
599 on which each field was observed in a given band but  
600 does not convey the total number of observations ob-  
601 tained per filter on any individual night. Gaps in cov-  
602 erage across some bands arise from the fact that LSST-  
603 ComCam can only accommodate three filters at a time  
604 (see §2.2). As the campaign progressed, the temporal  
605 sampling became denser across all fields, reflecting im-  
606 proved efficiency and increased time allocated for sci-  
607 ence observations. The Extended Chandra Deep Field-  
608 South Survey (ECDFS) field received the most consis-  
609 tent and densest temporal sampling. It is important to  
610 note that the time sampling in the DP1 dataset differs  
611 significantly from what will be seen in the final LSST  
612 data. All fields except for the low ecliptic latitude field,  
613 Rubin\_SV\_38\_7, used a small random dithering pat-

615 tern. The random translational dithers of the telescope  
616 boresight were applied for each visit, with offsets of up to  
617 0.2 degrees around the pointing center. The rotational  
618 dithers of the camera rotator were typically approxi-  
619 mately 1 degree per visit, with larger random offsets  
620 at each filter change, which worked to keep operational  
621 efficiency high. The Rubin\_SV\_38\_7 field used a dif-  
622 ferent dither pattern to optimize coverage of Solar Sys-  
623 tem Objects and test Solar System Object linking across  
624 multiple nights. These observations used a 2x2 grid of  
625 LSSTComCam pointings to cover an area of about 1.3  
626 degreex1.3 degrees. The visits cycled between the grid’s  
627 four pointing centers, each separated by 0.65 degrees,  
628 and used small random translational dithers to fill chip  
629 gaps with the goal of acquiring 3-4 visits per pointing  
630 center per band in each observing epoch. The RA and  
631 Dec values provided in Table 1 for this field represent  
632 approximately the center of the four fields.

633 Figure 6 shows sky coverage maps showing the distri-  
634 bution of visits in each of the seven DP1 fields, color  
635 coded by band. The images clearly show the focal plane  
636 chip gaps and dithering pattern. Only the detectors for  
637 which single frame processing succeeded are included  
638 in the plots, which explains why the central region of  
639 47\_Tuc looks thinner than the other fields (see §5.10).  
640 Table 2 reports the 5 $\sigma$  point source depths for coad-  
641 ded images per field and per band, where coverage in  
642 a band is non-zero, together with the expected 10-year  
643 LSST depths derived from the baseline simulated survey  
644 (F. B. Bianco et al. 2022).

#### 645 2.5. Delivered Image Quality

646 The delivered image quality is influenced by contribu-  
647 tions from both the observing system (i.e., dome, tele-  
648 scope and camera) and the atmosphere. During the  
649 campaign, the Rubin Differential Image Motion Monitor  
650 (DIMM) was not operational, so atmospheric seeing was  
651 estimated using live data from the Southern Astrophys-  
652 ical Research Telescope (SOAR) Ring-Image Next Gen-  
653 eration Scintillation Sensor (RINGSS) seeing monitor,  
654 also located on Cerro Pachón. Although accelerometers  
655 mounted on the mirror cell and top-end assembly were  
656 available to track dynamic optics effects, such as mir-  
657 ror oscillations that can degrade optical alignment, this  
658 data was not used during the campaign. Mount encoder  
659 data were used to measure the mount jitter in every im-  
660 age, with a measured median contribution of 0.004 arc-  
661 seconds to image degradation. As the pointing model  
662 was not fine tuned, tracking errors could range from 0.2  
663 to 0.4 arcseconds per image, depending on RA and Dec.  
664 Dome and mirror-induced seeing were not measured dur-  
665 ing the campaign.

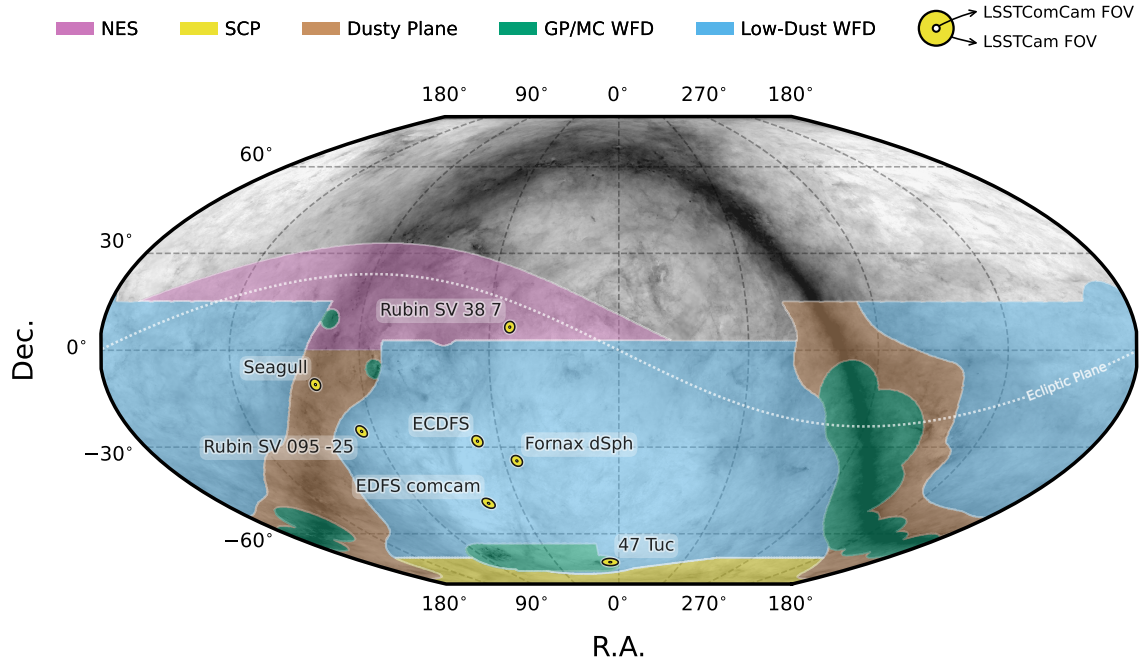


**Figure 4.** Locations of the seven DP1 fields overlaid on the LSST baseline survey footprint. NES: North Ecliptic Spur, SCP: South Celestial Pole, Low-Dust WFD: regions away from the Galactic Plane (GP) observed with a WFD cadence, GP/MC WFD: Galactic Plane and Magellanic Clouds regions observed with a WFD cadence. The field of view covered by the LSSTCam and LSSTComCam focal planes is shown as concentric yellow circles about the pointing center of each field.

**Table 1.** DP1 fields and pointing centers with the number of exposures in each band per field. ICRS coordinates are in units of decimal degrees, and are specified as J2000.

Field Code	Field Name	RA	Dec	Band						Total
				deg	deg	<i>u</i>	<i>g</i>	<i>r</i>	<i>i</i>	
47_Tuc	47 Tucanae Globular Cluster	6.128	-72.090	6	10	32	19	0	5	72
ECDFS	Extended Chandra Deep Field South	53.160	-28.100	43	230	237	162	153	30	855
EDFS_comcam	Rubin SV Euclid Deep Field South	59.150	-48.730	20	61	87	42	42	20	272
Fornax_dSph	Fornax Dwarf Spheroidal Galaxy	40.080	-34.450	0	5	25	12	0	0	42
Rubin_SV_095_-25	Rubin SV Low Galactic Latitude Field	95.040	-25.000	33	82	84	23	60	10	292
Rubin_SV_38_7	Rubin SV Low Ecliptic Latitude Field	37.980	7.015	0	44	40	55	20	0	159
Seagull	Seagull Nebula	106.300	-10.510	10	37	43	0	10	0	100
Total				112	469	548	313	285	65	1792

667 The DP1 median delivered image quality, quantified  
 668 as the PSF at FWHM across all filters and target fields,  
 669 is  $1''.14$ . The best images achieve a PSF FWHM of ap-  
 670 proximately  $0''.58$ . Both the per-sensor PSF FWHM and  
 671 the overall median vary depending on the filter and the  
 672 specific target field. The median delivered image quality  
 673 per band and target field is provided in Table 3. Fig-  
 674 ure 7 shows the distribution of PSF FWHM (in arcsec)  
 675 over all 16071 individual sensors images. Ongoing efforts  
 676 aim to quantify all sources of image degradation, includ-

678 ing contributions from the camera system; static and  
 679 dynamic optical components; telescope mount motion;  
 680 observatory-induced seeing from the dome and primary  
 681 mirror; and atmospheric conditions. For the LSST, the  
 682 design specification for the median delivered image qual-  
 683 ity, referenced to the zenith and 550 nm, is  $0''.7$ . This  
 684 value corresponds to the measured median atmospheric  
 685 seeing at the Cerro Pachón site and a system contribu-  
 686 tion to delivered image quality of  $0''.35$  added in quadra-  
 687 ture.

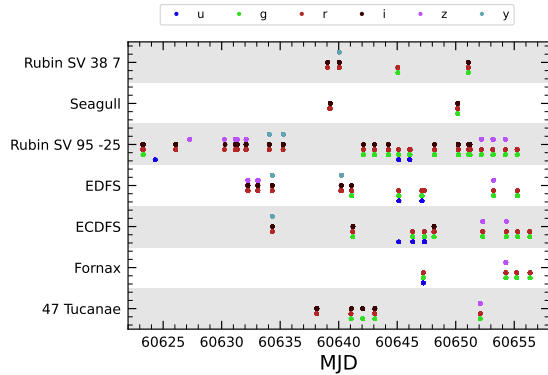


**Figure 5.** Temporal distribution of DP1 observations, grouped by field as a function of Modified Julian Date (MJD) and color-coded by filter. Each point indicates that a given field was observed at least once in the corresponding filter on that date.

**Table 2.** DP1 median  $5\sigma$  coadded point-source detection limits per field and band, expressed in magnitudes, compared with the expected 10-year LSST values derived from the baseline simulated survey (F. B. Bianco et al. 2022).

Field Code	Band					
	<i>u</i>	<i>g</i>	<i>r</i>	<i>i</i>	<i>z</i>	<i>y</i>
47_Tuc	-	24.03	24.24	23.90	-	21.79
ECDFS	24.55	26.18	25.96	25.71	25.07	23.10
EDFS_comcam	23.42	25.77	25.72	25.17	24.47	23.14
Fornax_dSph	-	24.53	25.07	24.64	-	-
Rubin_SV_095_-25	24.29	25.46	24.95	24.86	24.32	22.68
Rubin_SV_38_7	-	25.46	25.15	24.86	23.52	-
Seagull	23.51	24.72	24.19	-	23.30	-
LSST 10-year	25.73	26.86	26.88	26.34	25.63	24.87

### 3. OVERVIEW OF THE CONTENTS OF RUBIN DP1

In this section we describe the Rubin DP1 data products and provide summary statistics for each. For more detailed information, we refer the reader to the DOI-registered DP1 release documentation available at <https://dp1.lsst.io> and the catalog schemas available at <https://sdm-schemas.lsst.io>.<sup>86</sup>

The DP1 science data products are derived from the 15972 individual CCD images taken across 1792 exposures in the seven LSSTComCam commissioning fields

**Table 3.** DP1 Median image quality per field and per band quantified as the PSF at FWHM in arcseconds.

Field Code	Band						All
	<i>u</i>	<i>g</i>	<i>r</i>	<i>i</i>	<i>z</i>	<i>y</i>	
47_Tuc	-	1.27	1.25	1.11	-	1.33	1.22
ECDFS	1.40	1.14	1.08	1.00	1.00	1.07	1.08
EDFS_comcam	1.88	1.25	1.20	1.10	1.18	0.99	1.19
Fornax_dSph	-	1.16	0.82	0.93	-	-	0.85
Rubin_SV_095_-25	1.40	1.25	1.14	0.97	1.17	0.82	1.19
Rubin_SV_38_7	-	1.13	1.13	1.10	1.22	-	1.13
Seagull	1.50	1.34	1.19	-	1.19	-	1.25
All	1.48	1.17	1.12	1.03	1.11	1.01	1.13

(§2.4). To aid legibility, we have separated the descriptions of the data products from the description of the data release processing pipeline (§4). Similarly, as the DP1 data products can be accessed via one or both of International Virtual Observatory Alliance (IVOA) Services (§6.2.1) or the Data Butler (§6.2.2), we describe them here in a manner that is agnostic to the means of access.

The data products that comprise DP1 provide an early preview of future LSST data releases and are strongly dependent on the type and quality of the data that was collected during the LSSTComCam on-sky campaign (§2.4). Consequently not all anticipated LSST data products, as described in the Data Product Definition Document (DPDD) (M. Jurić et al. 2023), were produced for the DP1 dataset.

Rubin Observatory has adopted the convention by which single-epoch detections are referred to as “Sources”, and the astrophysical object associated with a given detection is referred to as an “Object”<sup>87</sup>. As such, a given Object will likely have multiple associated Sources, since it will be observed in multiple epochs.

At the highest level, the DP1 data products fall into one of five types:

- **Science Images**, including single-epoch images, deep and template coadded images, and difference images (§3.1);
- **Catalogs** of astrophysical Sources and Objects detected and measured in the aforementioned images. We also provide the astrometric and photo-

<sup>86</sup> Searchable catalog schemas are also available to Data Rights Holders via the Rubin Science Platform at <https://data.lsst.cloud>.

<sup>87</sup> We caution that this nomenclature is not universal; for example, some surveys use “detections” for what we call “sources”, and “sources” for what we call “objects”.

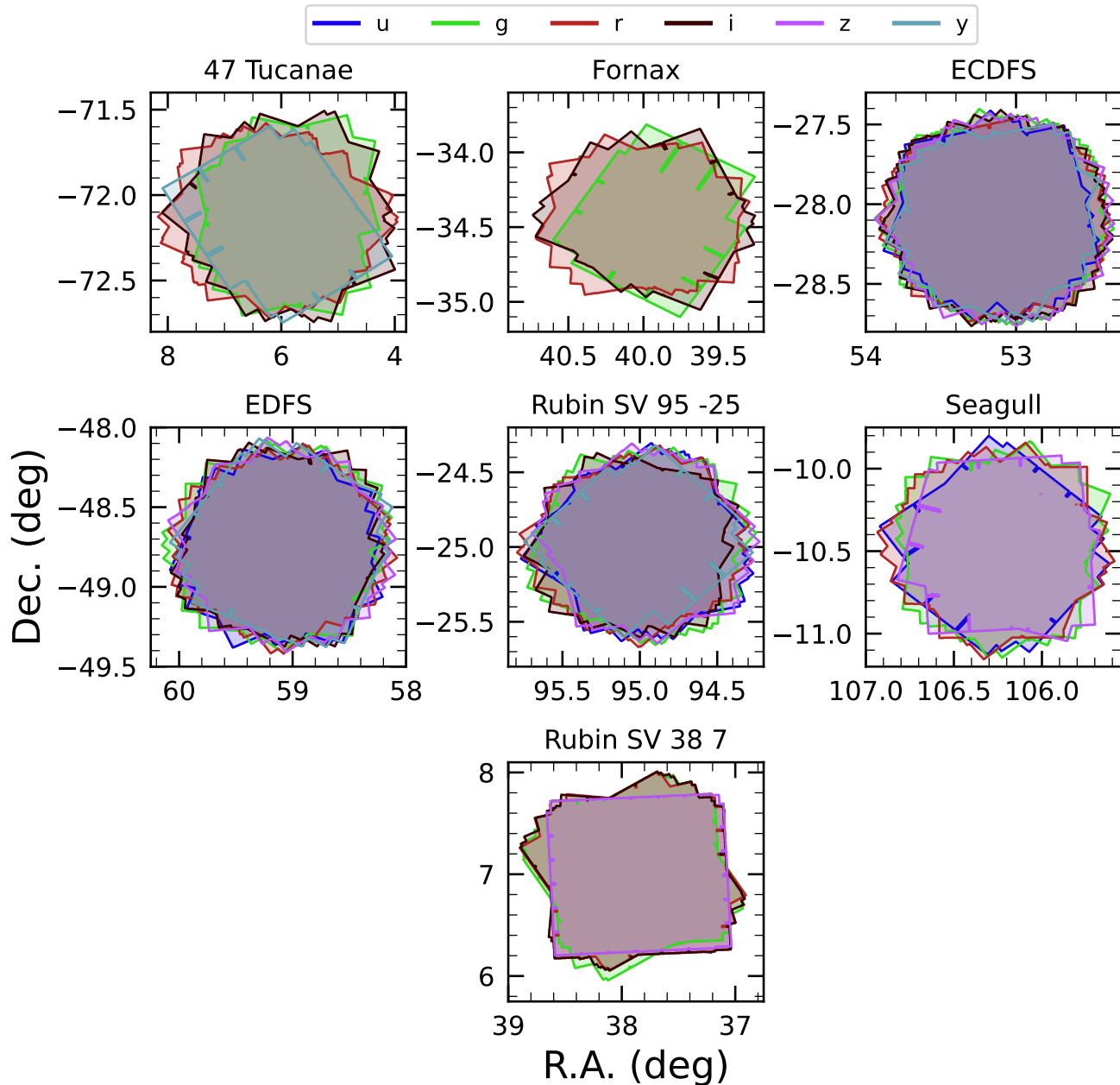


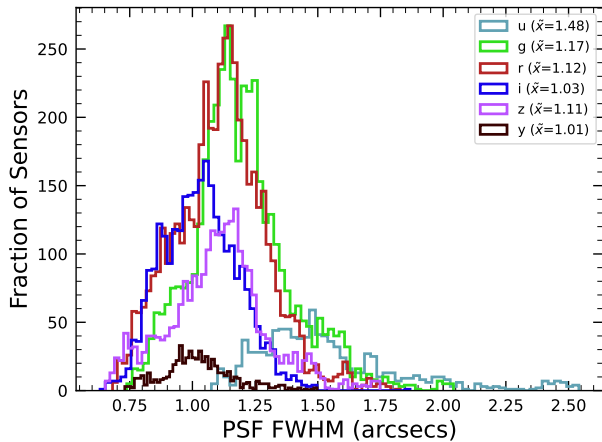
**Figure 6.** Sky coverage maps showing the distribution of visits in each field, color coded by band. The images clearly show the focal plane chip gaps and dithering pattern. Only the detectors for which single frame processing succeeded are included in the plots, which explains why the central region of 47\_Tuc looks thinner than the other fields.

729 metric reference catalog generated from external  
730 sources that was used during processing to gener-  
731 ate the DP1 data products (§3.2);

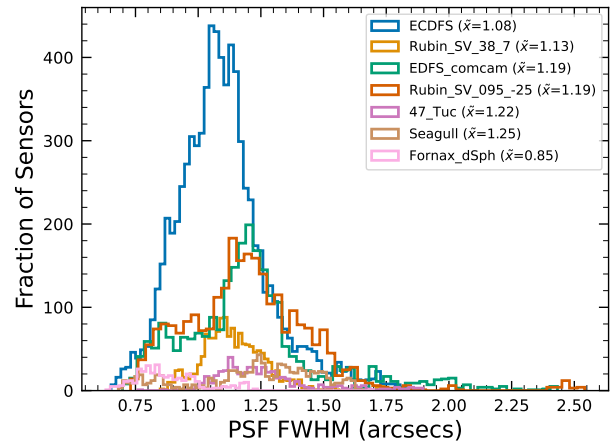
732 • **Maps**, which provide non-science-level visualiza-  
733 tions of the data within the release. They include,  
734 for example, zoomable multi-band images and cover-  
735 age maps (§3.4.1);

736 • **Ancillary data products**, including, for exam-  
737 ple, the parameters used to configure the data pro-  
738 cessing pipelines, log and processing performance  
739 files, and calibration data products (§3.6);

740 • **Metadata** in the form of tables containing infor-  
741 mation about each visit and processed image, such  
742 as pointing, exposure time, and a range of image  
743 quality summary statistics (§3.5).



(a) PSF FWHM (arcsecs) per passband across all DP1 target fields.



(b) PSF FWHM (arcsecs) per DP1 target field across all passbands

**Figure 7.** Histograms showing the distribution of delivered image quality for all 16071 single-epoch individual sensors in the DP1 dataset per passband (a) and per field (b). The median values are given in the legend.

744 While images and catalogs are expected to be the pri-  
 745 mary data products for scientific research, we also rec-  
 746 ognize the value of providing access to other data types  
 747 to support investigations and ensure transparency.

748 To facilitate processing, Rubin DP1 uses a single  
 749 skymap<sup>88</sup> that covers the entire sky area encompass-  
 750 ing the seven DP1 fields. The DP1 skymap divides the  
 751 entire celestial sphere into 18938 *tracts*, each covering  
 752 approximately  $2.8 \text{ deg}^2$ . The *tracts* are arranged in rings  
 753 of declination, ordered from south to north, then with  
 754 increasing right ascension within a ring. Each *tract* is  
 755 further subdivided into  $10 \times 10$  equally-sized patches.  
 756 Both *tracts* and patches overlap with their neighboring  
 757 regions. The amount of overlap between *tracts* changes  
 758 with declination, with *tracts* nearest the poles having  
 759 the greatest degree of overlap; the minimum overlap be-  
 760 tween *tracts* is  $1/0$ . By contrast, the amount of overlap  
 761 between patches is constant, with each *patch* overlap-  
 762 ping each of its neighbouring patches by  $80\%$ . Each  
 763 patch covers  $0.036 \text{ deg}^2$  which, due to the patch overlap,  
 764 is slightly larger than the tract area divided by the  
 765 number of patches in a tract. The aerial coverage of  
 766 a patch is comparable to, but somewhat smaller than,  
 767 the  $0.058 \text{ deg}^2$  field-of-view of a single LSSTComCam or  
 768 LSSTCam detector, meaning each detector image spans  
 769 multiple patches. The size of a tract is larger than the  
 770 LSSTComCam field of view. However, since each ob-

771 served field extends across more than one tract, each  
 772 field covers multiple tracts.

773 The skymap is integral to the production of co-added  
 774 images. To create a coadded image, the processing  
 775 pipeline selects all calibrated science images in a given  
 776 field that meet specific quality thresholds (§3.1 and  
 777 §4.5.1) for a given *patch*, warps them onto a single  
 778 consistent pixel grid for that *patch*, as defined by the  
 779 skymap, then coadds them. Each individual coadd im-  
 780 age therefore covers a single *patch*.

781 Throughout this section, the data product names are  
 782 indicated using `monospace` font. Data products are ac-  
 783 cessed via either the IVOA Services (§6.2.1) or the Data  
 784 Butler (§6.2.2).

### 785 3.1. Science Images

786 Science images are exposures of the night sky, as dis-  
 787 tinct from *calibration* images (§3.6.3). Although the re-  
 788 lease includes *calibration* images, thereby allowing users  
 789 to reprocess the raw images if needed, this is expected  
 790 to be necessary only in rare cases. Users are strongly  
 791 encouraged to start from the `visit_image` provided.  
 792 The data product names shown here are those used by  
 793 the Data Butler, but the names used in the IVOA Ser-  
 794 vices differ only slightly in that they are prepended by  
 795 “`lsst.`”.

#### 796 3.1.1. Raw Image

797 *raw* images (NSF-DOE Vera C. Rubin Observatory  
 798 2025b) are unprocessed data received directly from the  
 799 camera. Each *raw* corresponds to a single CCD from a  
 800 single LSSTComCam exposure of 30 s duration. Each  
 801 LSSTComCam exposure typically produces up to nine  
 802 *raws*, one per sensor in the focal plane. However, a

<sup>88</sup> A skymap is a tiling of the celestial sphere, organizing large-scale sky coverage into manageable sections for processing and analysis. While the skymap described here is specific to DP1, we do not anticipate major changes to the skymap in future data releases.

**Table 4.** Number of raw images per field and band. Each raw image corresponds to a single 30-second LSSTComCam exposure on one CCD. Most exposures produce nine raw images, one per sensor in the focal plane, however some yield fewer due to occasional hardware or readout issues.

Field Code	Band						Total
	<i>u</i>	<i>g</i>	<i>r</i>	<i>i</i>	<i>z</i>	<i>y</i>	
47_Tuc	54	90	288	171	0	45	648
ECDFS	387	2070	2133	1455	1377	270	7692
EDFS_comcam	180	549	783	378	378	180	2448
Fornax_dSph	0	45	225	108	0	0	378
Rubin_SV_095_-25	297	738	756	207	540	90	2628
Rubin_SV_38_7	0	396	360	495	180	0	1431
Seagull	90	333	387	0	90	0	900
Total	1008	4221	4932	2814	2565	585	16125

small number of exposures resulted in fewer than nine raw images due to temporary hardware issues or readout faults.

In total, DP1 includes 16125 raw images. Table 4 provides a summary by target and band. A raw contains  $4608 \times 4096$  pixels, including prescan and overscan, and occupies around 18 MB of disk space.<sup>89</sup> The field of view of a single raw, excluding prescan and overscan regions, is roughly  $0^\circ.23 \times 0^\circ.22 \approx 0.051 \text{ deg}^2$ , corresponding to a plate scale of  $0''.2$  per pixel.

### 3.1.2. Visit Image

visit\_images (NSF-DOE Vera C. Rubin Observatory 2025c) are fully-calibrated processed images. They have undergone instrument signature removal (§4.2.1) and all the single frame processing steps described in §4.2 which are, in summary: PSF modeling, background subtraction, and astrometric and photometric calibration. As with raws, a visit\_image contains processed data from a single CCD resulting from a single 30 s LSSTComCam exposure. As a consequence, a single LSSTComCam exposure typically results in nine visit\_images. The handful of exposures with fewer than nine raw images also have fewer than nine visit\_images, but there are an additional 153 raw images that failed processing and for which there is thus no corresponding visit\_image. The majority of failures – 131 in total – were due to challenges with astrometric fits or PSF models

<sup>89</sup> Each amplifier image contains 3 and 64 columns of serial prescan and overscan pixels, respectively, and 48 rows of parallel overscan pixels, meaning a raw contains  $4072 \times 4000$  exposed pixels.

in the 47\_Tuc crowded field. The other failures were in the Rubin\_SV\_095\_-25 (9 failures), ECDFS (8), Fornax\_dSph (3), and EDFs\_comcam (2) fields.

In total, there are 15972 visit\_images in DP1. Each visit\_image comprises three images: a calibrated science image, a variance image, and a pixel-level bit-mask that flags issues such as saturation, cosmic rays, or other artifacts. Each visit\_image also contains a position-dependent PSF model, World Coordinate System (WCS) information, and various metadata providing information about the observation and processing. The science and variance images and the pixel mask each contain  $4072 \times 4000$  pixels. In total, a single visit\_image, including all extensions and metadata, occupies around 110 MB of disk space. A plot showing the normalized cumulative histogram of the  $5\sigma$  depths of all the visit\_images in DP1 is shown in Figure 8.

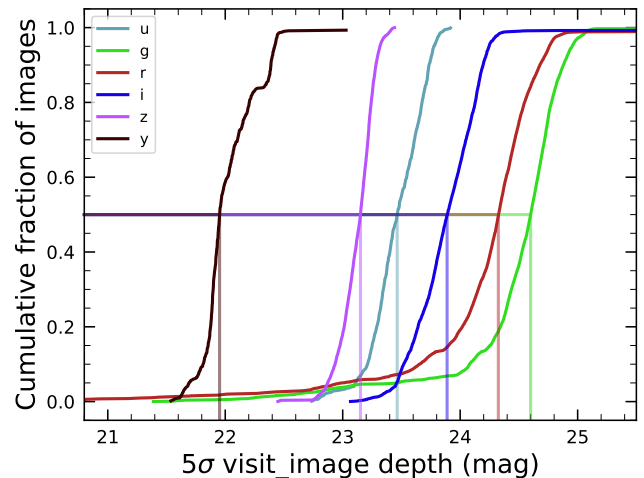


**Figure 8.** Normalized cumulative histograms of the  $5\sigma$  depths of all visit\_images in each band. The vertical lines indicate the 50th percentiles for each band (see legend).

### 3.1.3. Deep Coadd

deep\_coadds are created on a per-band basis, meaning only data from exposures taken with a common filter are coadded. As such, there are up to six deep\_coadds covering each patch – one for each of the six LSSTComCam bands. The process of producing deep\_coadds is described in §4.5 but, to summarize, it involves the selection of suitable visit\_images (both in terms of patch coverage, band, and image quality), the warping of those visit\_images onto a common pixel grid, and the co-adding of the warped visit\_images. To be included in a DP1 deep\_coadd, a visit\_image needed to have a PSF FWHM smaller than  $1''.7$ . Of the 15972 visit\_

861 images, 15375 satisfied this criterion and were therefore  
862 used to create `deep_coadds`.

863 There are a total of 2644 `deep_coadds` in DP1. As  
864 mentioned above, a single `deep_coadd` covers one `patch`,  
865 and includes a small amount of overlap with its neigh-  
866 boring `patch`. The skymap used for DP1 defines a `patch`  
867 as having an on-sky area of  $0.028 \text{ deg}^2$  excluding overlap,  
868 and  $0.036 \text{ deg}^2$  including overlap. A single `deep_coadd`  
869 – including overlap – contains  $3400 \times 3400$  equal-sized  
870 pixels, corresponding to a platescale of  $0''.2$  per pixel.  
871 Each `deep_coadd` contains the science image (i.e., the  
872 coadd), a variance image, and a pixel mask; all three  
873 contain the same number of pixels. Each `deep_coadd`  
874 also contains a position-dependent PSF model (which  
875 is the weighted sum of the PSF models of the input  
876 `visit_images`), WCS information, plus various `meta-`  
877 `data`.

878 The number of `visit_images` that contributed to a  
879 given `deep_coadd` varies across the patch; the Survey  
880 Property Maps can be consulted to gain insights into  
881 the total exposure time at all locations covered by the  
882 survey. Similarly, since coadds always cover an entire  
883 `patch`, it is common for a `deep_coadd` to contain regions  
884 that were not covered by any of the selected `visit_`  
885 `images`, particularly if the `patch` is on the outskirts of  
886 a field and was thus not fully observed. By the nature  
887 of how coadds are produced, such regions may contain  
888 seemingly valid `flux` values (i.e., not necessarily zeros or  
889 NaNs), but will instead be flagged with the `NO_DATA` flag  
890 in the pixel mask. It is therefore crucial that the pixel  
891 mask be referred to when analyzing `deep_coadds`.

### 892 3.1.4. *Template Coadd*

893 `template_coadds` (NSF-DOE Vera C. Rubin Obser-  
894 vatory 2025d) are those created to use as templates for  
895 difference imaging, i.e., the process of subtracting a tem-  
896 plate image from a `visit_image` to identify either vari-  
897 able or `transient` objects. It should be noted, however,  
898 that `template_coadds` are not themselves subtracted  
899 from `visit_images` but are, instead, warped to match  
900 the WCS of a `visit_image`. It is this warped template  
901 that is subtracted from the `visit_image` to create a  
902 difference image.<sup>90</sup> As with `deep_coadds`, `template_`  
903 `coadds` are produced by warping and co-adding multiple  
904 `visit_images` covering a given skymap-defined `patch`.  
905 The process of building `template_coadds` is the same  
906 as that for `deep_coadds`, but the selection criteria differ  
907 between the two types of coadd. In the case of `tem-`

908 `plate_coadds`, one third of `visit_images` covering the  
909 `patch` in question with the narrowest PSF FWHM are  
910 selected. If one third corresponds to fewer than twelve  
911 `visit_images` (i.e., there are fewer than 36 `visit_im-`  
912 `ages` covering the `patch`), then the twelve `visit_images`  
913 with the narrowest PSF FWHM are selected. Finally, if  
914 there are fewer than twelve `visit_images` covering the  
915 `patch`, then all `visit_images` are selected. Of the 15972  
916 `visit_images`, 13113 were used to create `template_`  
917 `coadds`. This selection strategy is designed to opti-  
918 mize for `seeing` when a `patch` is well-covered by `visit_`  
919 `images`, yet still enable the production of `template_`  
920 `coadds` for poorly-covered patches. As with `deep_`  
921 `coadds`, the number of `visit_images` that contributed  
922 to a `template_coadd` varies across the patch.

923 DP1 contains a total of 2730 `template_coadds`.<sup>91</sup> As  
924 with `deep_coadds`, a single `template_coadd` covers a  
925 single `patch`. Since the same skymap is used when cre-  
926 ating both `deep_coadd` and `template_coadds`, the on-  
927 sky area and pixel count of `template_coadds` are the  
928 same as that of a `deep_coadd` (see above). Similarly,  
929 `template_coadds` contain the science image (i.e., the  
930 coadd), a variance image, and a pixel mask; all three  
931 contain the same number of pixels. Also included are  
932 the PSF model, WCS information, and `metadata`. As  
933 is the case for `deep_coadds`, those pixels within `tem-`  
934 `plate_coadds` that are not covered by any of the se-  
935 lected `visit_images` may still have seemingly valid val-  
936 ues, but are indicated with the `NO_DATA` flag within the  
937 pixel mask.

### 938 3.1.5. *Difference Image*

939 `difference_images` (NSF-DOE Vera C. Rubin Ob-  
940 servatory 2025e) are generated by the subtraction of  
941 the warped, scaled, and PSF-matched `template_coadd`  
942 from the `visit_image` (see §4.6.1). In principle, only  
943 those sources whose `flux` has changed relative to the  
944 `template_coadd` should be apparent (at a significant  
945 level) within a `difference_image`. In practice, how-  
946 ever, there are numerous spurious sources present in  
947 `difference_images` due to unavoidably imperfect tem-  
948 plate matching.

949 In total, there are 15972 `difference_images` in DP1,  
950 one for each `visit_image`.

951 Like `visit_images`, `difference_images` contain the  
952 science (i.e., difference) image, a variance image, and a  
953 pixel mask; all three contain the same number of pixels,  
954 which is the same as that of the input `visit_image`.

<sup>90</sup> For storage space reasons, warped templates are not retained for DP1, as they can be readily and reliably recreated from the `template_coadds`.

<sup>91</sup> The difference in the number of `deep_coadds` and `template_coadds` is due to the difference in the `visit_image` selection criteria for each coadd.

Also included is the `PSF` model, `WCS` information, and `metadata`.

### 3.1.6. Background Images

Background images contain the model `background` that has been generated and removed from a science image. `visit_images`, `deep_coadds` and `template_coadds` all have associated `background` images.<sup>92</sup> Background images contain the same number of pixels as their respective science image, and there is one `background` image for each `visit_image`, `deep_coadd`, and `template_coadd`. Difference imaging analysis also measures and subtracts a `background` model, but the `difference_background` data product is not written out by default and is not part of `DP1`.

Background images are not available via the `IVOA` Service; they can only be accessed via the `Butler` Data Service.

## 3.2. Catalogs

In this section we describe science-ready tables produced by the science pipelines. All catalogs contain data for detections in the images described in §3.1, except the `Calibration` catalog, which contains reference data obtained from previous surveys. Observatory-produced `metadata` tables are described in §3.5.

The catalogs contains measurements for either Sources detected in `visit_images` and `difference_images`, or Objects detected in `deep_coadds`. All catalogs store fluxes rather than magnitudes, with fluxes measured in nanojansky ( $1 \text{ nJy} = 10^{-35} \text{ Wm}^{-2}\text{Hz}^{-1}$ ). Fluxes are preferred for multi-epoch observations, as they can be averaged across epochs, unlike magnitudes. Additionally, flux measurements on difference images (§3.1) are computed against a template, representing a flux difference. As a result, flux measurements on difference images can be negative, particularly for faint sources in the presence of noise.

The `Source`, `Object`, `ForcedSource`, `DiaSource`, `DiaObject`, and `ForcedSourceOnDiaObject` catalogs described below each vary in terms of their specific columns but generally contain: one or more unique identification numbers, positional information, multiple types of `flux` measurements (e.g., aperture fluxes, `PSF` fluxes, Gaussian fluxes, etc.), and a series of boolean flags indicating characteristics such as saturation or cosmic ray contamination for each source/object. The Solar System catalogs `SSObject` and `SSSource` deviate from

this general structure in that they instead contain orbital parameters for all known asteroids.

Where applicable, quantities are prefixed with the band in which they were measured, and all measured properties are reported with their associated  $1\sigma$  uncertainties. For example, `g_ra` and `g_raErr` refer to right ascension and its uncertainty, measured in the g-band.

Fluxes for various apertures are provided together with an uncertainty and a flag, and named in the format `[band]_ap[size]Flux`, where `[size]` is the aperture diameter in pixels. For example, `g_ap03Flux`, `g_ap03FluxErr`, `g_ap03Flux_flag` provide the flux, uncertainty and flag measured within a 3.0-pixel aperture in the g-band. Similarly for flux measurements using difference algorithms, e.g. `g_psfFlux` provides the flux derived using the `PSF` model as a weight function, forced on g-band.

A complete list of columns with description and units for all tables in `DP1` is available at <https://sdm-schemas.lsst.io/dp1.html> Since `DP1` is a preview release, it does not include all the catalogs expected in a full `LSST Data Release`. Additionally, some catalogs may be missing columns, as not all quantities have been computed yet. These quantities will be included in future releases, and, where it is known to be the case, missing data are noted in the catalog descriptions that follow.

Catalog data are stored in the `Qserv` database (§6.5.1) and are accessible via `Table Access Protocol (IVOA standard) (IVOA)`, and an online `DP1` catalog schema is available at <https://sdm-schemas.lsst.io/dp1.html>. Catalog data are also accessible via the `Data Butler` (see §6.2.2).

### 3.2.1. Source Catalog

The `Source` catalog (`NSF-DOE Vera C. Rubin Observatory 2025f`) contains data on all sources which are, prior to deblending (§4.5.2), detected with a greater than  $5\sigma$  significance in each individual visit. The detections reported in the `Source` catalog have undergone deblending; in the case of blended detections, only the deblended sources are included in the `Source` catalog. It is important to note that while the criterion for inclusion in a `Source` catalog is a  $> 5\sigma$  detection in a `visit_image` prior to deblending, the positions and fluxes are reported post-deblending. Hence, it is possible for the `Source` catalog to contain sources whose `flux-to-error` ratios – potentially of all types (i.e., aperture `flux`, `PSF flux`, etc.) – are less than 5.

In addition to the general information mentioned above (i.e., IDs, positions, fluxes, flags), the `Source` catalog also includes basic `shape` and extendedness information.

<sup>92</sup> In future data releases, `background` images may be included as part of their respective science image data product.

1052 The `Source` catalog contains data for 46 million  
1053 `sources` in DP1.

1054 A cumulative histogram showing the PSF magnitudes  
1055 of all `sources` contained within the `Source` catalogue is  
1056 presented in the top panel of Figure 9

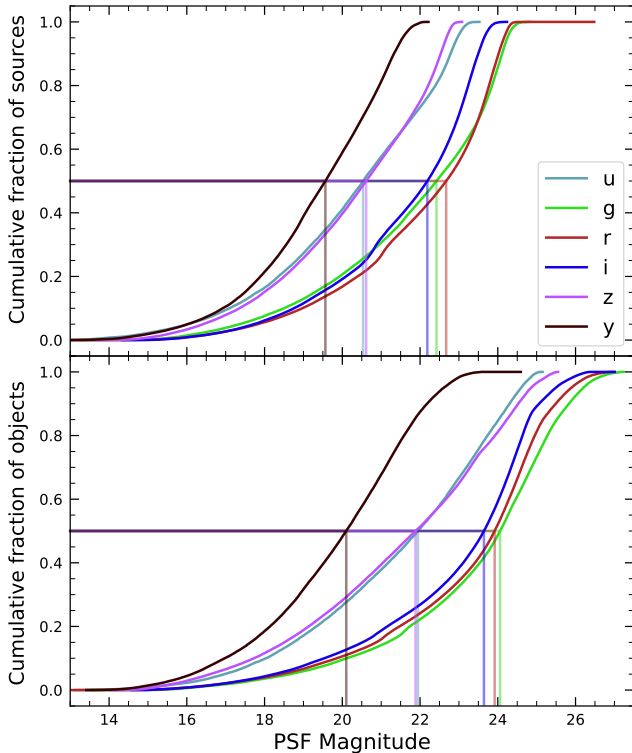


**Figure 9.** Normalized cumulative histograms of the PSF magnitudes of all  $> 5\sigma$ -detected `sources` (top panel) and `objects` (bottom panel) contained in the `Source` and `Object` catalogs, respectively, separated according to band (see legend). The vertical lines indicate the 50th percentile for each band.

### 3.2.2. Object Catalog

1057  
1058 The `Object` catalog (NSF-DOE Vera C. Rubin Ob-  
1059 servatory 2025g) contains data on all objects detected  
1060 with a greater than  $5\sigma$  significance in the `deep_coadds`.  
1061 With coadd images produced on a per-band basis, a  
1062  $> 5\sigma$  detection in one or more of the bands will re-  
1063 sult in an object being included in the `Object` catalog.  
1064 For cases where an object is detected at  $> 5\sigma$  in more  
1065 than one band, a cross-matching has been performed  
1066 between bands to associate an object in one band with  
1067 its counterpart(s) in the other bands. As such, the `Ob-`  
1068 `ject` catalog contains data from multiple bands. The  
1069 objects reported in the `Object` catalog have also under-  
1070 gone deblending; in the case of blended detections, only  
1071 the deblended child objects are included in the catalog.  
1072 As with the `Source` catalog, the criterion for inclusion

1073 in the `Object` catalog is a  $> 5\sigma$  detection in one of the  
1074 `deep_coadds` prior to deblending, yet the positions and  
1075 fluxes of objects are reported post-deblending. Hence, it  
1076 is possible for `Object` catalog to contain `objects` whose  
1077 flux-to-error ratios — potentially of all types and in all  
1078 bands — are less than 5.

1079 In addition to the general information mentioned  
1080 above (i.e., IDs, positions, fluxes, flags), the `Object` cat-  
1081 alog also includes basic `shape` and extendedness informa-  
1082 tion. While they may be included in future data releases,  
1083 no photometric redshifts, Petrosian magnitudes (V. Pet-  
1084 rosian 1976), proper motions or periodicity information  
1085 are included in the DP1 object catalogs.

1086 The `Object` catalog contains data for 2.3 million ob-  
1087 jects in DP1.

### 3.2.3. ForcedSource Catalog

1088  
1089 The `ForcedSource` catalog (NSF-DOE Vera C. Ru-  
1090 bin Observatory 2025h) contains forced PSF photome-  
1091 try measurements performed on both `difference_im-`  
1092 `ages` (i.e., the `psfDiffFlux` column) and `visit_images`  
1093 (i.e., the `psfFlux` column) at the positions of all the  
1094 objects in the `Object` catalog, to allow assessment of  
1095 the time variability of the fluxes. We recommend using  
1096 the `psfDiffFlux` column when generating light curves  
1097 because this quantity is less sensitive to flux from nei-  
1098 ghoring sources than `psfFlux`. In addition to `forced pho-`  
1099 `tometry` PSF fluxes, a number of boolean flags are also  
1100 included in the `ForcedSource` catalog.

1101 The `ForcedSource` catalog contains a total of 269 mil-  
1102 lion entries across 2.3 million unique objects.

### 3.2.4. DiaSource Catalog

1103  
1104 The `DiaSource` catalogs (NSF-DOE Vera C. Rubin  
1105 Observatory 2025i) contains data on all the `sources` de-  
1106 tected at  $> 5\sigma$  significance — including those associ-  
1107 ated with known Solar System objects — in the `dif-`  
1108 `ference_images`. Unlike `sources` detected in `visit_im-`  
1109 `ages`, `sources` detected in difference images (hereafter,  
1110 “DiaSource”) have gone through an association step in  
1111 which an attempt has been made to associate them into  
1112 underlying objects called “DiaObject”. The `DiaSource`  
1113 catalog consolidates all this information across multiple  
1114 visits and bands. The detections reported in the `Dia-`  
1115 `Source` catalog have not undergone deblending.

1116 The `DiaSource` catalog contains data for 3.1 million  
1117 `DiaSources` in DP1.

### 3.2.5. DiaObject Catalog

1118  
1119 The `DiaObject` catalog (NSF-DOE Vera C. Rubin  
1120 Observatory 2025j) contains the astrophysical objects  
1121 that `DiaSources` are associated with (i.e., the `DiaOb-`  
1122 `jects`). The `DiaObject` catalog contains only non-Solar

System Objects; Solar System Objects are, instead, recorded in the `SSObject` catalog. When a `DiaSource` is identified, the `DiaObject` and `SSObject` catalogs are searched for objects to associate it with. If no association is found, a new `DiaObject` is created and the `DiaSource` is associated to it. Along similar lines, an attempt has been made to associate `DiaObjects` across multiple bands, meaning the `DiaObject` catalog, like the `Object` catalog, contains data from multiple bands. Since `DiaObjects` are typically [transient](#) or variable (by the nature of their means of detection), the `DiaObject` catalog contains summary statistics of their fluxes, such as the mean and standard deviation over multiple epochs; users must refer to the `ForcedSourceOnDiaObject` catalog (see below) or the `DiaSource` catalog for single [epoch flux](#) measurements of `DiaObjects`.

The `DIAObject` catalog contains data for 1.1 million `DiaObjects` in `DP1`.

### 3.2.6. *ForcedSourceOnDiaObject Catalog*

The `ForcedSourceOnDiaObject` catalog ([NSF-DOE Vera C. Rubin Observatory 2025k](#)) is equivalent to the `ForcedSource` catalog, but contains [forced photometry](#) measurements obtained at the positions of all the `DiaObjects` in the `DiaObject` catalog.

The `ForcedSourceOnDiaObject` catalog contains a total of 197 million entries across 1.1 million unique `DiaObjects`.

## 3.3. *SSObject Catalog*

The `SSObject` catalog ([NSF-DOE Vera C. Rubin Observatory 2025l](#)) and the [Minor Planet Center Orbit database \(MPCORB\)](#) carry information about solar system objects. The `MPCORB` table provides the [Minor Planet Center](#)-computed orbital elements for all known asteroids, including those that Rubin discovered. For `DP1`, the `SSObject` catalog serves primarily to provide the mapping between the [International Astronomical Union \(IAU\)](#) designation of an object (listed in `MPCORB`), and the internal `ssObjectId` identifier, which is used as a key to find solar system object observations in the `DiaSource` and `SSSource` tables. The `SSObject` catalog contains data for 431 `SSObjects` in `DP1`.

### 3.3.1. *SSSource Catalog*

The `SSSource` catalog ([NSF-DOE Vera C. Rubin Observatory 2025m](#)) contains data on all `DiaSources` that are either associated with previously-known Solar System Objects, or have been confirmed as newly-discovered Solar System Objects by confirmation of their orbital properties. As entries in the `SSSource` catalog stem from the `DiaSource` catalog, they have all been

detected at  $> 5\sigma$  significance in at least one band. The `SSSource` catalog contains data for 5988 Solar System Sources.

### 3.3.2. *CcdVisit Catalog*

The `CcdVisit` catalog ([NSF-DOE Vera C. Rubin Observatory 2025n](#)) contains data for all `CCD` images from a single visit. In principle, this means nine entries per visit, however due to a variety of technical reasons, not all `CCDs` have data for each visit, and so the catalog may contain fewer than nine entries per visit. In addition to technical information, such as the on-sky coordinates of the central pixel and measured pixel scale, the `CcdVisit` catalog contains a range of data quality measurements, such as whole-image summary statistics for the `PSF` size, zeropoint, sky [background](#), sky noise, and quality of astrometric solution. It provides an efficient method to access `visit_image` properties without needing to access the image data. When combined with the data contained in the `Visit` table described in [§3.5](#), it provides a full picture of the telescope pointing and sky conditions at the time of observation.

The `CcdVisit` catalog contains 16071 entries (nine entries for each of the 1786 visits, minus three entries for one incomplete visit). This differs from the number of `visit_images` due to the more stringent requirements imposed to generate a science-ready image.

### 3.3.3. *Calibration Catalog*

The `Calibration` catalog is the reference catalog that was used to perform astrometric and photometric [calibration](#). It is a whole-sky catalog built specifically for `LSST`, as no single prior reference catalog had both the depth and coverage needed to calibrate `LSST` data. It combines data from multiple previous reference catalogs and contains only stellar sources. Full details on how the `Calibration` catalog was built are provided in [P. S. Ferguson et al. \(2025\)<sup>93</sup>](#). We provide a brief summary here.

For the *grizy* bands, the input catalogs were (in order of decreasing priority): [Dark Energy Survey \(DES\) Y6 Calibration Stars \(E. S. Rykoff et al. 2023\)](#); [Gaia-B or R Photometry \(Gaia\) \(XP\) Synthetic Magnitudes \(Gaia Collaboration et al. 2023a\)](#); the [Panoramic Survey Telescope and Rapid Response System \(Pan-STARRS\)1 3PI Survey \(K. C. Chambers et al. 2016\)](#); [Data Release 2 of the SkyMapper survey \(C. A. Onken et al. 2019\)](#); and [Data Release 4 of the VLT Survey Telescope \(VST\)](#)

<sup>93</sup> In [P. S. Ferguson et al. \(2025\)](#), the calibration reference catalog is referred to as “The Monster”. This terminology is also carried over to the `DP1` Butler.

1219 Asteroid Terrestrial-impact Last Alert System (ATLAS) 1270  
 1220 survey (T. Shanks et al. 2015). For the  $u$ -band, the input 1271  
 1221 catalogs were (in order of decreasing priority): Standard 1272  
 1222 Stars from Sloan Digital Sky Survey (SDSS) Data Re- 1273  
 1223 lease 16 (R. Ahumada et al. 2020); Gaia-XP Synthetic 1274  
 1224 Magnitudes (Gaia Collaboration et al. 2023a); and syn- 1275  
 1225 thetic magnitudes generated using Single Lens Reflex 1276  
 1226 (SLR), which estimates the  $u$ -band flux from the  $g$ -band 1277  
 1227 flux and  $g-r$  colors. This SLR estimates were used to 1278  
 1228 boost the number of  $u$ -band reference sources, as other- 1279  
 1229 wise the source density from the  $u$ -band input catalogs 1280  
 1230 is too low to be useful for the LSST.

1231 Only stellar sources were selected from each input cat- 1281  
 1232 alog. Throughout, the Calibration catalog uses the 1282  
 1233 DES bandpasses for the *grizy* bands and the SDSS band- 1283  
 1234 pass for the  $u$ -band; color transformations derived from 1284  
 1235 high quality sources were used to convert fluxes from the 1285  
 1236 various input catalogs (some of which did not use the 1286  
 1237 DES/SDSS bandpasses) to the respective bandpasses. 1287  
 1238 All sources from the input catalogs are matched to Gaia- 1288  
 1239 Data Release 3 (DR3) sources for robust astrometric in- 1289  
 1240 formation, selecting only isolated sources (i.e., no neigh- 1290  
 1241 bors within  $1''$ ).

1242 After collating the input catalogs and transforming 1291  
 1243 the fluxes to the standard DES/SDSS bandpasses, the 1292  
 1244 catalog was used to identify sources within a specific 1293  
 1245 region of the sky. This process generated a set of stan- 1294  
 1246 dard columns containing positional and flux informa- 1295  
 1247 tion, along with their associated uncertainties.

### 1248 3.3.4. Source and Object Designations

1249 To refer to individual sources or objects from the DP1 1297  
 1250 catalogs, one should follow the LSST DP1 naming con- 1298  
 1251 vention that has been registered with the International 1299  
 1252 Astronomical Union. Because the Source, Object, Dia- 1300  
 1253 aSource, DiaObject, and SSObject tables each have 1301  
 1254 their own unique IDs, their designations should differ. 1302  
 1255 In general, source and object designations should be- 1303  
 1256 gin with the string “LSST-DP1” (denoting the Legacy 1304  
 1257 Survey of Space and Time, Data Preview 1), followed 1305  
 1258 by a string specifying the table from which the source 1306  
 1259 was obtained. These strings should be “O” (for the Ob- 1307  
 1260 ject table), “S” (Source), “DO” (DiaObject), “DS” 1308  
 1261 (DiaSource), or “SSO” (SSObject). Following the table 1309  
 1262 identifier, the designation should contain the full unique 1310  
 1263 numeric identifier from the specified table (i.e., the ob- 1311  
 1264 jectId, sourceId, diaObjectId, diaSourceId, or ssObjec- 1312  
 1265 tId). Each component of the identifier should be sep- 1313  
 1266 arated by dashes, resulting in a designation such as 1314  
 1267 “LSST-DP1-TAB-123456789012345678”. In summary, 1315  
 1268 source designations should adhere to the formats listed 1316  
 1269 below:

- Object: LSST-DP1-O-609788942606161356 (for  
objectId 609788942606161356)
- Source: LSST-DP1-S-600408134082103129 (for  
sourceId 600408134082103129)
- DiaObject: LSST-DP1-DO-609788942606140532  
(for diaObjectId 609788942606140532)
- DiaSource: LSST-DP1-DS-600359758253260853  
(for diaSourceId 600359758253260853)
- SSObject: LSST-DP1-SSO-21163611375481943  
(for ssObjectId 21163611375481943)

1280 Tables that were not explicitly mentioned in the de-  
 1281 scription above do not have their own unique IDs, but  
 1282 are instead linked to one of the five tables listed above  
 1283 via a unique ID. For example, the ForcedSource table  
 1284 uses objectId, ForcedSourceOnDiaObject uses diaOb-  
 1285 jectId, SSSource uses diaSourceId and ssObjectId, and  
 1286 MPCORB uses ssObjectId.

### 1287 3.4. Maps

1288 Maps are two-dimensional visualizations of survey  
 1289 data. In DP1, these fall into two categories: Sur-  
 1290 vey Property Maps and Hierarchical Progressive Survey  
 1291 (HiPS) Maps (P. Fernique et al. 2015).

#### 1292 3.4.1. Survey Property Maps

1293 Survey Property Maps (NSF-DOE Vera C. Rubin Ob-  
 1294 servatory 2025o) summarize how properties such as ob-  
 1295 serving conditions or exposure time vary across the ob-  
 1296 served sky. Each map provides the spatial distribution  
 1297 of a specific quantity at a defined sky position for each  
 1298 band by aggregating information from the images used  
 1299 to make the deep\_coadd. Maps are initially created per-  
 1300 tract and then combined to produce a final consolidated  
 1301 map. At each sky location, represented by a spatial pixel  
 1302 in the Hierarchical Equal-Area iso-Latitude Pixelisation  
 1303 (HEALPix)(K. M. Górski et al. 2005) grid, values are  
 1304 derived using statistical operations, such as minimum,  
 1305 maximum, mean, weighted mean, or sum, depending on  
 1306 the property.

1307 DP1 contains 14 survey property maps. The avail-  
 1308 able maps describe total exposure times, observation  
 1309 epochs (one each for the earliest, mean, and latest ob-  
 1310 servation epoch), PSF size and shape (one for each  
 1311 of the  $e^1$  and  $e^2$  shape parameters; see §5.2), PSF  
 1312 magnitude limits, sky background and noise levels, as  
 1313 well as astrometric shifts (one each for right ascension  
 1314 and declination) and PSF distortions (one for each of  
 1315 the  $e^1$  and  $e^2$  shape parameters) due to wavelength-  
 1316 dependent atmospheric Differential Chromatic Refrac-  
 1317 tion (DCR) effects. They all use the dataset type

format `deep_coadd_<PROPERTY>_consolidated_map_<STATISTIC>`. For example, `deep_coadd_exposure_time_consolidated_map_sum` provides a spatial map of the total exposure time accumulated per sky position in units of seconds. All maps are stored in `HealSparse`<sup>94</sup> format. Survey property maps are only available via the `Data Butler` (§6.2.2).

Figure 10 presents three survey property maps for exposure time, PSF magnitude limit, and sky noise, computed for representative tracts and bands. Because full consolidated maps cover widely separated tracts, we use clipped per-tract views here to make the spatial patterns more discernible.

### 3.4.2. HiPS Maps

HiPS Maps (P. Fernique et al. 2015), offer an interactive way to explore seamless, multi-band tiles of the sky regions covered by DP1, allowing for smooth panning and zooming. DP1 provides multi-band HiPS images created by combining data from individual bands of `deep_coadd` and `template_coadd` images, using an improved version (Lust et al. in prep) of the algorithm presented in R. Lupton et al. (2004). These images are false-color representations generated using various filter combinations for the red, green, and blue channels.

The available filter combinations include `gri`, `izy`, `riz`, and `ugr` for both `deep_coadd` and `template_coadd`. Additionally, for `deep_coadd` only, we provide color blends such as `uug` and `grz`. Post-DP1, we plan to also provide single-band HiPS images for all `ugrizy` bands in both `Portable Network Graphics (PNG)` and `FITS` formats.

HiPS maps are only accessible through the HiPS viewer in the RSP Portal (§6.3) and cannot be accessed via the `Data Butler` (§6.2.2). All multi-band HiPS images are provided in `PNG` format.

### 3.5. Metadata

DP1 also includes `metadata` about the observations, which are stored in the `Visit` table. We distinguish it from a catalog as the data it contains was produced by the observatory directly, rather than the science pipelines. The `Visit` table contains technical data for each visit, such as telescope pointing, camera rotation, `airmass`, exposure start and end time, and total exposure time. Some of the information contained within the `Visit` table is also contained in the `CCDVisit` catalogue described in §3.2 (e.g., exposure time), although the latter also includes information produced by the pro-

cessing pipelines at a per-detector level, such as the PSF size and limiting magnitudes of a given `visit_image`.

## 3.6. Ancillary Data Products

DP1 also includes several ancillary data products. While we do not expect most users to need these, we describe them here for completeness. All the Data Products described in this section can only be accessed via the `Data Butler` (§6.2.2).

### 3.6.1. Standard Bandpasses

Figure 3 shows the full-system throughput of the six `LSSTComCam` filters. The corresponding transmission curves are provided as a DP1 data product. These datasets tabulate the full-system transmission of the six `LSSTComCam` filters as a function of wavelength and were used as a reference for the `LSSTComCam DP1` photometry. The `standard_passband` dataset is keyed by band and is stored in `Astropy Table` format.

### 3.6.2. Task configuration, log, and metadata

DP1 includes `provenance`-related data products such as task logs, `configuration` files, and task metadata. Configuration files record the parameters used in each processing task, while logs and `metadata` contain information output during processing. These products help users understand the processing setup and investigate potential processing failures.

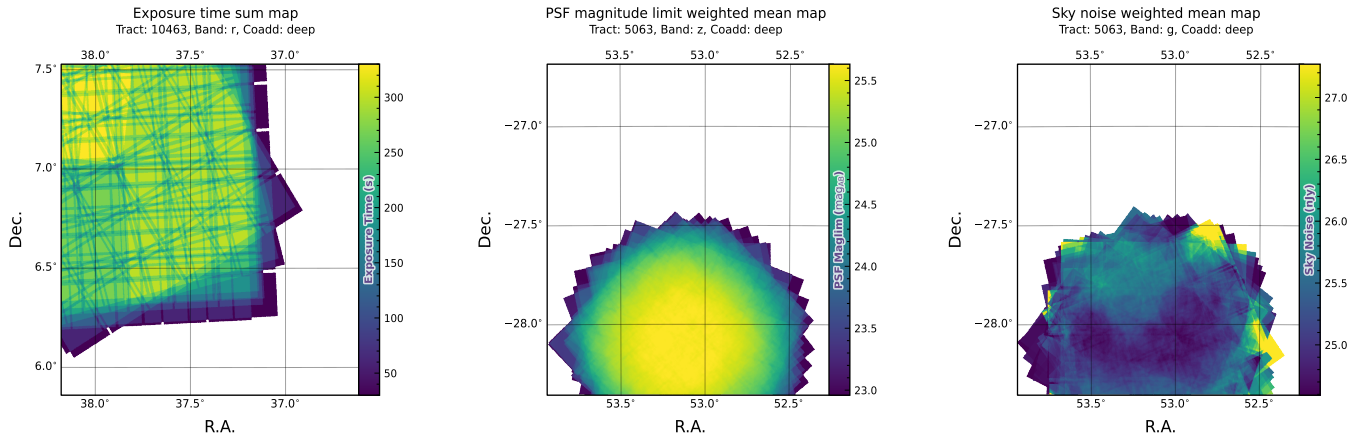
### 3.6.3. Calibration Data Products

Calibration data products include a variety of images and models that are used to characterize and correct the performance of the camera and other system components. These include bias, dark, and flat-field images, `Photon Transfer Curve (PTC)` gains, brighter-fatter kernels (P. Antilogus et al. 2014), charge transfer inefficiency (CTI) models, linearizers, and illumination corrections. For flat-field corrections, DP1 processing used combined flats, which are averaged from multiple individual flat-field exposures to provide a stable `calibration`. These `calibration` products are essential inputs to `Instrument Signal Removal (ISR)` (§4.2.1). While these products are included in DP1 for transparency and completeness, users should not need to rerun ISR for their science and are advised to start with the processed `visit_image`.

## 4. DATA RELEASE PROCESSING

`Data Release Processing (DRP)` is the systematic processing of all Rubin Observatory data collected up to a certain date to produce the calibrated images, catalogs of detections, and derived data products described

<sup>94</sup> A sparse `HEALPix` representation that efficiently encodes data values on the celestial sphere. <https://healsparse.readthedocs.io>



(a) Exposure time sum map for `deep_coadd tract 10463`, `r`-band in field `Rubin_SV_38_7` (b)  $5\sigma$  PSF magnitude limit weighted mean map for `deep_coadd tract 5063`, `z`-band in field `ECDFS` (c) Sky noise weighted mean map for `deep_coadd tract 5063`, `g`-band in field `ECDFS`

**Figure 10.** Examples of survey property maps from Rubin DP1 across different bands, clipped to the boundary of a single tract for visual clarity.

1412 in Section 3. DP1 was processed entirely at the [United States Data Facility \(USDF\)](#) at SLAC using 17,024 CPU  
 1413 hours.<sup>95</sup>

1414  
 1415 This section describes the pipeline algorithms used to  
 1416 produce DP1 and how they differ from those planned for  
 1417 full-scale LSST data releases. Data Release Production  
 1418 consists of four major stages: (1) single-frame process-  
 1419 ing, (2) calibration, (3) coaddition, and (4) difference  
 1420 image analysis (DIA).

1421 **4.1. LSST Science Pipelines Software**

1422 The LSST Science Pipelines software ([Rubin Observa-  
 1423 tory Science Pipelines Developers 2025](#); [J. D. Swinbank  
 1424 et al. 2020](#)) will be used to generate all Rubin Obser-  
 1425 vatory and LSST data products. They provide both  
 1426 the [algorithm](#) and [middleware](#) frameworks necessary to  
 1427 process raw data into science-ready data products, en-  
 1428 abling analysis by the Rubin scientific community. Ver-  
 1429 sion v29.1 of the pipelines was used to produce DP1<sup>96</sup>.

1430 **4.2. Single Frame Processing**

1431 **4.2.1. Instrument Signature Removal**

1432 The first step in processing `LSSTComCam` images is  
 1433 to correct for the effects introduced by the telescope and  
 1434 detector. Each sensor and its readout amplifiers can  
 1435 vary slightly in performance, causing images of even a  
 1436 uniformly illuminated focal plane to exhibit discontinu-  
 1437 ities and shifts due to detector effects. The `ISR` pipeline

1438 aims to recover the original astrophysical signal as best  
 1439 as possible and produce science-ready single-epoch im-  
 1440 ages for source detection and measurement. A detailed  
 1441 description of the `ISR` procedures can be found in [P. Fag-  
 1442 relius & E. S. Rykoff \(2025\)](#) and [A. A. Plazas Malagón  
 1443 et al. \(2025\)](#). Figure 11 illustrates the model of detector  
 1444 components and readout electronics and their impact  
 1445 on the signal, tracing the process from photons incident  
 1446 on the detector surface to the final quantized values<sup>97</sup>  
 1447 recorded in the image files. The `ISR pipeline` essen-  
 1448 tially “works backward” through the signal chain, cor-  
 1449 recting the integer analog-to-digital units (ADU) raw  
 1450 camera output back to a floating-point number of pho-  
 1451 toelectrons created in the silicon. The physical detec-  
 1452 tor, represented on the left in Figure 11, is the source  
 1453 of effects that arise from the silicon itself, such as the  
 1454 dark current and the brighter-fatter effect ([A. A. Plazas  
 1455 et al. 2018](#); [A. Broughton et al. 2024](#)). After the inte-  
 1456 gration time has elapsed, the charge is shifted to the  
 1457 serial register and read out, which can introduce charge  
 1458 transfer inefficiencies and a clock-injected offset level.  
 1459 The signals for all amplifiers are transferred via cables  
 1460 to the `Readout Electronics Board (REB)`, during which  
 1461 crosstalk between the amplifiers may occur. The `Ana-  
 1462 log Signal Processing Integrated Circuit (ASPIC)` on the  
 1463 `REB` converts the analog signal from the detector into a  
 1464 digital signal, adding both quantization and a bias level  
 1465 to the image. Although the signal chain is designed to  
 1466 be stable and linear, the presence of numerous sources  
 1467 of non-linearity indicates otherwise.

<sup>95</sup> For future Data Releases, data processing will be distributed across the USDF, the French (FrDF) and UK (UKDF) data facilities.

<sup>96</sup> Documentation for this version is available at [https://pipelines.lsst.io/v/v29\\_1\\_1](https://pipelines.lsst.io/v/v29_1_1)

<sup>97</sup> The images written to disk by the camera have values that are integers that come from the ADC converting an analog voltage.

The *ISR* processing pipeline for *DP1* performs, in the following order: **Analogue-to-Digital Unit (ADU)** dithering to reduce quantization effects, serial overscan subtraction, saturation masking, gain normalization, crosstalk correction, parallel overscan subtraction, linearity correction, serial **CTI** correction, image assembly, bias subtraction, dark subtraction, brighter-fatter correction, defect masking and interpolation, variance plane construction, flat fielding, and amplifier offset (amp-offset) correction<sup>98</sup>. Flat fielding for *DP1* was performed using combined flats produced from twilight flats acquired with sufficient rotational dithering to mitigate artifacts from print-through stars, as described in §2.3.

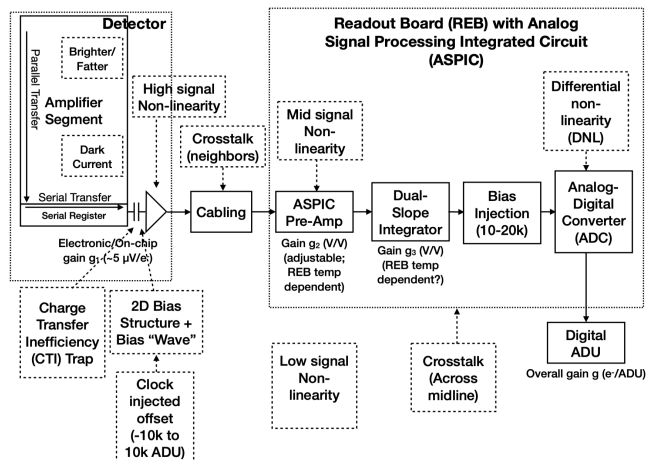


**Figure 11.** The model of the detector and REB components, labeled with the effects that they impart on signal.

#### 4.2.2. Background Subtraction

The background subtraction algorithms in the LSST Science Pipelines estimate and remove large-scale background signals from science imaging. Such signals may include sky brightness from airglow, moonlight, scattered light instrumental effects, zodiacal light, and diffuse astrophysical emission. In so doing, true astrophysical sources are isolated to allow for accurate detection and measurement.

To generate a **background** model, each post-*ISR* image is divided into superpixels of  $128 \times 128$  pixels. Pixels with a mask flag set that indicates that they contain no useful science data or that they contain **flux** from a preliminary source detection are masked. The iterative

<sup>98</sup> Amp-offset corrections are designed to address systematic discontinuities in background sky levels across amplifier boundaries. The implementation in the LSST Science Pipelines is based on the **Pan-STARRS** Pattern Continuity algorithm (C. Z. Waters et al. 2020).

$3\sigma$  clipped mean of the remaining pixels is calculated for each superpixel, constructing a **background** statistics image. A sixth-order Chebyshev polynomial is fit to these values on the scale of a single detector to allow for an extrapolation back to the native pixel resolution of the post-*ISR* image.

#### 4.3. Calibration

Stars are detected in each post-*ISR* image using a  $5\sigma$  threshold. Detections of the same star across multiple images are then associated to identify a consistent set of isolated stars with repeated observations suitable for use in PSF modeling, photometric **calibration**, and astrometric **calibration**.

Initial astrometric and photometric solutions are derived using only the calibration reference catalogs (see §3.2), and an initial PSF model is fit using PSFEx (E. Bertin 2011). These preliminary solutions provide approximate source positions, fluxes, and PSF shapes that serve as essential inputs to the **calibration** process, enabling reliable source matching, selection of high-quality stars, and iterative refinement of the final astrometric, photometric, and PSF models. These preliminary solutions are subsequently replaced by more accurate fits, as described in the following sections.

##### 4.3.1. PSF Modeling

PSF modeling in *DP1* uses the Piff (M. Jarvis et al. 2021) package. Our configuration of Piff utilizes its **PixelGrid** model with a fourth-order polynomial interpolation per **CCD**, except in the *u*-band, where star counts are insufficient to support a fourth-order fit. In this case, a second-order polynomial is used instead. Details on the choice of polynomial order, overall PSF modeling performance, and known issues are discussed in §5.2.

##### 4.3.2. Astrometric Calibration

Starting from the astrometric solution calculated in single frame processing (§4.2), the final astrometric solution is computed using the ensemble of visits in a given band that overlap a given **tract**. This allows the astrometric solution to be further refined by using all of the isolated point sources of sufficient signal-to-noise ratio in an image, rather than only those that appear in the reference catalog, as is done in single frame processing. Using multiple whole visits rather than a single detector also allows us to account for effects that impact the full focal plane, and for the proper motion and parallax of the sources.

In order to perform the fit of the astrometric solution, isolated point sources are associated between overlapping visits and with the **Gaia DR3** (Gaia Collaboration et al. 2023b) reference catalog where possible. The

1545 model used for DP1 consists of a static map from pixel  
 1546 space to an intermediate frame (the per-detector model),  
 1547 followed by a per-visit map from the intermediate frame  
 1548 to the plane tangent to the telescope boresight (the per-  
 1549 visit model), then finally a deterministic mapping from  
 1550 the tangent plane to the sky. The fit is done using the  
 1551 `gbdes` package (G. M. Bernstein et al. 2017), and a full  
 1552 description is given in C. Saunders (2024).

1553 The per-detector model is intended to capture quasi-  
 1554 static characteristics of the telescope and camera. Dur-  
 1555 ing *Rubin Operations*, the astrometric solution will al-  
 1556 low for separate epochs with different per-detector mod-  
 1557 els, to account for changes in the camera due to warm-  
 1558 ing and cooling and other discrete events. However, for  
 1559 DP1, LSSTComCam was assumed to be stable enough  
 1560 that all visits use the same per-detector model. The  
 1561 model itself is a separate two-dimensional polynomial for  
 1562 each detector. For DP1, a degree 4 polynomial was used;  
 1563 the degree of the polynomial mapping is tuned for each  
 1564 instrument and may be different for LSSTCam. Fur-  
 1565 ther improvements may be made by including a pixel-  
 1566 based astrometric offset mapping, which would be fit  
 1567 from the ensemble of astrometric residuals, but this is  
 1568 not included in the DP1 processing.

1569 The per-visit model attempts to account for the path  
 1570 of a photon from both atmospheric sources and those  
 1571 dependent on the telescope orientation. This model is  
 1572 also a polynomial mapping, in this case a degree 6 two-  
 1573 dimensional polynomial. Correction for DCR (§5.4) was  
 1574 not done for DP1, but will be included in LSSTCam pro-  
 1575 cessing during *Rubin Operations*. Future processing will  
 1576 also likely include a Gaussian Process fit to better ac-  
 1577 count for atmospheric turbulence, as was demonstrated  
 1578 by W. F. Fortino et al. (2021) and P. F. Léget et al.  
 1579 (2021).

1580 The final component of the astrometric calibration  
 1581 involves the positions of the isolated point sources in-  
 1582 cluded in the fit, which are described by five parameters:  
 1583 sky coordinates, proper motion, and parallax. While  
 1584 proper motions and parallaxes are not released for DP1,  
 1585 they are fitted for these sources in the astrometric solu-  
 1586 tion to improve the astrometric calibration.

#### 1587 4.3.3. Photometric Calibration

1588 Photometric calibration of the DP1 dataset is based  
 1589 on the *Forward Global Calibration Method (FGCM)*  
 1590 (D. L. Burke et al. 2018), adapted for the LSST Sci-  
 1591 ence Pipelines (H. Aihara et al. 2022; P. Fagrelius &  
 1592 E. S. Rykoff 2025). We used the FGCM to calibrate  
 1593 the full DP1 dataset with a forward model that uses a  
 1594 parameterized model of the atmosphere as a function of  
 1595 airmass along with a model of the instrument through-

1596 put as a function of wavelength. The FGCM process  
 1597 typically begins with measurements of the instrumental  
 1598 throughput, including the mirrors, filters, and detectors.  
 1599 However, because full scans of the LSSTComCam as-  
 1600 built filters and individual detectors were not available,  
 1601 we instead used the nominal reference throughputs for  
 1602 the Simonyi Survey Telescope and LSSTCam.<sup>99</sup> These  
 1603 nominal throughputs were sufficient for the DP1 cali-  
 1604 bration, given the small and homogeneous focal plane  
 1605 consisting of only nine ITL detectors. The FGCM atmo-  
 1606 sphere model, provided by MODTRAN (A. Berk et al.  
 1607 1999), was used to generate a look-up table for atmo-  
 1608 spheric throughput as a function of zenith distance at  
 1609 Cerro Pachón. This model accounts for absorption and  
 1610 scattering by molecular constituents of the atmosphere,  
 1611 including  $O_2$  and  $O_3$ ; absorption by water vapor; and  
 1612 Mie scattering by airborne aerosol particulates. Nightly  
 1613 variations in the atmosphere are modeled by minimiz-  
 1614 ing the variance in repeated observations of stars with  
 1615 a *Signal to Noise Ratio (SNR)* greater than 10, mea-  
 1616 sured using “compensated aperture fluxes”. These fluxes  
 1617 include a local background subtraction (see §4.2.2) to  
 1618 mitigate the impact of background offsets. The model  
 1619 fitting process incorporates all six bands (*ugrizy*) but  
 1620 does not include any gray (achromatic) terms, except  
 1621 for a linear assumption of mirror reflectance degrada-  
 1622 tion, which is minimal over the short duration of the  
 1623 DP1 observation campaign. As an additional constraint  
 1624 on the fit, we use a subset of stars from the reference  
 1625 catalog (P. S. Ferguson et al. 2025), primarily to con-  
 1626 strain the system’s overall throughput and establish the  
 1627 “absolute” calibration.

1628 Photometric transformation relations between LSST-  
 1629 Cam and LSSTComCam systems and other photomet-  
 1630 ric systems are under development and are provided in  
 1631 (M. N. Porter et al. 2026)

#### 1632 4.4. Visit Images and Source Catalogs

1633 With the final PSF models, WCS solutions, and pho-  
 1634 tometric calibrations in place, we reprocess each single-  
 1635 epoch image to produce a final set of calibrated visit  
 1636 images and source catalogs. Source detection is per-  
 1637 formed down to a  $5\sigma$  threshold using the updated PSF  
 1638 models, followed by measurement of PSF and aperture  
 1639 fluxes. These catalogs represent the best single-epoch  
 1640 source characterization, but they are not intended for  
 1641 constructing light curves. For time-domain analysis,  
 1642 we recommend using the *forced photometry* tables de-  
 1643 scribed in §4.6.2.

<sup>99</sup> Available at: <https://github.com/lstt/throughputs/tree/1.9>

## 4.5. Coaddition Processing

### 4.5.1. Coaddition

Only exposures with a *seeing* better than 1.7 arcseconds FWHM are included in the deep coadded images. For the template coadds, typically only the top third of visits with the best *seeing* are used (although see §3.1 for more details), resulting in an even tighter image quality cutoff for the template coadds. Exposures with poor PSF model quality, identified using internal diagnostics, are excluded to prevent contamination of the coadds with unreliable PSF estimates. The remaining exposures are combined using an inverse-variance weighted mean stacking algorithm.

To mitigate transient artifacts before coaddition, we apply the artifact rejection procedure described in Y. Al-Sayyad (2018) that identifies and masks features such as satellite trails, optical ghosts, and cosmic rays. It operates on a time series of PSF-matched images resampled onto a common pixel grid (“warps”) and leverages their temporal behavior to distinguish persistent astrophysical sources from transient artifacts.

Artifact rejection uses both direct (where no PSF-matching is performed) and PSF-matched warps, homogenized to a standard PSF of 1.8 arcseconds FWHM, broadly consistent with the 1.7 arcsecond FWHM *seeing* threshold used in data screening. A sigma-clipped mean of the PSF-matched warps serves as a static sky model, against which individual warps are differenced to identify significant positive and negative residuals. Candidate artifact regions are classified as *transient* if they appear in less than a small percentage of the total number of exposures, with the threshold based on the number of visits,  $N$ , as follows:

- $N = 1$  or  $2$ : threshold = 0 (no clipping).
- $N = 3$  or  $4$ : threshold = 1.
- $N = 5$ : threshold = 2.
- $N > 5$ : threshold =  $2 + 0.03N$ .

Identified *transient* regions are masked before coaddition, improving image quality and reducing contamination in derived catalogs.

### 4.5.2. Detection, Deblending and Measurement

After constructing coadded images, sources are detected in each band, merged across bands, deblended, and measured to generate the final object catalogs (§3.2). For each coadd in all six bands, we perform source detection at a  $5\sigma$  detection threshold and then adjust the background with a per-patch constant (coadds are built from background-subtracted images,

but the deeper detection on coadds redefines what is considered source versus background). Detections across bands are merged in a fixed priority order, *irzygu*, to form a union detection catalog, which serves as input to deblending.

Deblending is performed using the Scarlet Lite algorithm, which implements the same model as Scarlet (P. Melchior et al. 2018), but operates on a single pixel grid. This allows the use of analytic gradients, resulting in greater computational speed and memory efficiency.

*Object* measurement is then performed on the deblended detection footprints in each band. Measurements are conducted in three modes: independent per-band measurements, forced measurements in each band, and multiband measurements.

Most measurement algorithms operate through a single-band plugin system, largely as originally described in J. Bosch et al. (2018). The same plugins are run separately for each object on a deblended image, which uses the Scarlet model as a template to re-weight the original noisy coadded pixel values. This effectively preserves the original image in regions where objects are not blended, while dampening the noise elsewhere.

A reference band is chosen for each object based on detection significance and measurement quality using the same priority order as detection merging (*irzygu*) and a second round of measurements is performed in forced mode using the shape and position from the reference band to ensure consistent colors (J. Bosch et al. 2018).

Measurement algorithm outputs include object fluxes, centroids, and higher-order moments thereof like sizes and shapes. A variety of *flux* measurements are provided, from aperture fluxes and forward modeling algorithms.

Composite model (CModel) magnitudes (K. Abazajian et al. 2004; J. Bosch et al. 2018) are used to calculate the extendedness parameter, which functions as a star-galaxy classifier. Extendedness is a binary classifier that is set to 1 if the PSF model flux is less than 98.5% of the (free, not forced) CModel flux in a given band. Additionally, the extendedness in the reference band is provided as a separate column for convenience as a multiband star-galaxy classification, and is recommended generally but also specifically for objects with low signal-to-noise ratio in some bands.

Gaussian-Aperture-and-PSF (Gaussian Aperture and PSF (GAaP) K. Kuijken 2008; A. Kannawadi 2025) fluxes are provided to ensure consistent galaxy colors across bands. Sérsic model (J. L. Sérsic 1963; J. L. Sérsic 1968) fits are run on all available bands simultaneously (MultiProFit, D. S. Taranu 2025). The resulting Sérsic model fluxes are provided as an alternative to CModel

and are intended to represent total galaxy fluxes. Like CModel, the Sérsic model is a Gaussian mixture approximation to a true Sérsic profile, convolved with a Gaussian mixture approximation to the PSF. Sérsic model fits also include a free centroid, with all other structural parameters shared across all bands. That is, the intrinsic model has no color gradients, but the convolved model may have color gradients if the PSF parameters vary significantly between bands.

CModel measurements use a double “shapelet” (A. Refregier 2003) PSF model with a single shared shape. The Sérsic fits are intended to use a double Gaussian with independent shape parameters for each component. Due to a pipeline misconfiguration, the Sérsic fits actually used the shapelet PSF parameters, with the higher-order terms ignored (since MultiProFit does not support shapelet PSFs). This bug is not expected to impact the galaxy fluxes significantly, since the higher-order shapelet PSF parameters tend to be small, and the fix will be applied in future campaigns. Either way, the double Gaussian PSF parameters are included for each object.

Further details on the performance of these algorithms are found in §5.7.

#### 4.6. Variability Measurement

##### 4.6.1. Difference Imaging Analysis

Difference Image Analysis (DIA) uses the decorrelated Alard & Lupton image differencing algorithm (D. J. Reiss & R. H. Lupton 2016). We detected both positive and negative DIASources at  $5\sigma$  in the difference image. Sources with footprints containing both positive and negative peaks due to offsets from the template position or blending were fit with a dipole centroid code, which simultaneously fits offset positive and negative PSFs. We filter the resulting DIASource catalog to remove detections with pixel flags indicative of artifacts, non-astrophysical trail lengths, or unphysically negative direct fluxes. Finally, we perform a simple spatial association of DIASources into DIAObjects using a one-arcsecond matching radius.

The Machine Learning reliability model applied to DP1 was developed with the aim to meet the latency requirements for Rubin Alert Production when executed on CPUs. Accordingly we developed a relatively simple model: a Convolutional Neural Network with three convolutional layers, and two fully connected layers. The convolutional layers have a  $5 \times 5$  kernel size, with 16, 32, and 64 filters, respectively. A max-pooling layer of size 2 is applied at the end of each convolutional layer, followed by a dropout layer of 0.4 to reduce overfitting. The last fully connected layers have sizes of 32 and 1. The ReLU

activation function is used for the convolutional layers and the first fully connected layer, while a sigmoid function is used for the output layer to provide a probabilistic interpretation. The cutouts are generated by extracting postage stamps of  $51 \times 51$  pixels centered on the detected sources. The input data of the model consist of the template, science, and difference image stacked to have an array of shape (3, 51, 51). The model is implemented using PyTorch (J. Ansel et al. 2024). The Binary Cross Entropy loss function was used, along with the Adaptive Moment Estimation (Adam) optimizer with a fixed learning rate of  $1 \times 10^{-4}$ , weight decay of  $3.6 \times 10^{-2}$ , and a batch size of 128. The final model uses the weights that achieved the best precision/purity for the test set. Training was done on the SLAC Shared Scientific Data Facility (S3DF) with an NVIDIA model L40S GPU.

The model was initially trained using simulated data from the second DESC Data Challenge (DC2; (LSST Dark Energy Science Collaboration (LSST DESC) et al. 2021)) plus randomly located injections of PSFs to increase the number of real sources, for a total of 89,066 real sources. The same number of bogus sources were selected at random from non-injected DIASources. Once the LSSTComCam data were available, the model was fine-tuned on a subset of the data containing 183,046 sources with PSF injections. On the LSSTComCam test set, the model achieved an accuracy of 98.06%, purity of 97.87%, and completeness of 98.27%. As discussed in §5.8, the injections used to train this model version do not capture all types of astrophysical variability, so performance on the test set will not be representative for variable stars, comets, and other types of variable objects. The machine-learning reliability score, reported in the reliability column of the DIASource catalog, is a scalar value between 0 and 1 that quantifies the model’s confidence that a given detection is astrophysical.

##### 4.6.2. Light Curves

To produce light curves, we perform multi-epoch forced photometry on both the direct visit images and the difference images. For light curves we recommend the forced photometry on the difference images (psfDiffFlux on the ForcedSource Table), as it isolates the variable component of the flux and avoids contamination from static sources. In contrast, forced photometry on direct images includes flux from nearby or blended static objects, and this contamination can vary with seeing. Centroids used in the multi-epoch forced photometry stage are taken either from object positions measured on the coadds or from the DIAObjects (the associated DIASources detected on difference images).

### 4.6.3. Solar System Processing

Solar system processing in DP1 consists of two key components: the association of observations (sources) with known solar system objects, and the discovery of previously unknown objects by linking sets of *tracklets*<sup>100</sup>.

The association component begins by generating expected positions for all objects in the Minor Planet Center orbit catalog, using ephemerides computed with the *Sorcha* survey simulation toolkit (Merritt et al., in press)<sup>101</sup>. To enable fast lookup of objects potentially present in an observed visit, we use the *mpsky* package (M. Juric 2025). In each image, the closest *DiaSource* within 1 arcsecond of a known solar system object’s predicted position is associated to that object. In DP1 we used a simple positional association to tag *DiaSources* that are likely observations of known asteroids. The 1 arcsecond radius is intentionally generous; we did not see evidence of mismatches at DP1 depth and volume. This radius will be tuned for future processing campaigns.

The discovery component of Solar System processing uses the *heliolinx* package<sup>102</sup>, which provides tools for asteroid identification and linking (A. Heinze et al. 2023). The repository contains code for the following tasks:

- Tracklet creation with `make_tracklets`
- Multi-night *tracklet* linking with an algorithm
- Linkage post processing (orbit fitting, outlier rejection, and de-duplication) with `link_purify`

The inputs to the discovery processing comprised all sources detected in difference images, regardless of whether they were tagged in the association step. These inputs were produced by an early processing of *LSST-ComCam* commissioning data, some of which were later rejected during DP1 processing and therefore do not appear in the final DP1 data products.

About 10% of all commissioning visits targeted the near-ecliptic field *Rubin\_SV\_38\_7*, chosen to facilitate asteroid discovery. *Rubin\_SV\_38\_7* produced the vast majority of asteroid discoveries in DP1, as expected, but a few were found in off-ecliptic fields as well.

Tracklet creation with `make_tracklets` used an upper limit angular velocity of 1.5 deg/day, faster than

any main belt asteroid and in the range of many *Near-Earth Object (NEO)* discoveries. While no formal minimum angular velocity was imposed, in practice it would be unlikely to detect objects moving slower than about 0.01 deg day<sup>-1</sup>. To minimize false *tracklets* from fields observed multiple times per night, the minimum *tracklet* length was set to three detections, and a minimum on-sky motion of five arcseconds was required for a valid *tracklet*. To claim a discovery candidate, we required *tracklets* to be linked across at least three nights.

Multi-night *tracklet* linking is the heart of Solar system discovery, which connects (“links”) *tracklets* belonging to the same object over a series of nights. It employs the *HelioLinC3D* algorithm (S. Eggl et al. 2020; A. Heinze et al. 2022), a refinement of the original *HelioLinC* algorithm of M. J. Holman et al. (2018). Each processing run tested each *tracklet* with 324 different hypotheses spanning heliocentric distances from 1.5 to 9.8 *astronomical unit (au)* and radial velocities spanning the full range of possible bound orbits (eccentricity 0.0 to nearly 1.0). The upper limit of 10 *au* was chosen because searches targeting more distant populations require different parameter choices. This range of distance encompasses all main belt asteroids and Jupiter Trojans, as well as many comets and Mars-crossers and some *NEOs*. A dedicated search for objects at heliocentric distances out to 50 *au* was also conducted; no distant objects were detected, consistent with expectations for the size of the DP1 data set. Smaller heliocentric distances were not attempted here because nearby objects move rapidly across the sky and hence were not likely to remain long enough in an *LSSTComCam* field to be discovered.

Candidate linkages, defined as groups of *tracklets* whose propagated orbits cluster within a radius of  $1.33 \times 10^3$  *au* at 1 *au*, are identified, then post-processed via `link_purify` to yield a final, non-overlapping set of high-confidence asteroid candidates, ranked by orbit-fit residuals and related metrics. While *heliolinx* can produce false-positive or redundant raw linkages by design, these are filtered during post-processing by `link_purify`, which applies a Rubin-specific, more stringent version of the MPC validation rules<sup>103</sup>. This step both rejects spurious linkages and deduplicates multiple hypotheses for the same object, ensuring that only the highest-quality, non-redundant linkages are carried forward for orbit determination and for distinguishing new discoveries from rediscoveries of known objects.

<sup>100</sup> A *tracklet* is defined as two or more detections of a moving object candidate taken in close succession in a single night.

<sup>101</sup> Available at <https://github.com/dirac-institute/sorcha>

<sup>102</sup> <https://github.com/heliolinx/heliolinx>

<sup>103</sup> <https://minorplanetcenter.net/mpcops/documentation/identifications/additional/>

## 5. PERFORMANCE CHARACTERIZATION AND KNOWN ISSUES

In this section, we provide an assessment of the DP1 data quality and describe known issues.

### 5.1. Sensor Anomalies and ISR

In addition to the known detector features identified before LSSTComCam commissioning, most of which are handled by the ISR processing (see §4.2.1), we discovered a number of new types of anomalies in the DP1 data. Since no corrections are currently available for these anomalies, they are masked and excluded from downstream data products.

#### 5.1.1. Vampire Pixels

“Vampire” pixels are visible on the images as a bright defect surrounded by a region of depressed flux, as though the defect is stealing charge from its neighboring pixels. Figure 12 shows an example of a vampire pixel near the center of R22\_S11 on an *r*-band flat.

From studies on evenly illuminated images, vampires appear to conserve charge. Unfortunately, no unique optimum way exists to redistribute this stolen flux so, following visual inspection, a defect mask was created to exclude them from processing. We have found some similar features on the ITL detectors on LSSTCam, and will use the same approach to exclude them.

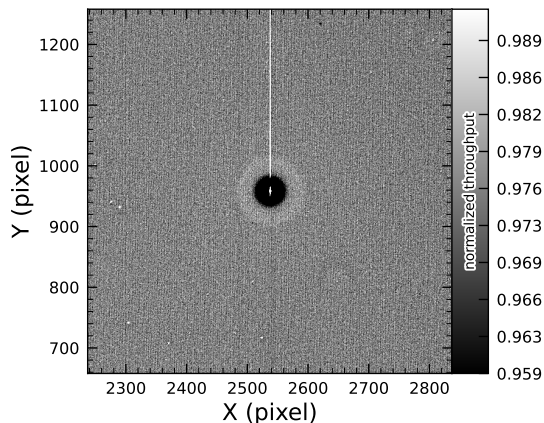


**Figure 12.** A large vampire pixel near the center of R22\_S11, as seen on the *r*-band flat. This clearly shows the central hot “vampire” pixels, surrounded by a region of depressed signal, with a brighter ring surrounding that caused by the local electric field effects. The charge contained in the central pixels is incompletely shifted as the image is read, and that charge leaks out into subsequent rows as they are shifted through the remnant charge. The columns that contain the hot pixels are masked as defects in all processing, as this feature cannot be otherwise corrected.

### 5.1.2. Phosphorescence

Some regions of the LSSTComCam CCD raft were seen to contain large numbers of bright defects. An example is shown in Figure 13 in a *g*-band flat. On further investigation, it appears that on some detectors a layer of photoresist wax was incompletely removed from the detector surface during production. As this wax is now trapped below the surface coatings, there is no way to physically clean these surfaces. If this wax responded to all wavelengths equally, then it would likely result in quantum efficiency dips, which might be removable during flat correction. However, it appears that this wax is slightly phosphorescent, with a decay time on the order of minutes, resulting in the brightness of these defects being dependent on the illumination of prior exposures. The worst of these regions were excluded with manual masks.

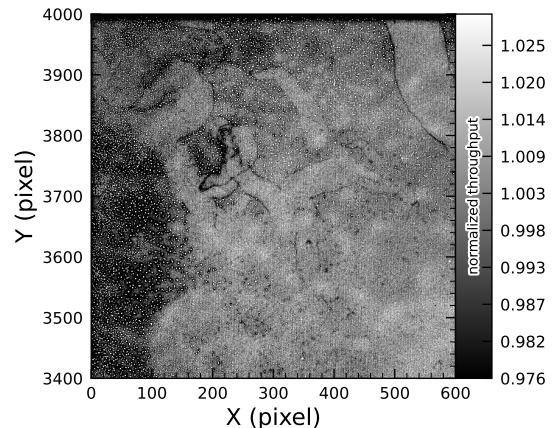


**Figure 13.** The top left corner of R22\_S01 in the *g*-band flat, showing the many small defect features that are caused by the remnant photoresist wax. A single large defect box masks this region from further analysis to prevent these features from contaminating measurements.

### 5.1.3. Crosstalk

Crosstalk refers to unwanted signal interference between adjacent pixels or amplifiers. We use an average inter-amp crosstalk correction based on laboratory measurements with LSSTCam. These average corrections proved satisfactory, and so have been used as-is for DP1 processing. There are, however, some residual crosstalk features present post-correction, with a tendency towards over-subtraction. Figure 14 shows an example of a bright star with over-subtracted crosstalk residuals visible on neighboring amplifiers to both sides on exposure 2024120600239, detector R22\_S02.

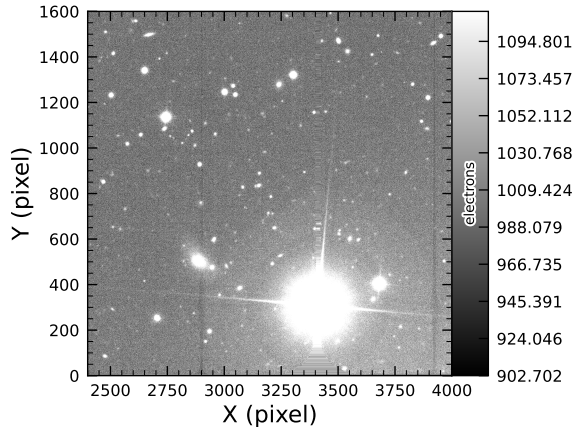


**Figure 14.** An example of a bright star with over-subtracted crosstalk residuals visible on neighboring amplifiers to both sides (exposure 2024120600239, detector R22\_S02). The horizontal banding stretching from the center of the star shows the interpolation stretching covering the saturated core and the ITL edge bleed near the serial register.

#### 5.1.4. Bleed Trails

Bleed trails are produced when charge from saturated pixels spills into adjacent pixels. Bleed trails were anticipated on LSSTComCam sensors, but they appear in more dramatic forms than had been expected. As a bleed trail nears the serial register, it fans out into a “trumpet” shaped feature. Although bright, these features do not have consistently saturated pixels. In DP1 these “edge bleeds” were identified and masked.

Saturated sources can create a second type of bleed, where the central bleed drops below the background level. The depressed columns along these trails extend across the entire readout column of the detector, crossing the detector mid-line. We developed a model for these to identify which sources are sufficiently saturated to result in such a trail, which is then masked. As this kind of trail appears only on the ITL detectors, we’ve named these features “ITL dips”. Figure 15 shows an example of a bright star exhibiting the “ITL dip” phenomenon on exposure: 2024121000503, detector: R22\_S21.

#### 5.2. PSF Models

To characterize PSF performance, we use adaptive second moments (G. M. Bernstein & M. Jarvis 2002) measured on PSF stars and on the PSF model using the HSM implementation (C. Hirata & U. Seljak 2003; R. Mandelbaum et al. 2005). All measurements are expressed in the pixel coordinate frame of each detector. We characterize the performance of the PSF using the classical trace of the second moment matrix  $T$ , along

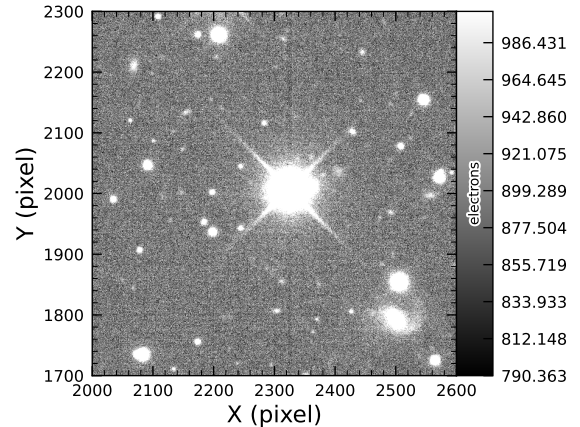


**Figure 15.** A bright star showing the “ITL dip” phenomenon, in which a dark trail extends out from the star to the top and bottom edges of the detector (exposure: 2024121000503, detector: R22\_S21).

with the ellipticity parameters  $e^1$  and  $e^2$ . Measurements on the observed PSF stars are denoted as  $T_{\text{PSF}}$ ,  $e_{\text{PSF}}^1$ ,  $e_{\text{PSF}}^2$ , while those from PSF models are denoted as  $T_{\text{model}}$ ,  $e_{\text{model}}^1$ ,  $e_{\text{model}}^2$ . We compare two PSF modeling approaches:

- Piff with second-order polynomial interpolation (Piff O2), the pipeline’s default, and
- Piff with fourth-order polynomial interpolation (Piff O4), which serves as the final DP1 PSF model.

Table 5 summarizes each model’s ability to reconstruct the mean  $T$ ,  $e^1$ , and  $e^2$  on LSSTComCam. Both models exhibit a negative residual bias in the reconstructed PSF size, with Piff O4 providing improved performance over Piff O2.

An alternative approach to evaluating the performance of the PSF model is to examine the average  $\delta T/T$ , where  $\delta T$  is  $T_{\text{PSF}} - T_{\text{model}}$ , across visits, projected onto focal-plane coordinates, as shown in Figure 16. Piff reveals strong spatial correlations in the residuals, including a systematic offset consistent with the results presented in Table 5. The presence of these spatial structures motivated the adoption of fourth-order polynomial interpolation in all bands except  $u$ -band. Although not shown in Figure 16, residual patterns persist even with third-order interpolation, indicating that it is insufficient to capture the complexity of the PSF variation. Increasing the interpolation order to five would nominally reduce the residuals further, but the limited number of stars available on some CCDs would not provide adequate constraints for such a model, while the resulting improvement would likely be minimal. Preliminary

**Table 5.** Observed mean values and comparison of model residuals, across all visits and filters

Quantity	Observed	Piff O2	Piff O4
		$\times 10^{-4}$	$\times 10^{-4}$
$\langle T \rangle$ (pixel <sup>2</sup> )	$11.366 \pm 0.003$		
$\langle e^1 \rangle$	$(-6.07 \pm 0.05) \times 10^{-3}$		
$\langle e^2 \rangle$	$(-4.57 \pm 0.05) \times 10^{-3}$		
$\langle e \rangle$	$(8.794 \pm 0.004) \times 10^{-2}$		
$\langle \delta T/T \rangle$		$-4.0 \pm 0.2$	$-5.0 \pm 0.2$
$\langle \delta e^1 \rangle$		$0.6 \pm 0.1$	$0.5 \pm 0.1$
$\langle \delta e^2 \rangle$		$0.0 \pm 0.1$	$0.0 \pm 0.1$

2059 analysis of LSSTCam data in the laboratory at SLAC  
 2060 National Accelerator Laboratory (SLAC) shows that the  
 2061 ITL sensors exhibit the same pattern as ITL sensors on  
 2062 LSSTComCam.

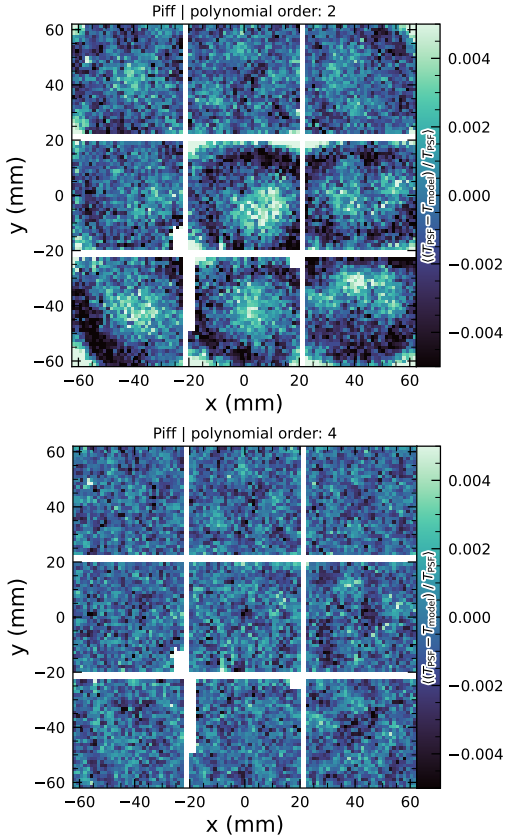


**Figure 16.** Average across all visits of  $\delta T/T$  for Piff O2 and Piff O4 modeling on LSSTComCam. Averages are computed using a  $120 \times 120$  binning.

2065 Another way to look at the PSF modeling quality is  
 2066 via whisker plots of the PSF second and fourth moments

2067 and their modeling residuals projected on a part of the  
 2068 sky. In addition to the second moment, the spin-2 fourth  
 2069 moments,  $e^{(4)}$ , are defined as:

$$e_1^{(4)} = M_{40} - M_{04}$$

$$e_2^{(4)} = 2(M_{31} - M_{13}),$$

2070  
 2071  
 2072 where  $M_{pq}$  are the standardized higher moments as defined in  
 2073 T. Zhang et al. (2023) measured on stars and PSF models. Figure 17  
 2074 shows the whisker plots of  $e$ ,  $e^{(4)}$  (top rows), and  $\delta e$ ,  $\delta e^{(4)}$   
 2075 in the ECDFS field. The direction of a whisker represents the orientation  
 2076 of the  $e$  or  $e^{(4)}$ , while the length represents the amplitude  $|e|$  or  
 2077  $|e^{(4)}|$ . We observe coherent patterns in both the PSF  
 2078 moments and the residuals, the latter of which warrants  
 2079 further investigation if it persists in future data releases.  
 2080

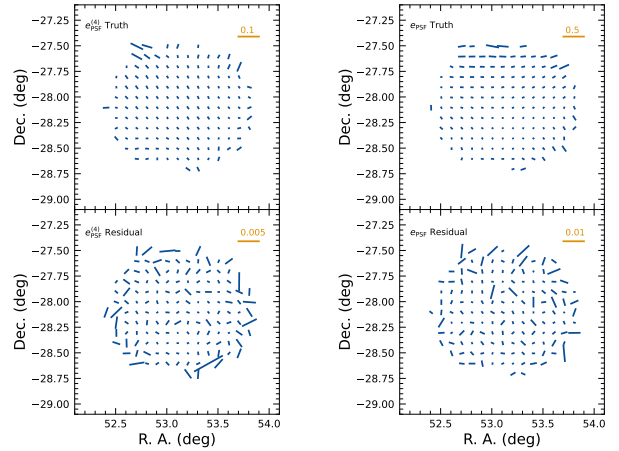


**Figure 17.** Whisker plots for the ECDFS field for  $e$ ,  $e^{(4)}$  and  $\delta e$ ,  $\delta e^{(4)}$ .

2084 Figure 18 shows a plot of  $\delta T/T$  versus stellar magnitude, which can reveal any dependencies between PSF size and flux. We also repeat this analysis in color bins

2087 to probe chromatic effects. Binning by color uncovers 2121  
 2088 a clear color dependence, as was also seen in DES (M. 2122  
 2089 Jarvis et al. 2021). The residual is consistent with Ta- 2123  
 2090 ble 5 and its cause is unknown. DP1 does not include the 2124  
 2091 color correction implemented in the DES Year 6 anal-  
 2092 ysis, T. Schutt et al. (2025). This will be included in  
 2093 processing of future data releases.

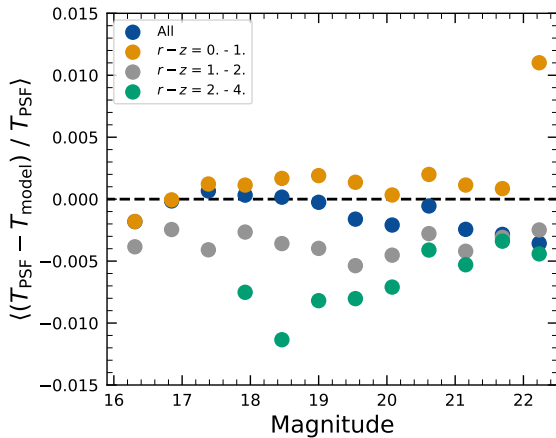


**Figure 18.** Binned  $\delta T/T$  as a function of magnitude across all visits and filters and in bins of stellar colors.

2094  
 2095 As noted in Rubin Observatory Science Pipelines De-  
 2096 velopers (2025), two key Piff features were not used in  
 2097 the DP1 processing. PSF color dependence was not im-  
 2098 plemented, and, while Rubin software allows Piff to work  
 2099 with sky coordinates (including WCS transformations),  
 2100 it does not yet correct for sensor-induced astrometric  
 2101 distortions such as tree rings (H. Y. Park et al. 2017).  
 2102 Both features are planned for upcoming releases.  
 2103

### 2104 5.3. Astrometry

2105 To characterize astrometric performance, we evaluate  
 2106 both internal consistency and agreement with an exter-  
 2107 nal reference. The primary measure of internal consis-  
 2108 tency is the repeatability of position measurements for  
 2109 the same object, defined as the RMS of the astrometric  
 2110 distance distribution for stellar pairs having a specified  
 2111 separation in arcminutes. We associate isolated point  
 2112 sources across visits and compute the rms of their fitted  
 2113 positions, rejecting any stars with another star within  
 2114  $2''$ . Figure 19 shows the mean per-tract rms astrometric  
 2115 error in RA for all isolated point sources, both after the  
 2116 initial calibration and after the final calibration, which  
 2117 includes proper motion corrections. The results indicate  
 2118 that the astrometric solution is already very good after  
 2119 the initial calibration. Global calibration yields only  
 2120 modest improvement, likely due to the short time span

of DP1 and the minimal distortions in the LSSTCom-  
 Cam. In the main survey, the longer time baseline and  
 greater distortions near the LSSTCam field edges will  
 make global calibration more impactful. An additional

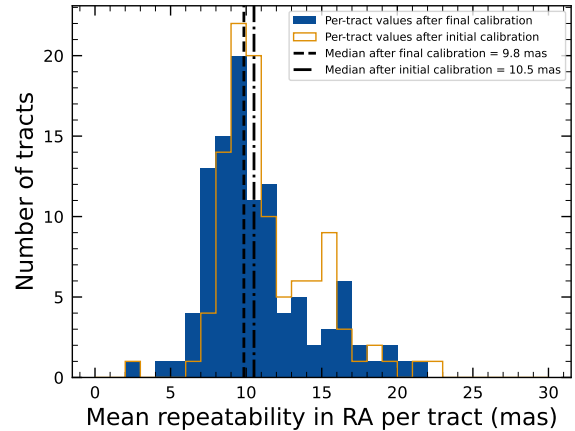


**Figure 19.** Mean per-tract astrometric repeatability of measurements of isolated point sources in RA in visits across all bands.

2125  
 2126 measure of internal consistency is the repeatability of  
 2127 separations between objects at a given distance. To com-  
 2128 pute this, we identify pairs of objects that are separated  
 2129 by a specified distance and measure their precise separa-  
 2130 tion during each visit in which both objects are ob-  
 2131 served. The scatter in these separation measurements  
 2132 provides an indication of the internal consistency of the  
 2133 astrometric model. Figure 20 shows the median separa-  
 2134 tion for pairs of objects separated by approximately 5  
 2135 arcminutes (referred to as “AM1”), computed per tract  
 2136 after the final calibration. These values are already ap-  
 2137 proaching the design requirement of 10 mas.  
 2138

2139 To assess external consistency, we consider the median  
 2140 separation between sources not included in the astro-  
 2141 metric fit and associated objects from a reference catalog  
 2142 (§3.3.3). For this, we use the Gaia DR3 catalog, with the  
 2143 object positions shifted to the observation epoch using  
 2144 the Gaia proper motion parameters. Figure 21 shows the  
 2145 median separation for each visit in the  $r$ -band in tract  
 2146 4849 in the ECDFS fields. The calculated values are  
 2147 almost all within 5 mas, well below the design require-  
 2148 ment of 50 mas for the main survey. By examining the  
 2149 astrometric residuals, we can assess whether there are  
 2150 distortions not accounted for by the astrometric model.  
 2151 In some cases, residuals from a single visit exhibit behav-  
 2152 ior consistent with atmospheric turbulence, as shown in  
 2153 Figure 22, which is characterized by a curl-free gradient  
 2154 field in the two-point correlation function of the residu-  
 2155 als (E-mode), P. F. Léget et al. (2021) and W. F. Fortino

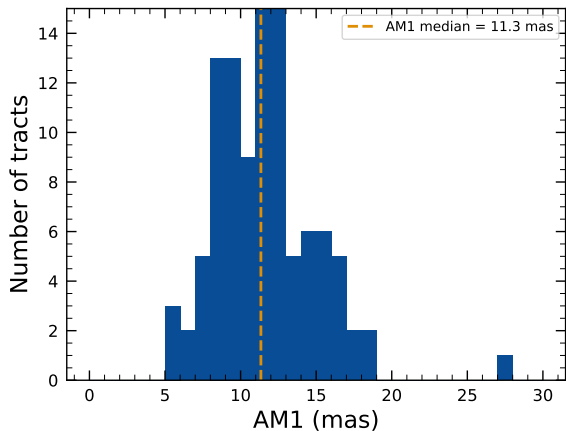


**Figure 20.** Median per-tract repeatability in separations between isolated point sources 5 arcmin apart (AM1) in visits across all bands.

et al. (2021). However, as seen in Figure 23, the residuals in many visits also have correlation functions with a non-negligible divergence-free B-mode, indicating that some of the remaining residuals are due to unmodeled instrumental effects, such as rotations between visits.

We can see unmodeled camera distortions by stacking the astrometric residuals over many visits as a function of the focal plane position. Figure 24 shows the median residuals in  $x$  and  $y$  directions for 1792 visits. Spatial structures are evident at the CCD level, as well as at the mid-line break, the discontinuity between the two rows of amplifiers, in the  $y$ -direction residuals. Further stacking all the detectors makes certain effects particularly clear. Figure 25 shows distortions very similar to those measured for an LSSTCam ITL sensor in a laboratory setting in J. H. Esteves et al. (2023).

#### 5.4. Differential Chromatic Refraction

DCR occurs when light passes through Earth’s atmosphere, refracting more for shorter wavelengths, which causes blue light to appear shifted closer to the zenith. This wavelength-dependent effect results in the smearing of point sources along the zenith direction, specifically parallel to the parallactic angle. The DCR effect is observable in LSSTComCam data, particularly in the angular offset versus  $g - i$  band magnitude difference plots, as shown in Figure 26. These plots include 228 visits selected to maximize the range of observed airmass, which spans 1.01–1.30 with a mean value of 1.13. When looking at data perpendicular to the parallactic angle, sources exhibit no discernible DCR effect, which is expected, and form a clear vertical distribution on the two-dimensional density plots in Figure 26.

In contrast, sources aligned with the parallactic angle exhibit a tilted, linear distribution, clearly demonstrating that the relationship between angular offset and the  $g - i$  band magnitude difference, thereby providing a visual indication of the DCR effect. The DCR effect will be addressed in future releases.

#### 5.5. Stellar Photometry

The photometric repeatability for isolated bright unresolved sources following the FGCM fits was excellent. For the 10% of unresolved sources withheld from the fit and having signal-to-noise ratios greater than 100, the photometric repeatability after applying chromatic correction was 7.1, 5.4, 5.4, 5.1, 5.9, and 6.5 mmag in the  $ugrizy$  bands respectively, across all fields. After accounting for photometric noise, the intrinsic photometric repeatability was approximately 4.8, 2.7, 1.7, 1.0, 2.0, and 1.1 mmag in  $ugrizy$ . The DP1 processing does not yet include chromatic corrections in the final photometry. In this case the delivered photometric repeatability was 3–8 mmag for  $grizy$ .

In Figure 27, we show the stellar loci for  $ugriz$  for unresolved sources in the DP1 Object table (§3.2). These unresolved sources were selected using the extendedness parameter (§3.2) in the Object catalog. This parameter is assigned a value of 0 (unresolved) or 1 (resolved) in each band based on the difference between the PSF and CModel magnitudes. The extendedness is set to 1 when this magnitude difference exceeds 0.016 mag, as the PSF flux for extended sources is biased low relative to the CModel flux. This method has been previously employed by the SDSS pipelines, and its statistical properties, including the optimal combination of information from different bands and repeated measurements, are discussed in C. T. Slater et al. (2020).

Figure 28 illustrates the behavior of the extendedness parameter. Its behavior in the  $g$  and  $r$  bands is similar, with unresolved sources scattered around the vertical line centered on zero. The width of the distribution increases towards fainter magnitudes. Resolved sources are found to the right and the dashed lines in the top panels show the adopted “star-galaxy” separation boundary. The morphology of the two color-magnitude diagrams in the bottom panels suggest that the unresolved sample suffers from increasing contamination by galaxies for  $r > 24$ . This behavior is consistent with simulation-based predictions from C. T. Slater et al. (2020).

#### 5.6. Detection Completeness on Coadds

We characterize completeness by injecting synthetic sources into coadded images, and by comparing source

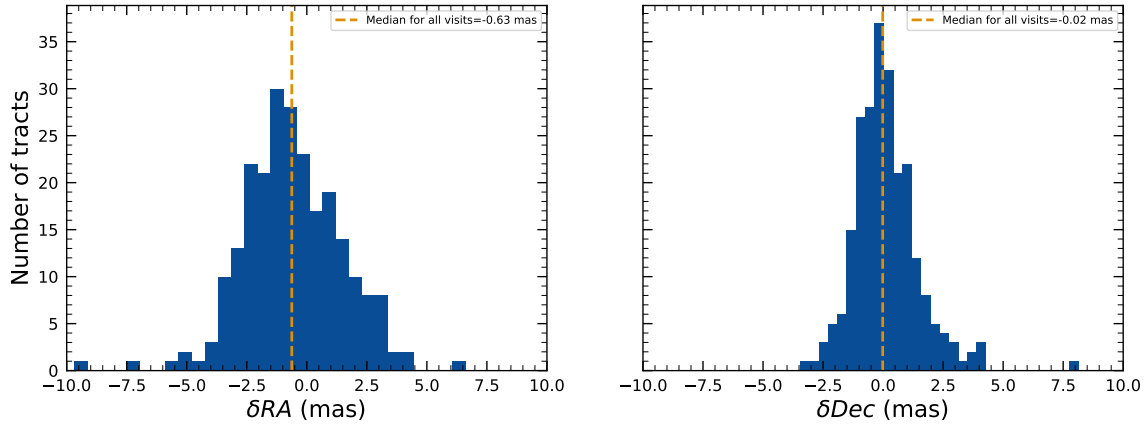


**Figure 21.** Median absolute offset for all visits in  $r$ -band in [tract 4849](#) in the ECDFS field. The offset is the difference between the positions of isolated point sources that were reserved from the astrometric fit and matched objects from the Gaia DR3 catalog.

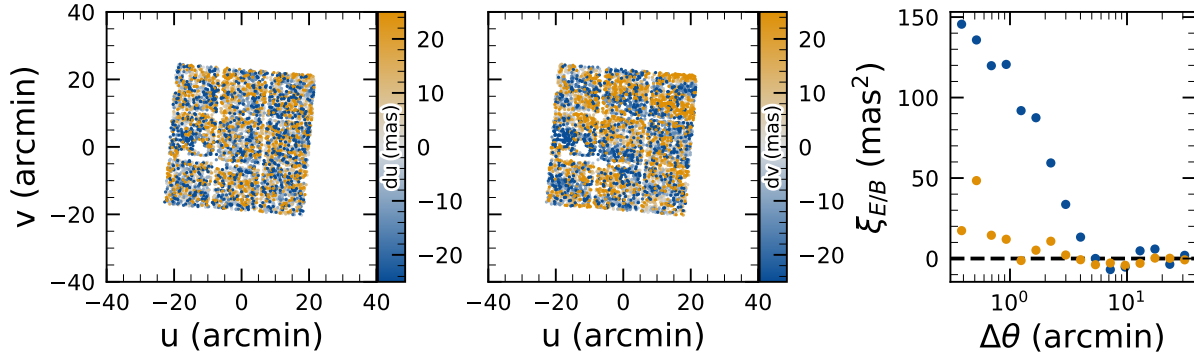


**Figure 22.** Astrometric residuals in  $u$  (left panel) and  $v$  (center panel) directions with the E (blue) and B (orange) modes of the two-point correlation function (right panel) seen in visit 2024120200359 in [tract 2393](#) in  $u$  band. The residuals show a wave-like pattern characteristic of atmospheric turbulence, and there is significant E-mode and negligible B-mode in the correlation function.

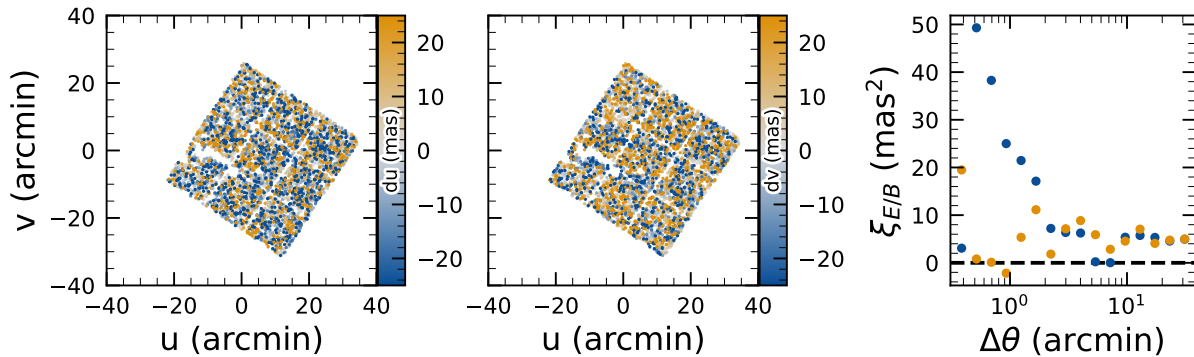


**Figure 23.** Astrometric residuals in  $u$  (left panel) and  $v$  (center panel) directions, with the E (blue) and B (orange) modes of the two-point correlation function (right panel) seen in visit 2024120700527 in [tract 2393](#) in  $u$  band. There are coherent residuals, but without the wave-like pattern seen in [Figure 22](#), and the correlation function has significant values for both E and B-modes.

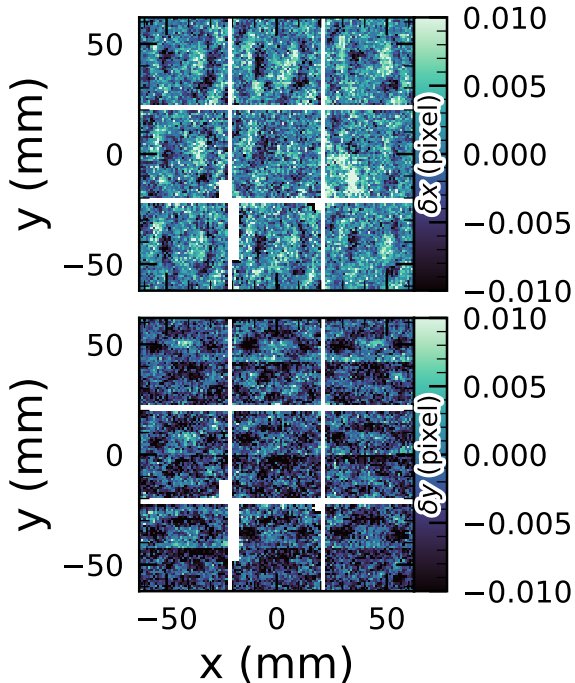


**Figure 24.** Median astrometric residuals as a function of focal plane position, shown in the left panel for the  $x$  direction and in the right panel for the  $y$  direction, for all nine [LSSTComCam](#) CCDs independently. The range of the color scale is  $\pm 0.01$  pixels, corresponding to 2 mas, showing that the effect is small.

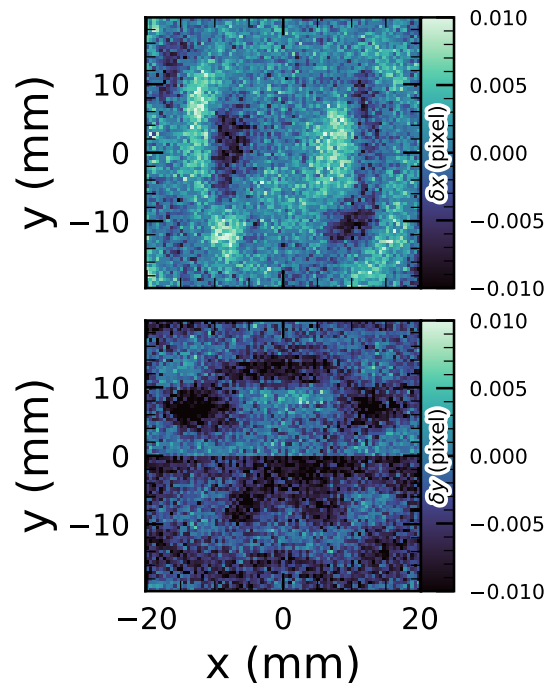


**Figure 25.** Median residuals as a function of pixel position, shown in the left panel for the  $x$  direction and in the right panel for the  $y$  direction. These residuals are aggregated across all nine CCDs that comprise the central [LSSTComCam](#) raft. The range of the color scale is  $\pm 0.01$  pixels, corresponding to 2 mas, showing that the effect is small.

2247 reference objects, in order of descending brightness, to  
 2248 the most likely target within a  $0''.5$  radius.

2249 We inject sources in 12 of the patches of the [ECDFS](#)  
 2250 region with the deepest coverage. The input catalog con-  
 2251 tains stars and galaxies from part of the [Data Challenge](#)  
 2252 [2 \(DC2\) simulations](#) ([LSST Dark Energy Science Col-  
 2253 laboration \(LSST DESC\) et al. 2021](#)), where the galaxies  
 2254 consist of an exponential disk and de Vaucouleurs ([G.  
 2255 de Vaucouleurs 1948, 1953](#)) bulge. To avoid deblender  
 2256 failures from excessive increases in object density, stars  
 2257 with a total `flux` (i.e., summed across all six bands)  
 2258 brighter than 17.5 mag are excluded, as are galaxies  
 2259 whose total `flux` is brighter than 15 mag or fainter than  
 2260 26.5 mag. Half of the remaining objects are selected for  
 2261 injection. Afterwards, individual bulge and disk compo-  
 2262 nents fainter than 29 mag are also excluded, both  
 2263 for computational expediency and because their struc-  
 2264 tural properties are less likely to be representative of  
 2265 real galaxies.

2267 [Figure 29](#) shows completeness as a function of mag-  
 2268 nitude for these injected objects in the [ECDFS](#) field.  
 2269 These completeness estimates are comparable to results  
 2270 from matching external catalogs. Matching to the Hub-

2271 ble Legacy Field catalog ([G. Illingworth et al. 2016](#);  
 2272 [K. E. Whitaker et al. 2019](#)) reaches 50% completeness  
 2273 at  $F775W = 26.13$ , or about  $i = 25.83$  from differences  
 2274 in matched object magnitudes. Similarly, completeness  
 2275 drops below 90% at  $VIS = 23.80$  from matching to  
 2276 Euclid Q1 ([Euclid Collaboration et al. 2025](#)) objects,  
 2277 equivalent to roughly  $i = 23.5$ . The Euclid imaging is of  
 2278 comparable or shallower depth, so magnitude limits at  
 2279 lower completeness percentages than 90% are unreliable,  
 2280 whereas the HST images cover too small and irregular of  
 2281 an area to accurately characterize 80-90% completeness  
 2282 limits.

2283 At the 80% completeness limit, nearly 20% of objects,  
 2284 primarily injected galaxies, are incorrectly classified as  
 2285 stars based on their reference band extendedness. Simi-  
 2286 larly, the fraction of correctly classified injected stars  
 2287 drops to about 50% at  $i = 23.8$  (corresponding to 90%  
 2288 completeness).

2289 This analysis has several caveats. The selection of  
 2290 objects for matching in any catalog is not trivial. Some  
 2291 fraction of the detections are spurious, particularly close  
 2292 to bright stars and their diffraction spikes. Additionally,  
 2293 some objects lie in masked regions of one survey but not

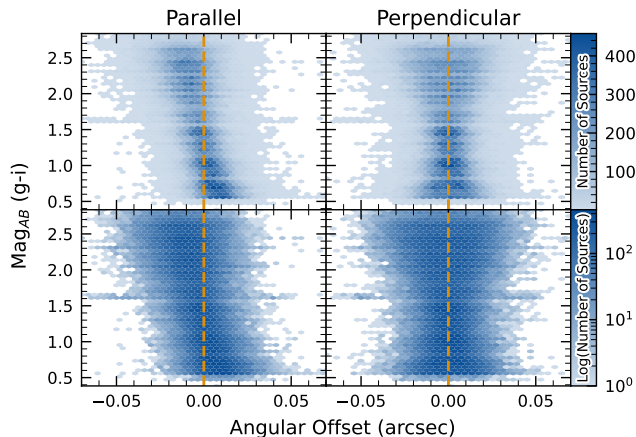


**Figure 26.** Visualization of [Differential Chromatic Refraction](#) (DCR) observed in the [LSSTComCam](#) commissioning campaign. The  $g - i$  color is computed for every source in the reference catalog (§3.3.3) that is matched to a direct source in the science image, and the binned density for the full survey is plotted against the angular offset between the reference and detected positions. The angular offset is projected along coordinates parallel and perpendicular to the parallactic angle of the observation, and shows a characteristic correlation along the parallel axis with no correlation along the perpendicular axis. The orange vertical dashed line indicates the expected  $g - i$  magnitude distribution at zero angular offset.

2294 another, which has not been accounted for. For injected  
 2295 source matching, the reference catalog (§3.3.3) does not  
 2296 include real on-sky objects. Based on prior analyses of  
 2297 the [DC2](#) simulations, purity is generally greater than  
 2298 completeness at any given magnitude. Similarly, for  
 2299 bright ( $i < 23$ ) objects classified as stars by reference  
 2300 band extendedness,  $< 5\%$  are either unmatched to a Eu-  
 2301 clid or HST object, or misclassified - that is, selecting on  
 2302 extendedness alone yields a fairly pure but incomplete  
 2303 sample of stars. We expect to remedy some of these  
 2304 shortcomings in future releases.

### 2305 5.7. Model Flux and Shape Measurement

2306 [Figure 30](#) shows  $i$ -band magnitude residuals for  
 2307 CModel and Sérsic measurements using the matched in-  
 2308 jected galaxies described in §5.6. Similar behavior is  
 2309 seen in other bands. Sérsic fluxes show reduced scatter  
 2310 for galaxies with  $i < 22.5$ , though CModel fluxes are  
 2311 less biased, with median residuals closer to zero and less  
 2312 magnitude-dependent. For fainter objects, Sérsic fluxes  
 2313 are more biased and less accurate. The magnitude of  
 2314 this bias is considerably larger than previously seen in  
 2315 simulated data. Subsequent testing indicates that this  
 2316 bias can be (roughly) halved by fitting an exponential  
 2317 model first, and then using those parameters to initialize

2318 a free Sérsic fit. This approach will be adopted in future  
 2319 releases. Aperture fluxes - including Kron and [GAaP](#) -  
 2320 are not shown as they are not corrected to yield total  
 2321 fluxes. The correction for Kron fluxes can be derived  
 2322 from the Sérsic index ([A. W. Graham & S. P. Driver](#)  
 2323 [2005](#)), but this correction is not provided in object ta-  
 2324 bles.

2325 [Figure 31](#) shows  $g - i$  color residuals versus  $r$ -band  
 2326 magnitude for the same sample of galaxies as [Figure 30](#).  
 2327 For this and most other colors, [GAaP](#) (with a  $1''$  aper-  
 2328 ture) and Sérsic colors both yield lower scatter; however,  
 2329 the CModel colors have the smallest bias. Curiously,  
 2330 the [GAaP](#) bias appears to be magnitude-dependent,  
 2331 whereas the Sérsic bias remains stable from  $19 < r < 26$ .  
 2332 Any of these color measurements are suitable for use  
 2333 for deriving quantities like photometric redshifts, stellar  
 2334 population parameters, etc.

2335 In addition to photometry, some algorithms include  
 2336 measurements of structural parameters like size, ellip-  
 2337 ticity, and Sérsic index. One particular known issue is  
 2338 that many (truly) faint objects have significantly overes-  
 2339 timated sizes and fluxes. This was also seen in the Dark  
 2340 Energy Survey ([K. Bechtol et al. 2025](#)), who dubbed  
 2341 such objects “super-spreaders”. These super-spreaders  
 2342 contribute significantly to overestimated fluxes at the  
 2343 faint end (see e.g. [Figure 30](#)), and are particularly prob-  
 2344 lematic for the Kron algorithm ([R. G. Kron 1980](#)), which  
 2345 should only be used with caution.

2346 As mentioned in §4.5, the Sérsic fits include a free  
 2347 centroid, which is initialized from the fiducial centroid  
 2348 of the object. Preliminary analyses of matched injected  
 2349 objects suggest that the Sérsic model galaxy [astrom-](#)  
 2350 [etry](#) residuals are somewhat smaller than for the stan-  
 2351 dard centroids used in other measurements, and so users  
 2352 of the Sérsic photometry should also use these centroid  
 2353 values. One caveat is that for faint objects and/or in  
 2354 crowded regions with unreliable deblending, free cen-  
 2355 troids can drift significantly and potentially towards  
 2356 other objects, so objects with large differences between  
 2357 the fiducial and Sérsic [astrometry](#) should be discarded  
 2358 or used with caution.

2359 Sérsic model parameter uncertainties are estimated  
 2360 by computing and inverting the Hessian matrix with  
 2361 the best-fit parameter values, after replacing the pixel  
 2362 data (but not uncertainties) by the best-fit model values.  
 2363 Currently, only the on-diagonal dispersion term (square  
 2364 root of the variance) is provided as an error estimate for  
 2365 each parameter. Future releases may provide more off-  
 2366 diagonal terms of the covariance matrix - particularly  
 2367 for the structural parameters, which are known to be  
 2368 correlated.

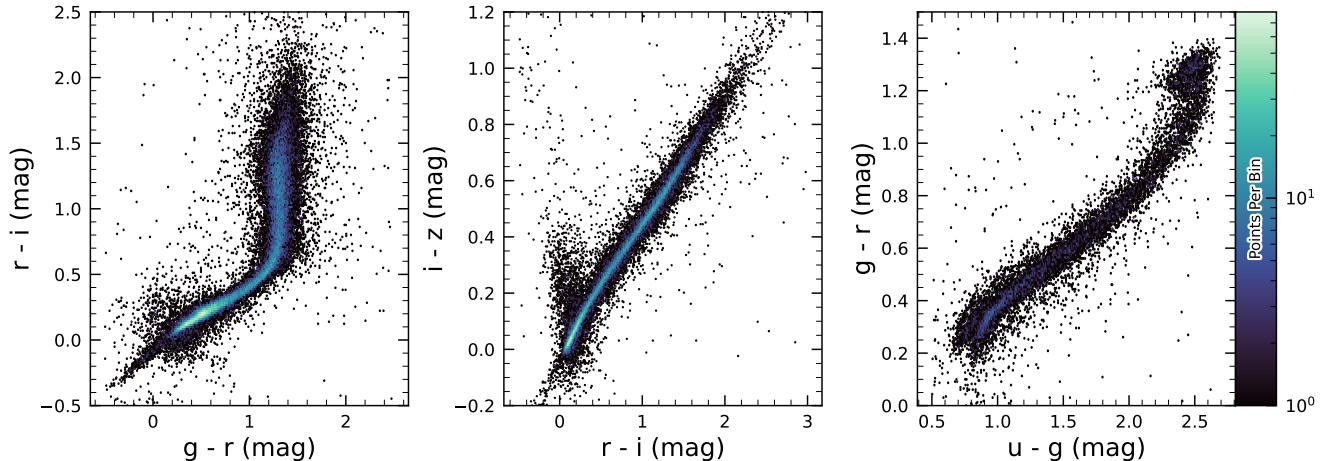


**Figure 27.** Examples of stellar loci for unresolved sources from the DP1 dataset. From left to right: *gri* stellar locus containing 63,236 stars with signal-to-noise ratio  $> 200$  in the *i* band; *riz* stellar locus containing 46,760 stars with signal-to-noise ratio  $> 200$  in the *i* band; *ugr* stellar locus containing 12,779 stars with signal-to-noise ratio  $> 50$  in the *u* band.

A major outstanding issue is that many parameter uncertainties - including but not limited to those for fluxes - are underestimated. This is at least partly (but not wholly) due to the fact that coaddition introduces covariance between pixels, which is not captured in per-pixel variances.

The degree to which uncertainties are underestimated can depend on the parameter in question and on the brightness of the object. In plots of uncertainty-scaled residuals, the ideal behavior is for the median (i.e. the bias) to lie close to zero, and for the  $\pm 1\sigma$  lines to lie at  $\pm 1$ , without any dependence on magnitude. Figure 32 shows that flux and color uncertainties for PSF model magnitudes of injected stars are both underestimated, but by a factor of approximately 1.7–2 that is not very sensitive to SNR. This holds for astrometric/centroid parameters as well.

In turn, Figure 33 shows that CModel color uncertainties of galaxies are underestimated by a similar factor at the faint end, but with appreciable scaling with magnitude (and thereby SNR). Flux error underestimation is both larger than for colors and scales more strongly with SNR. This indicates that systematic effects dominate the errors in fluxes, particularly for bright galaxies. This is also at least partly but not wholly due to so-called model inadequacy - that is, the fact that galaxy models, parameteric or otherwise, are insufficiently complex to capture the structure of real galaxies.

Figure 34 shows that Sérsic model fluxes and colors have similar behavior as CModel, but with a greater degree of overestimation. This may be partly due to the fact that Sérsic parameter uncertainties are estimated along with the free centroid and structural (shape and

Sérsic index) parameters, whereas the forced CModel fluxes and errors are derived from linear flux fits with a fixed shape and centroid.

Efforts are underway to investigate and quantify the origin of uncertainty underestimates and future releases will, at the least, provide recommendations for mitigations.

## 5.8. Difference Imaging

We assessed the performance of image differencing using both human vetting (§5.8.1) and source injection (§5.8.2).

### 5.8.1. Difference Imaging Purity

Members of the DP1 team labeled more than 11,000 DIASource image triplets, each consisting of cutouts from the science, template, and difference images. An internal labeling service (*tasso*) was deployed within the USDF environment. A random subset of approximately 16,000 DIASources was selected and uploaded to the service, which remained active for roughly three months and labeled by members of the DP1 team. Users labeled DIASource PNG image triplets, each consisting of cutouts from the science, template, and difference images. Each stamp had dimensions of  $51 \times 51$  pixels, matching the input size required by the machine-learning model. Access to the labeling service was granted to all individuals with commissioning data access. Each DIASource was classified exactly once, with a total of 35 volunteers contributing labels. Figure 35 show an example of one of the image triplets consisting of cutouts from the science, template, and difference images that volunteers were asked to label.

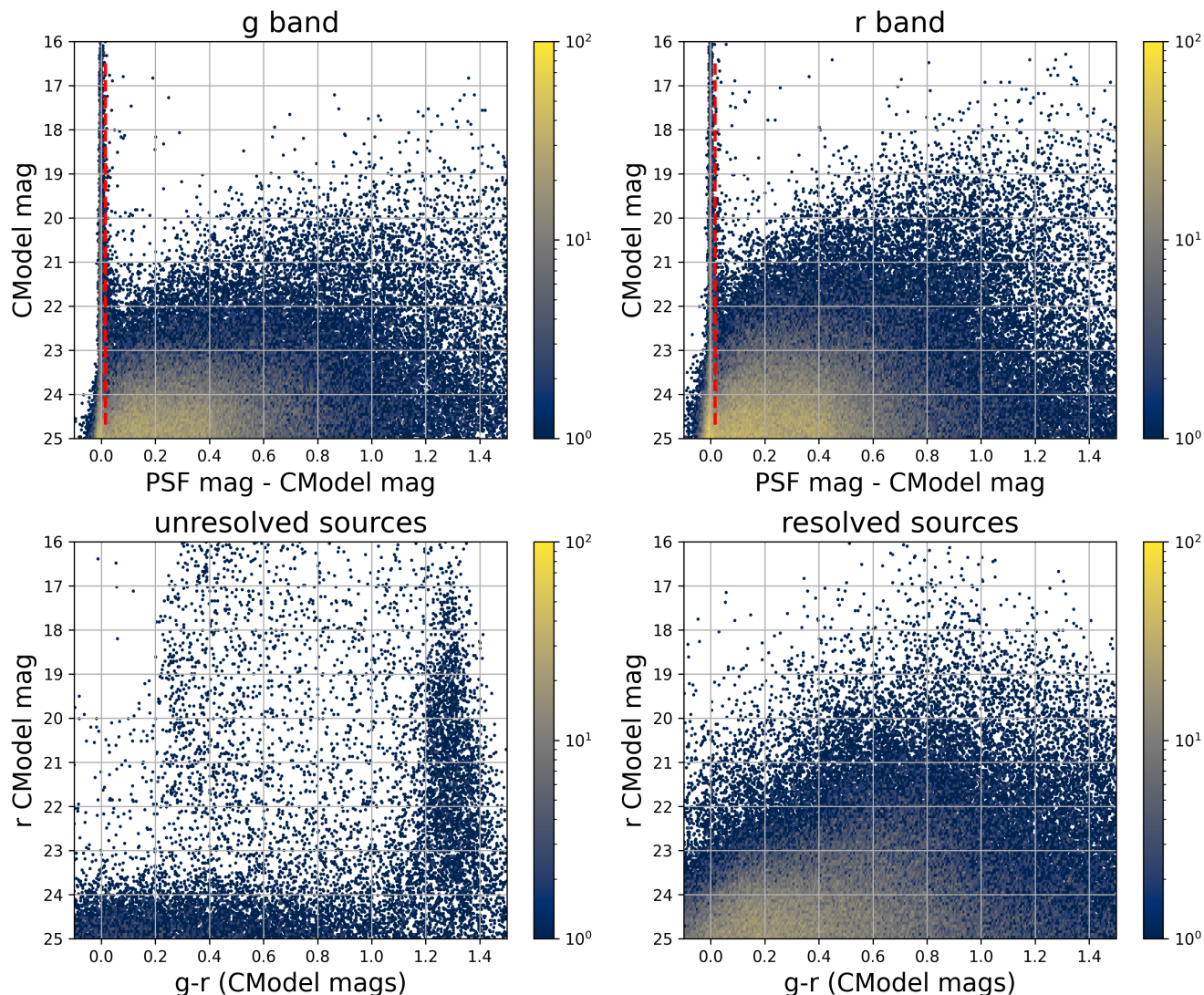


**Figure 28.** The top two panels show the difference between the PSF and CModel magnitudes as a function of CModel magnitude in the  $g$  and  $r$  bands for 178,547 sources with  $CModel_r < 25$  from the ECDFS field. The vertical dashed line in each panel marks the minimum value (0.016 mag) for setting the extendedness parameter to 1. The bottom two panels show the  $r$  vs.  $g - r$  color-magnitude diagrams for 14,701 unresolved (left) and 163,666 resolved (right) sources. Note the unresolved sample suffers from increasing contamination by galaxies for  $r > 24$ .

2434 The labeled sources were classified into multiple categories representing real astrophysical events and artifacts. Prior to any filtering, the raw artifact-to-real ratio was approximately 9:1. Bright stars were identified as the dominant source of artifacts, while correlated noise, particularly in the  $u$  and  $g$  bands, also produced spurious detections near the flux threshold. We expect to be able to mitigate these effects in future LSSTCam data.

2442 Applying a reliability threshold based on the Machine Learning reliability model described in §4.6.1 improved the purity of transient detections but had limited impact on variable stars. This limitation arises from technical constraints at the time of model training, which

2447 prevented the injection of variable stars into the synthetic training set. Future reliability models for LSST-Cam data, described in §4.6.1, will be trained using a broader and more representative range of input data.

2451 The performance of the reliability model on the test data (§4.6.1) is shown in Figure 36. The rate of true positives and false negatives obtained by thresholding the reliability score at 0.5 is reported for transients (99 stamps), and variable stars (316 stamps) vetted in `tasso` in Table 6.

2456 Additionally we crossmatched stamps with Solar System Objects with known orbits retrieving 5,988 Solar System Objects stamps.

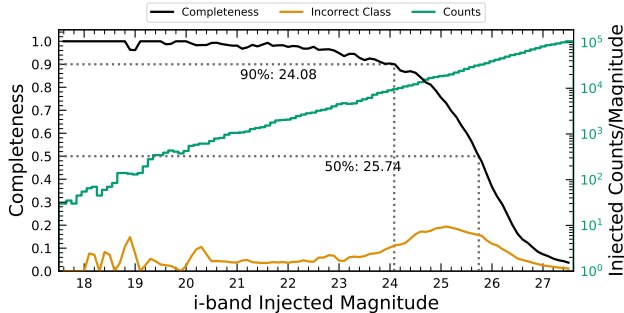


**Figure 29.** Completeness and incorrect classification fraction as a function of  $i$ -band CModel magnitude (Reference Magnitude) for DC2-based injected objects into a portion of the ECDFS field. The “Incorrect Class” line shows the proportion of objects that are matched but classified incorrectly by their reference-band extendedness, i.e. stars with extendedness of 1 or galaxies with extendedness of 0 in the reference band.

**Table 6.** The rate of true positives (TP) and false negatives (FN) obtained by thresholding the reliability score at 0.5 for Solar system objects, transients and variable stars.

Object Type	Number	TP Rate	FN Rate
Solar System	5,988	93.5%	6.5%
Transients	99	73.7%	26.3%
Variables	316	3.5%	96.5%

### 5.8.2. Difference Imaging Detection Completeness

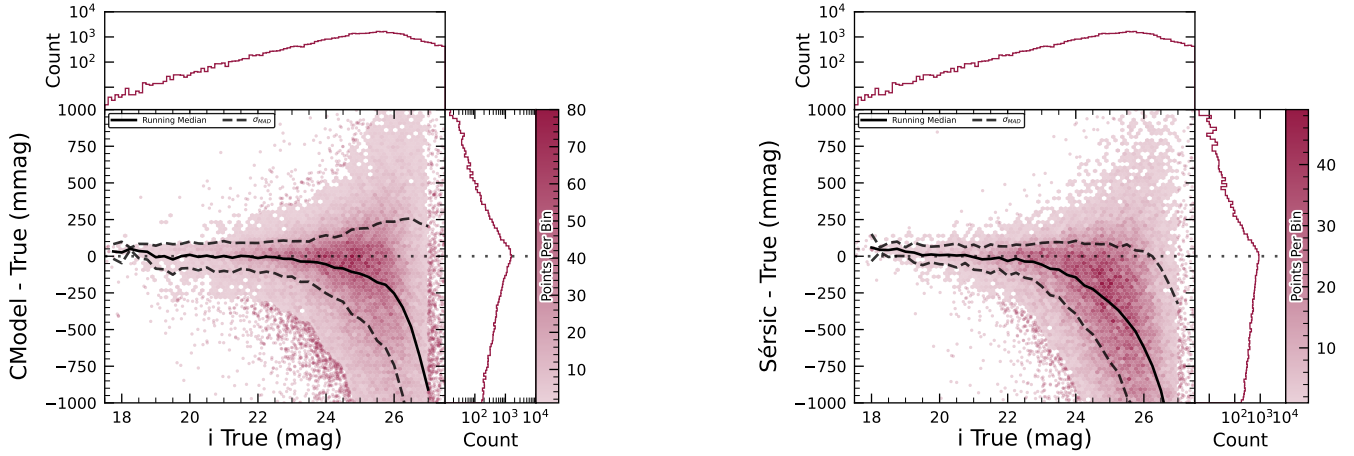
We assess the performance of our difference imaging pipeline using synthetic source injection on the science images prior to differencing. We construct a catalog of injected sources by joining two different samples of point sources, a set of hosted sources to emulate transients in galaxies and second set of hostless sources. The hosts are selected from the pipeline source catalog that is produced upstream by imposing a cut on their extendedness measurement and selecting  $N_{\text{src}} = \min(100, N \times 0.05)$  of the  $N$  available sources per detector. For each host we pick a random position angle and radius using its light profile shape to decide where to place the source, and also a random value of brightness for the injected source, with magnitudes higher than the host source.

The hostless sources instead have random positions in the CCD focal plane, and magnitudes chosen from a random uniform distribution with  $20 \geq m \geq m_{\text{lim}} + 1$ , where  $m_{\text{lim}}$  is the limiting magnitude of the image. We

used the LSST `source_injection` package<sup>104</sup> to include these sources in our test images. We performed a coordinate cross-match task, with a threshold of  $0''.5$  to find which of these sources were detected and which were lost, enabling the calculation of a set of performance metrics.

In Figure 37 we show the detection completeness as a function of the SNR, for sources in the ECDFS field, for filters *griz*. We observe a completeness  $> 95\%$  for sources with  $\text{SNR} > 6$ , with mean completeness  $\simeq 99\%$  and standard deviation of  $\simeq 0.7\%$ . In Figure 38 we show the distribution of the residuals of the recovered sky coordinates for the detected synthetic sources. The marginal distributions are both centered at zero, and for sources of  $\text{SNR} > 20$  the residuals are compatible with normal distributions  $\mathcal{N}(\mu = 0, \sigma^2 = (0''.02)^2)$ . In Figure 39 we show photometry results for our detected synthetic sources in the  $i$  filter, using PSF photometry on the difference images. We include both the magnitude residuals as well as the flux pulls, defined as  $(f_{\text{PSF}} - f_{\text{True}})/\sigma_{f_{\text{PSF}}}$ , where  $f_{\text{True}}$  is the true flux,  $f_{\text{PSF}}$  is the PSF flux and  $\sigma_{f_{\text{PSF}}}$  is its uncertainty, as a function of the true magnitude of the synthetic sources, including the running median and median absolute deviation (MAD) for the whole brightness range. We also include the true magnitude distribution as well as the detection completeness on the top panel, and for reference the 90% and 50% completeness magnitude values in vertical lines. On the right panels we include the marginal distribution for sources brighter than 22.5 mag, splitting the data into hosted and hostless, as well as the robust mean and standard deviation. From this figure we can see that our flux measurements are accurate within a wide range of magnitudes, for both hosted and hostless synthetic sources. We find that the median offset is below 0.002 mag for true magnitudes below 21, and with a maximum  $\sigma_{\text{MAD}}$  scatter of about 0.02 mag in this range. For true  $m_i < 22.5$ , the robust running median PSF magnitudes residuals are  $< 0.02$  mag, and when splitting into hosted and hostless both robust median are well below 0.01, and robust  $\sigma$ , i.e.  $\sigma_{\text{MAD}}$  are also well below 0.05. For all sources with  $m_i < 21.5$  the running median is always  $|\langle \delta \rangle| < 0.1$ , and MAD  $\sigma_\delta < 1$ . Extending to sources with  $m_i < 22.5$  then hostless sources have a robust mean pull below 0.02, with a robust standard deviation  $< 1.15$ , while these parameters increase to 0.2 and 1.2 for hosted sources, suggesting that we might

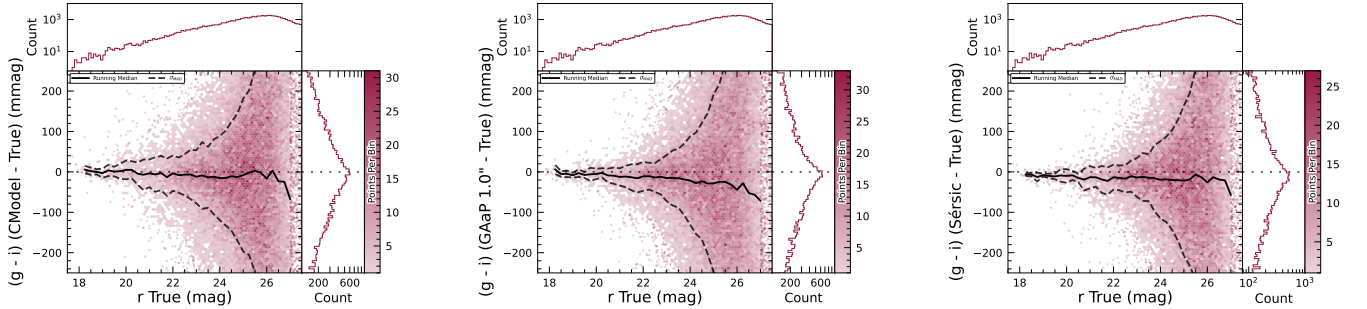
<sup>104</sup> <https://pipelines.lsst.io/modules/lstt.source.injection/index.html>



(a)  $i$ -band magnitude residuals for CModel measurements of injected galaxies.

(b)  $i$ -band magnitude residuals for Sérsic model measurements of injected galaxies.

**Figure 30.**  $i$ -band magnitude residuals for matched injected DC2 galaxies with the CModel and Sérsic algorithms in a portion of the ECDFS region, including the median and scatter thereof. The black line is the median.



(a)  $g-i$  color residuals for CModel measurements of injected galaxies.

(b)  $g-i$  color residuals for GAaP measurements of injected galaxies.

(c)  $g-i$  color residuals for Sérsic model measurements of injected galaxies.

**Figure 31.**  $g-i$  color residuals versus true  $r$ -band magnitude for matched injected DC2 galaxies with the CModel, GAaP and Sérsic algorithms in a portion of the ECDFS region.

2529 have contamination from host background sources po- 2547  
 2530 tentially biasing our fluxes. 2548

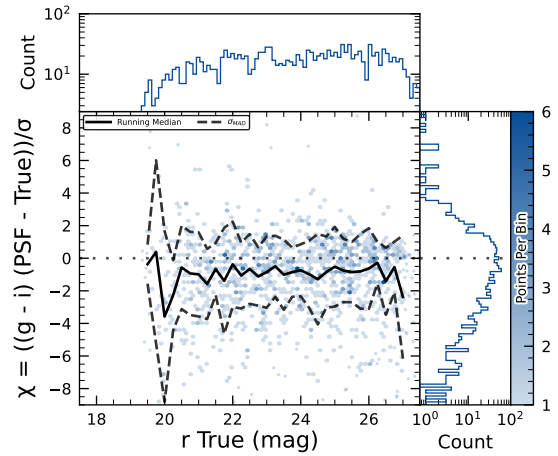
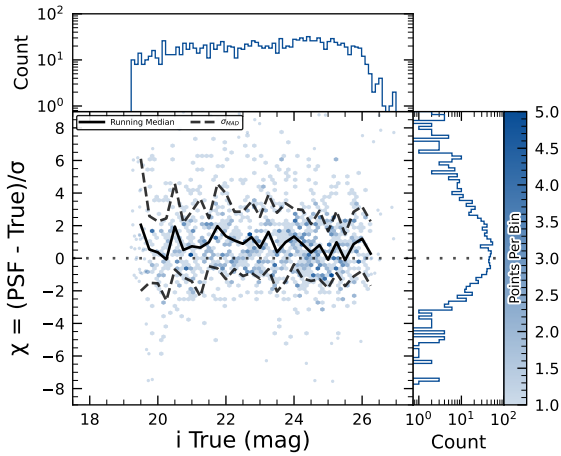
## 5.9. Solar System

### 5.9.1. Asteroid Linking Performance

2534 The evaluation of asteroid linking performance in DP1  
 2535 focused on demonstrating discovery capability. The solar  
 2536 system discovery pipeline produced 269,581 track-  
 2537 lets, 5,691 linkages, and 281 post-processed candidates.

2538 As described in §4.6.3, post-processing of the heli-  
 2539 olinc output with link\_purify produced a final set of  
 2540 281 candidate linkages, ranked with the most promising  
 2541 first. We then used find\_orb (B. Gray 2025) to derive  
 2542 orbit fits for each candidate, sorting the resulting list by  
 2543  $\chi^2_{\text{dof}}$ , a measure of fit quality. A conservative manual  
 2544 investigation of these candidates yielded a curated  
 2545 list of 93 probable new asteroid discoveries. Manual  
 2546 inspection of the linkages indicated that those ranked

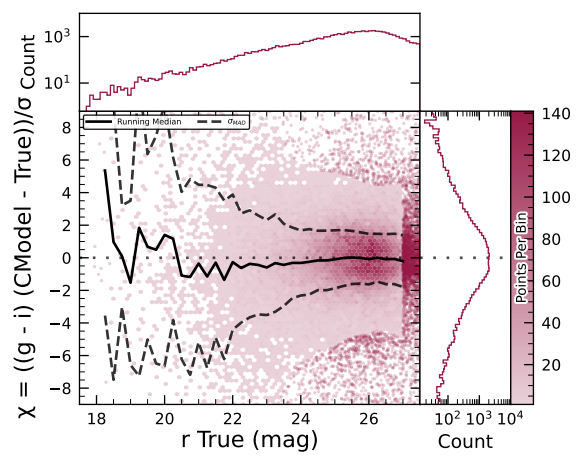
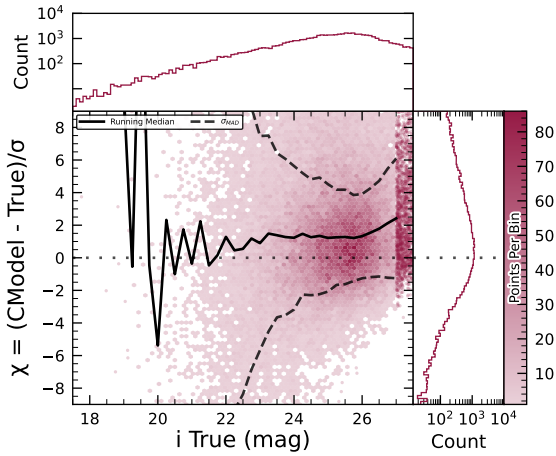
2549 0–137 corresponded to unique real asteroids; ranks 138–  
 2550 200 contained additional real objects intermixed with  
 2551 some spurious linkages; and ranks higher than 200 were  
 2552 essentially all spurious. This analysis indicates that it  
 2553 will be possible to identify cuts on quality metrics such  
 2554 as  $\chi^2$  to define discovery candidate samples with high  
 2555 purity; determining the exact quantitative cut values re-  
 2556 quires more data with LSSTCam. We next removed all  
 2557 observations matched to known asteroids (using Minor  
 2558 Planet Center (MPC)'s MPCChecker service), reducing  
 2559 the number of candidates to 97. Of these, four had  
 2560 strong astrometric and/or photometric outliers, likely  
 2561 due to self-subtraction in difference images due to the  
 2562 unavoidable limitations of template generation from the  
 2563 limited quantity of data available from LSSTComCam.  
 2564 We suspect these four linkages do correspond to real ob-  
 2565 jects, but have chosen to discard them out of an abun-  
 2566 dance of caution. The remaining 93 were submitted to



(a) *i*-band flux uncertainty-scaled residuals for PSF model measurements of injected stars.

(b) *g* - *i* color uncertainty-scaled residuals for PSF model measurements of injected stars.

**Figure 32.** Color and flux uncertainty-scaled residuals for matched injected DC2 stars' PSF model measurements in a portion of the ECDFS region.



(a) *i*-band flux uncertainty-scaled residuals for CModel measurements of injected galaxies.

(b) *g* - *i* color uncertainty-scaled residuals for CModel measurements of injected galaxies.

**Figure 33.** Color and flux uncertainty-scaled residuals for matched injected DC2 galaxies' CModel measurements in a portion of the ECDFS region.

2565 the Minor Planet Center and accepted as discoveries,  
 2566 demonstrating the LSST pipelines are able to success-  
 2567 fully discover new solar system objects.

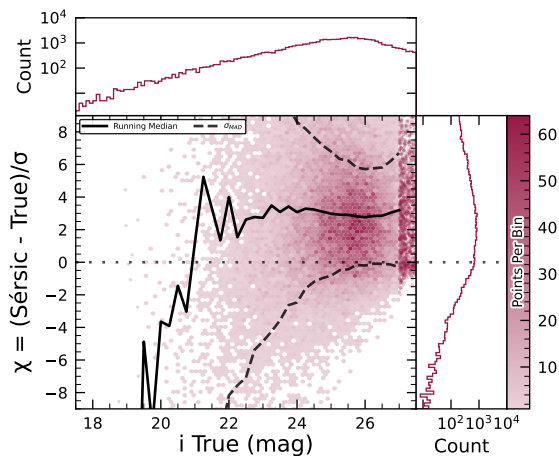
2568 **5.9.2. Asteroid Association Performance**

2569 During the Solar System association step, 5988 Di-  
 2570 aSources were linked to 431 unique Solar System ob-  
 2571 jects, These include 3,934 DiaSources with 338 previ-  
 2572 ously known objects cataloged by the MPC, and 2,054  
 2573 DiaSources with the 93 newly-discovered objects, all of  
 2574 which are main belt asteroids. An additional 143 de-  
 2575 tectations of these newly discovered objects were also re-  
 2576 covered. These detections were not initially identified  
 2577 by the discovery pipelines, as they did not meet the

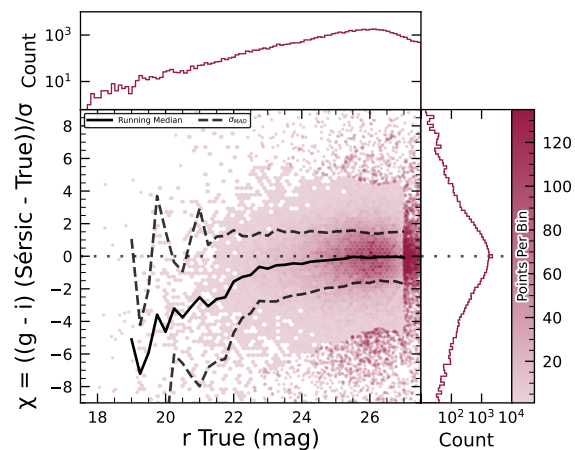
2578 required criteria for tracklet formation, specifically the  
 2579 minimum number of detections and/or the maximum  
 2580 allowed time span between observations.

2581 The astrometric residuals of known asteroid associa-  
 2582 tions are shown in Figure 40. The astrometric precision  
 2583 for solar system sources is excellent, with the majority of  
 2584 objects detected within 0".1 of their expected positions.

2585 By analyzing the signed median residuals to search for  
 2586 biases, we find that previously-known objects have mean  
 2587 residuals of 0".001 and -0".016 in the RA and Dec di-  
 2588 rections respectively, whereas newly-discovered objects  
 2589 have mean residuals of -0".035 and -0".010 in the RA  
 2590 and Dec directions, respectively. These mean residuals  
 2591 are small enough to eliminate the possibility of a tim-



(a)  $i$ -band flux uncertainty-scaled residuals for Sérsic model measurements of injected galaxies.



(b)  $g-i$  color uncertainty-scaled residuals for Sérsic model measurements of injected galaxies.

**Figure 34.** Color and flux uncertainty-scaled residuals for matched injected DC2 galaxies’ Sérsic measurements in a portion of the ECDFS region.

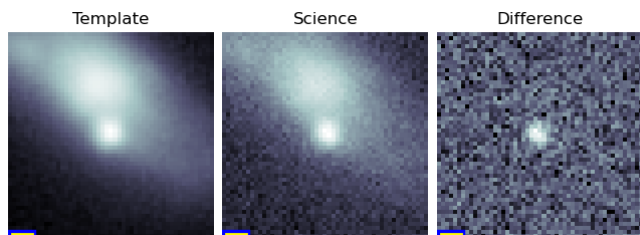


**Figure 35.** An example an image triplet consisting of cutouts showing, from left to right, the template, science, and difference images that volunteers were asked to label.

2592 ing offset greater than the second-scale shutter motion,  
 2593 which is consistent with the timing studies presented in  
 2594 §2.2.2.

2595 The wider scatter in the RA residuals is due to ob-  
 2596 jects whose measured orbital elements are less well con-  
 2597 strained, translating to larger along-track positional er-  
 2598 rors in the predicted positions. Observations of objects  
 2599 with large residuals are the most valuable ones from the  
 2600 point of view of improving the orbit, which is why we  
 2601 kept a generous matching radius. However, in future re-  
 2602 leases we are likely to couple this with either orbit fit-  
 2603 ting to verify the “singleton” match, or require two near-in-  
 2604 time observations (a tracklet) that match the expected  
 2605 motion vector as well.

2606 Optimal moving source attribution is an area of ac-  
 2607 tive work that we expect to fully converge in time of  
 2608 Data Release 1 (DR1). In the meantime, for DP1 we’ve  
 2609 opted to start with simple, more easily understandable,  
 2610 criteria.

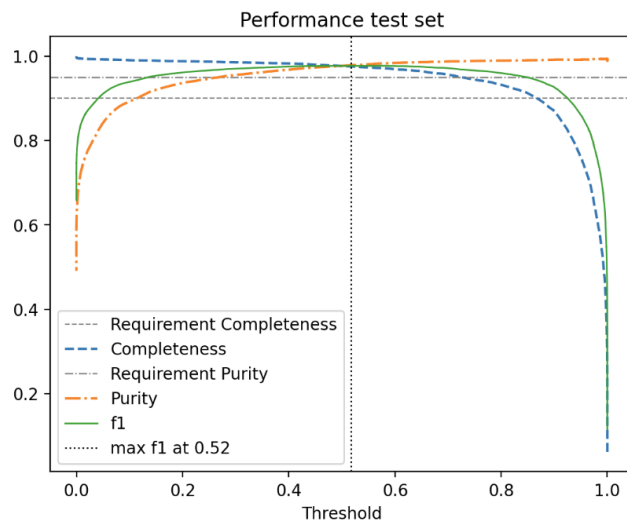


**Figure 36.** The purity and completeness of the reliability score is shown as a function of reliability threshold based on the testing data. A vertical line marks the threshold where the highest F1-score is obtained. The F1 score is the harmonic mean of completeness and purity. See §4.6.1 for details on the model and model training.

## 5.10. Crowded Fields

2611 Among the seven Rubin DP1 target fields, two stand  
 2612 out for their severe stellar crowding: the globular cluster  
 2613 47 Tucanae (47\_Tuc) and the Fornax dwarf spheroidal  
 2614 galaxy (Fornax dSph). These fields were selected in part  
 2615 to stress-test the LSST Science Pipelines under high-  
 2616 density conditions. While both exhibit high stellar den-  
 2617 sities, the nature and spatial extent of the crowding dif-  
 2618 fer significantly.  
 2619

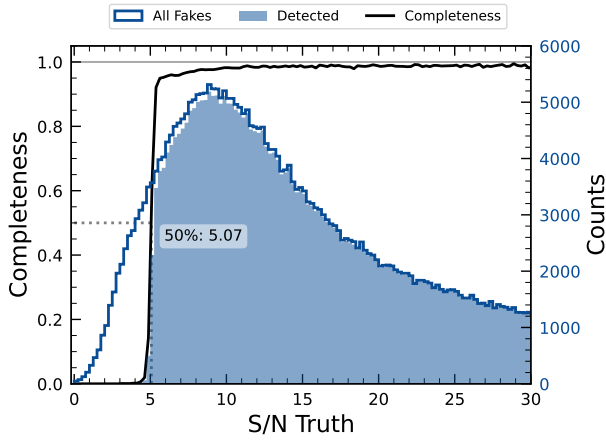


**Figure 37.** The difference image detection completeness for injected sources in the ECDFS field, for filters *griz*, as a function of the estimated signal to noise ratio SNR. This completeness is the ratio between the found fake sources (shaded histogram) and all the sources (solid line). The horizontal dashed line represents where the 50% completeness level is reached, at approximately  $\text{SNR} \simeq 5.07$ .

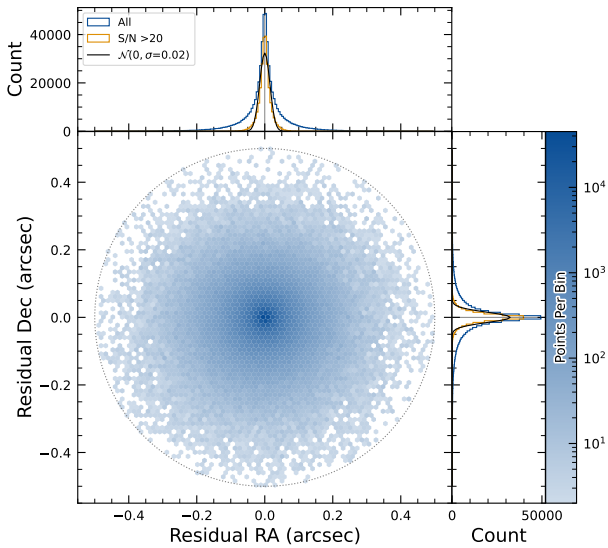


**Figure 38.** Coordinate residuals for detected synthetic sources in difference images, between recovered and true position of the sources in the ECDFS field. In the top and right panels we include the distribution of these offsets, for all sources as well as for sources with  $\text{SNR} > 20$ . These high SNR sources show gaussian coordinate residual distributions with  $\sigma = 0''.02$  (black solid lines). The circle reflects the matching radius of  $0''.5$ .

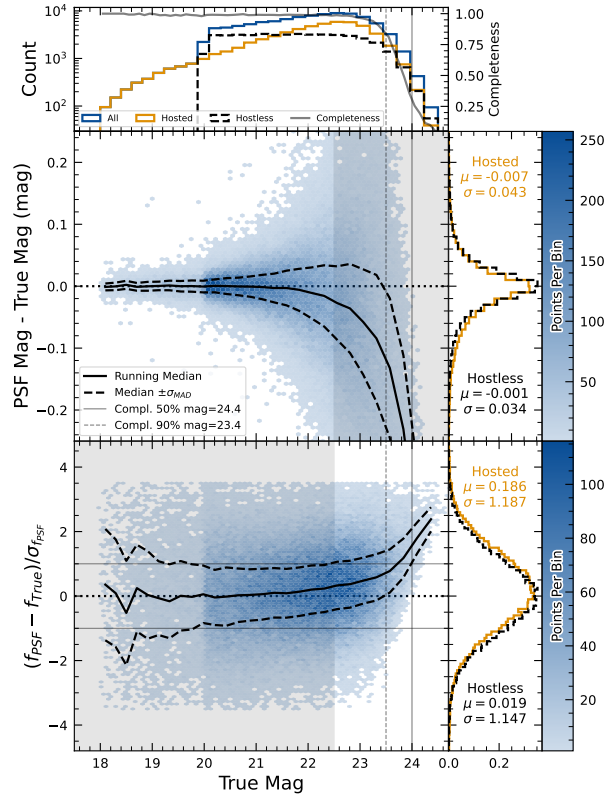


**Figure 39.** Magnitude residuals and flux pulls for *i*-band PSF photometry on difference images for ECDFS field in *i* for detected injected sources. Top panel: Distribution of true magnitudes for injected sources (blue), and split into hostless (black dash) and hosted (orange) sources, with detection completeness as a function of true magnitude (gray line). Vertical dashed lines indicate the 90% and 50% completeness magnitude limits. Center left panel: 2D hexbin plot of PSF magnitude residuals (measured minus true) versus true magnitude for detected sources, with running median (solid black) and  $\sigma_{MAD}$  (dashed black) overlaid. Center right panel: Marginalized distributions of PSF magnitude residuals for hostless (blue) and hosted (orange) sources with true magnitude  $m_i < 22.5$ , annotated with robust mean and standard deviation. Bottom left panel: 2D hexbin plot of PSF flux pulls versus true magnitude for detected sources, with running median (solid black) and  $\sigma_{MAD}$  (dashed black) overlaid. Bottom right panel: Marginalized distributions of PSF flux pulls for hostless (blue) and hosted (orange) sources with true magnitude  $m_i < 22.5$ , annotated with robust mean and standard deviation.

2620 47 Tuc presents extreme crowding across much of the  
 2621 field, encompassing its dense core and the eastern re-

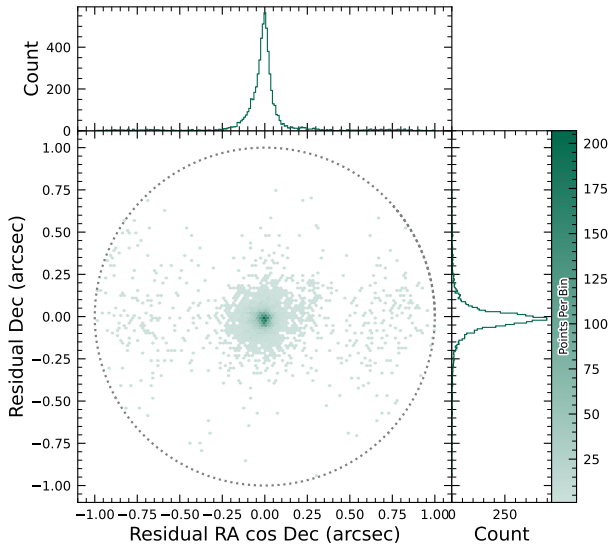


**Figure 40.** Astrometric residuals between expected and observed positions of Solar System Objects in DP1. The median residuals are  $0''.001$  and  $-0''.016$  in R.A./Dec direction, with standard deviations of  $0''.19$  and  $0''.10$ , respectively. No detectable systematic offset from zero indicates there are no major errors in either timing or astrometry delivered by the Rubin system. The wider scatter in the RA direction is due to objects whose measured orbital elements are less well constrained, translating to larger along-track positional errors in the predicted positions.

gions influenced by the Small Magellanic Cloud (SMC). This pervasive crowding leads to persistent challenges for deblending and reliable source detection, exposing field-wide limitations in the current pipeline performance (Y. Choi et al. 2025). In contrast, Fornax dSph shows significant crowding only in its central region, with outer areas remaining well resolved and easier to process.

In both 47 Tuc and Fornax, extreme crowding led to the deblending step being skipped frequently when memory or runtime limits were exceeded, typically due to an excessive number of peaks, or large parent footprints. However, the impact of these limitations differed: in 47 Tuc, deblending was often skipped across the entire field, resulting in large gaps and substantially reduced completeness. In Fornax, these issues were largely confined to the central region, with much better recovery in the outskirts. This contrast highlights how the pipeline’s limitations depend on the spatial extent of high-density regions: 47 Tuc exposed systematic, field-wide challenges, whereas Fornax revealed more localized, density-driven limits.

T. M. Wainer et al. (2025) explored the Rubin DP1 DiaObject catalog (§3.2) in the 47 Tuc field, which contains sources detected in difference images. Because forced photometry is performed at these positions across all single-epoch images, this dataset bypasses the coadd-based detection and deblending stages that often fail in crowded regions. By computing the median of the forced photometry for each DiaObject across available visits, they recovered approximately three times more candidate cluster members than found in the standard Object table (Y. Choi et al. 2025). This result underscores the value of difference-imaging-based catalogs for probing dense stellar regions inaccessible to standard coadd processing in DP1.

Although the DP1 pipeline was not optimized for crowded-field photometry, these early studies of 47 Tuc and Fornax provide critical benchmarks. They highlight both the limitations and opportunities for science with Rubin data in crowded environments, and they inform future pipeline development aimed at robust source recovery in complex stellar fields.

## 6. RUBIN SCIENCE PLATFORM

The RSP (M. Jurić et al. 2019) is a powerful, cloud-based environment for scientific research and analysis of petascale-scale astronomical survey data. It serves as the primary interface for scientists to access, visualize, and conduct next-to-the-data analysis of Rubin and LSST data. The RSP is designed around a “bring the compute to the data” principle, eliminating the need for users to download massive datasets. Although DP1 is much smaller in size (3.5 TB) than many current survey datasets, future LSST datasets will be far larger and more complex, making it crucial to co-locate data and analysis for effective scientific discovery.

The RSP provides users with access to data and services through three distinct user-facing Aspects: a *Portal*, which facilitates interactive exploration of the data; a JupyterLab-based *Notebook* environment for data analysis using Python; and an extensive set of *Application Programming Interfaces (APIs)* that enable programmatic access to both data and services. The three Aspects are designed to be fully integrated, enabling seamless workflows across the RSP. The data products described in §3 are accessible via all three Aspects, and the system facilitates operations such as starting a query in one Aspect and retrieving its results in another. Figure 41 shows the Rubin Science Platform landing page in the Google cloud.

The RSP is supported by a number of back-end services, including databases, files, and batch comput-

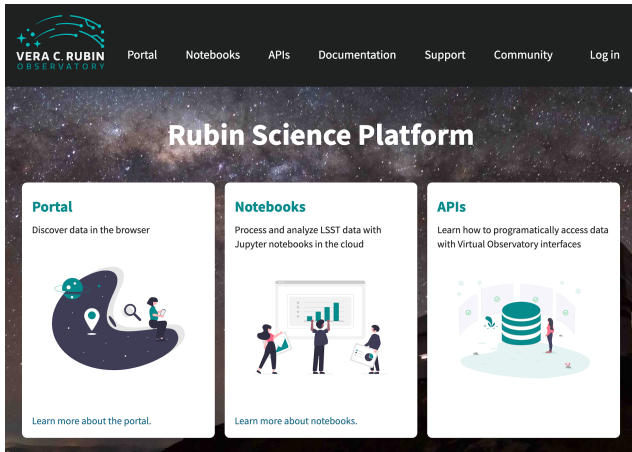


**Figure 41.** The Rubin Science Platform landing page at <https://data.lsst.cloud/> showing the three user-facing Aspects as well as links to documentation and support information.

ing. Support for collaborative work through shared workspaces is also included in the RSP.

A preview of the RSP was launched on Google Cloud in 2022, operating under a shared-risk model to support Data Preview 0 (W. O’Mullane et al. 2024a). This allowed the community to test the platform, begin preparations for science, and provide valuable feedback to inform ongoing development. It was the first time an astronomical research environment was hosted in a cloud environment. The DP1 release brings major updates to RSP services, enhancing scientific analysis capabilities. The RSP remains under active development, with incremental improvements being rolled out as they mature. During the Rubin Early Science Phase, the RSP will continue to operate under a shared-risk model. This section outlines the RSP functionality available at the time of the DP1 release and provides an overview of planned future capabilities.

### 6.1. Rubin Data Access Center

The Rubin US Data Access Center (US DAC) utilizes a novel hybrid on-premises-cloud architecture, which combines on-premises infrastructure at the USDF at SLAC with flexible and scalable resources in the Google cloud. This architecture has been deployed and tested using the larger simulated data set of DP0.2 (W. O’Mullane et al. 2024b).

In this hybrid model, user-facing services are deployed in the cloud to support dynamic scaling in response to user demand and to simplify the provisioning and management of large numbers of science user accounts. The majority of the static data products described in §3 are stored on-premises at the USDF to benefit from cost-effective mass storage and close integration with Ru-

bin data processing infrastructure, also located at the USDF. For imaging data, the Data Butler (§6.2.2) provides the interface between the cloud-based users and data services, and the on-premises data. For catalog data, a cloud-based TAP client (§6.2.1) submits queries to the on-premises Qserv database cluster (§6.5) and retrieves the results. In the initial DP1 deployment, catalog data is hosted at the USDF while image data is stored in the cloud. The full hybrid model will be rolled out and further tested following the release of DP1. The RSP features a single-sign-on authentication and authorization system to provide secure access for Rubin data rights holders (R. Blum & the Rubin Operations Team 2020).

### 6.2. API Aspect

The API Aspect provides a comprehensive set of user-facing interfaces for programmatic access to the DP1 data products, through both IVOA-compliant services and the Rubin Data Butler. IVOA services enable standard queries and integration with existing tools, while the Butler facilitates advanced data processing within the LSST Science Pipelines.

At the time of the DP1 release, some IVOA services are unavailable, and certain data products are only accessible via the Butler. This section provides an overview of the available IVOA services and Butler access.

#### 6.2.1. IVOA Services

Rubin has adopted a Virtual Observatory (VO)-first design philosophy, prioritizing compliance with IVOA standard interfaces to foster interoperability, standardization, and collaboration. In cases where standardized protocols have yet to be established, additional services have been introduced to complement these efforts. This approach ensures that the RSP can be seamlessly integrated with community-standard tools such as Tool for Operations on Catalogues And Tables (TOPCAT) (M. Taylor 2011) and Aladin (F. Bonnarel et al. 2000; T. Boch & P. Fernique 2014; M. Baumann et al. 2022), as well as libraries such as PyVO (M. Graham et al. 2014).

The user-facing APIs are also used internally within the RSP, creating a unified design that ensures consistent and reproducible workflows across all three Aspects. This reduces code duplication, simplifies maintenance, and ensures all users, both internal and external, access data in the same way. For example, an Astronomical Data Query Language (IVOA standard) (ADQL) query on the Object catalog via TAP yields identical results whether run from the Portal, Notebook, or an external client.

2778 The following [IVOA](#) services are available at the time  
2779 of the [DP1](#) release:

2780 • **Table Access Protocol (TAP) Service:** A  
2781 TAP service ([P. Dowler et al. 2019](#)) enables queries  
2782 of catalog data via the IVOA-standard [ADQL](#), a  
2783 dialect of [SQL92](#) with spherical geometry exten-  
2784 sions. The main [TAP](#) service for [DP1](#) runs on the  
2785 Rubin-developed [Qserv](#) database (§ 6.5), which  
2786 hosts the core science tables described in §3.2, as  
2787 well as the [Visit](#) database. It also provides image  
2788 metadata in the IVOA [ObsCore](#) format via the  
2789 standard `ivoa.ObsCore` table, making it an “Ob-  
2790 sTAP” service ([ObsTAP](#); [M. Louys et al. 2017](#)).  
2791 The TAP service is based on the [Canadian As-  
2792 tronomy Data Centre \(CADC\)](#)’s open-source Java  
2793 TAP implementation<sup>105</sup>, modified for the exact  
2794 query language accepted by [Qserv](#). It currently  
2795 supports a large subset of [ADQL](#), with limitations  
2796 documented in the data release materials (see §7.1)  
2797 and exposed via the TAP **capabilities** endpoint  
2798 where possible.

2799 The TAP service provides metadata annotations  
2800 consistent with the standard, including table and  
2801 column descriptions, indications of foreign-key re-  
2802 lationships between tables, and column metadata  
2803 such as units and [IVOA Unified Content Descrip-  
2804 tors \(UCDs\)](#).

2805 • **Image Access Services:** Rubin image access  
2806 services are compliant with [IVOA SIAv2](#) (Sim-  
2807 ple Image Access Protocol, version 2; [T. Jenness  
2808 et al. 2024](#); [P. Dowler et al. 2015](#)) for discovering  
2809 and accessing astronomical images based on [meta-  
2810 data](#). [SIAv2](#) is a [REpresentational State Transfer  
2811 \(REST\)](#)-based protocol designed for the discovery  
2812 and retrieval of image data. It allows, for instance,  
2813 querying all images in a given band over a defined  
2814 sky region and time period.

2815 Users identify an image or observation of interest  
2816 and query the service. The result set includes  
2817 [metadata](#) about the image, such as the sky posi-  
2818 tion, time, or band, and a data access URL, which  
2819 includes an IVOA Identifier uniquely identifying  
2820 the dataset ([T. Jenness & G. P. Dubois-Felsmann  
2821 2025](#)), allowing the dataset to be retrieved or a  
2822 cutout requested via [Server-side Operations for  
2823 Data Access \(IVOA standard\) \(SODA\)](#).

2824 • **Image Cutout Service:** The Rubin Cutout Ser-  
2825 vice ([R. Allbery 2023, 2024](#)) is based on the IVOA  
2826 [SODA](#) standard ([F. Bonnarel et al. 2017](#)). Users  
2827 submit requests specifying sky coordinates and the  
2828 cutout size as the radius from the coordinates, and  
2829 the service performs the operation on the full im-  
2830 age and returns a result set. For [DP1](#), the cutout  
2831 service is a single cutout service only where  $N$   
2832 cutout requests will require  $N$  independent syn-  
2833 chronous calls. We expect some form of bulk  
2834 cutout service by mid 2026.

2835 • **HiPS Data Service:** An authenticated [HiPS](#)  
2836 ([P. Fernique et al. 2017](#)) data service for seam-  
2837 less pan-and-zoom access to large-scale co-adds.  
2838 It supports fast interactive progressive image ex-  
2839 ploration at a range of resolutions.

2840 • **WebDAV:** A [Web Distributed Authoring and  
2841 Versioning \(WebDav\)](#) service is provided to enable  
2842 users to remotely manage, edit, and organize files  
2843 and directories on the [RSP](#) as if they were local  
2844 files on their own computer. This is especially use-  
2845 ful for local development.

#### 2846 6.2.2. *Data Butler*

2847 The Rubin Data Butler ([T. Jenness et al. 2022](#); [N. B.  
2848 Lust et al. 2023](#)), is a high-level interface designed to  
2849 facilitate seamless access to data for both users and  
2850 software systems. This includes managing storage for-  
2851 mats, physical locations, data staging, and database  
2852 mappings. A [Butler](#) repository contains two compo-  
2853 nents:

- 2854 • the *Data Store*: A physical storage system for  
2855 datasets, e.g., a [Portable Operating System Inter-  
2856 face \(POSIX\)](#) file system or [S3](#) object store; and
- 2857 • the *Registry*: An [Structured Query Language  
2858 \(SQL\)](#)-compatible database that stores metadata  
2859 about the datasets in the data store.

2860 For [DP1](#), the Butler repository is hosted in the Google  
2861 Cloud, using an ([Amazon](#)) [Simple Storage Service  
2862 \(S3\)](#)-compatible store for datasets and [AlloyDB](#), a  
2863 [PostgreSQL](#)-compatible database, for the registry.

2864 In the context of the [Butler](#), a *dataset* refers to a  
2865 unique data product, such as an image, catalog or map,  
2866 generated by the observatory or processing pipelines  
2867 Datasets belong to one of the various types of data  
2868 products, described in §3. The [Butler](#) ensures that  
2869 each dataset is uniquely identifiable by a combination  
2870 of three pieces of information: a data coordinate,  
2871 a dataset type, and a run collection. For example,

<sup>105</sup> <https://github.com/opencadc/tap>

**Table 7.** Tract coverage of each DP1 field. The size of a tract is larger than the LSSTComCam field of view; however, since each observed field extends across more than one tract, each field covers multiple tracts.

Field Code	Tract ID
47_Tuc	453, 454
ECDFS	4848, 4849, 5062, 5063, 5064
EDFS_comcam	2234, 2235, 2393, 2394
Fornax_dSph	4016, 4017, 4217, 4218
Rubin_SV_095_-25	5305, 5306, 5525, 5526
Rubin_SV_38_7	10221, 10222, 10463, 10464, 10704, 10705
Seagull	7610, 7611, 7849, 7850

a dataset that represents a single raw image in the *i* band taken on the night starting 2024-11-11 with exposure ID 2024111100074 would be represented as `dataId='exposure':2024111100074, 'band':'i', 'instrument':'LSSTComCam'` and is associated with the `raw` DatasetType. For a deep coadd on a patch of sky in the Seagull field, there would be no exposure dimensions and instead the tract, patch and band would be specified as `dataId='tract':7850, 'patch':6, 'band':'g', 'instrument':'LSSTComCam', skymap='lsst_cells_v1'` and is associated with the `deep_coadd` DatasetType. The tract identification numbers and corresponding target names for these tracts are listed in Table 7.

The data coordinate is used to locate a dataset in multi-dimensional space, where dimensions are defined in terms of scientifically meaningful concepts, such as instrument, visit, detector or band. For example, a calibrated single-visit image (§3.1) has dimensions including band, instrument, and detector. In contrast, the visit table (§3.2), a catalog of all calibrated single-epoch visits in DP1, has only the instrument dimension. The main dimensions used in DP1 are listed, together with a brief description, in Table 8. To determine which dimensions are relevant for a specific dataset, the Butler defines dataset types, which associate each dataset with its specific set of relevant dimensions, as well as the associated Python type representing the dataset. The dataset type defines the kind of data a dataset represents, such as a raw image (`raw`), a processed catalog (`object_forced_source`), or a sky map (`skyMap`). Table 9 lists all the dataset types available via the Butler in DP1, together with the dimensions needed to uniquely identify a specific dataset and the number of unique datasets of each type.

It is important to highlight a key difference between accessing catalog data via the TAP service versus the Butler. While the TAP service contains entire catalogs, many of the same catalogs in the Butler are split into multiple separate catalogs. This is partly due to how these catalogs are generated, but also because of the way data is stored within and retrieved from the Butler repository – it is inefficient to retrieve the entire Source catalog, for example, from the file system. Instead, because the Source catalog contains data for sources detected in the `visit_images`, there is one Source catalog in the Butler for each `visit_image`. Similarly, there is one Object catalog for each `deep_coadd`. All the catalogs described in §3.2, aside from the `CcdVisit`, `SSObject`, `SSSource`, and `Calibration` catalogs, are split within the Butler.

A dataset is associated with one or more *Collections*; logical groupings of datasets within the Butler system that were created or processed together by the same batch operation. Collections allow multiple datasets with the same data coordinate to coexist without conflict. Collections support flexible, parallel processing by enabling repeated analyses of the same input data using different configurations. The DP1 Butler is read-only; a writable Butler is expected by mid-2026.

### 6.2.3. Remote Programmatic Access

The Rubin RSP API can be accessed from a local system by data rights holders outside of the RSP, by creating a user security token. This token can then be used as a bearer token for API calls to the RSP TAP service. This capability is especially useful for remote data analysis using tools such as TOPCAT, as well as enabling third-party systems, e.g., Community Alert Brokers, to access Rubin data. Additionally, it supports remote development, allowing for more flexible workflows and integration with external systems.

### 6.3. Portal Aspect

The Portal Aspect provides an interactive web-based environment for exploratory data discovery, filtering, querying, and visualization of both image and catalog data, without requiring programming expertise. It enables users to access and analyze large datasets via tools for catalog queries, image browsing, time-series inspection, and cross-matching.

The Portal is built on Firefly (X. Wu et al. 2019), a web application framework developed by the Infrared Processing and Analysis Center (IPAC). Firefly provides interactive capabilities such as customizable table views, image overlays, multi-panel visualizations, and synchronized displays linking catalog and image data.

**Table 8.** Descriptions of and valid values for the key data dimensions in DP1. YYYYMMDD signifies date and # signifies a single 0–9 digit.

Dimension	Format/Valid values	Description
day_obs	YYYYMMDD	A day and night of observations that rolls over during daylight hours.
visit	YYYYMMDD#####	A sequence of observations processed together; synonymous with “exposure” in DP1.
exposure	YYYYMMDD#####	A single exposure of all nine ComCam detectors.
instrument	LSSTComCam	The instrument name.
detector	0–8	A ComCam detector.
skymap	lsst_cells_v1	A set of tracts and patches that subdivide the sky into rectangular regions with simple projections and intentional overlaps.
tract	See <a href="#">Table 7</a>	A large rectangular region of the sky.
patch	0–99	A rectangular region within a tract.
physical_filter	u_02, g_01, i_06, r_03, z_03, y_04	A physical filter.
band	u, g, r, i, z, y	An conceptual astronomical passband.

**Table 9.** The name and number of each type of data product in the Butler and the dimensions required to identify a specific dataset.

Data Product	Name in Butler	Required Dimensions	Number in DP1
<b>Image Data Products</b>			
raw	raw	instrument, detector, exposure	16125
visit_image	visit_image	instrument, detector, visit	15972
deep_coadd	deep_coadd	band, skymap, tract, patch	2644
template_coadd	template_coadd	band, skymap, tract, patch	2730
difference_image	difference_image	instrument, detector, visit	15972
<b>Catalog Data Products</b>			
Source	source	instrument, visit	1786
Object	object	skymap, tract	29
ForcedSource	object_forced_source	skymap, tract, patch	636
DiaSource	dia_source	skymap, tract	25
DiaObject	dia_object	skymap, tract	25
ForcedSourceOnDiaObject	dia_object_forced_source	skymap, tract, patch	597
SSSource	ss_source	–	1
SSObject	ss_object	–	1
Visit	visit_table	instrument	1
CcdVisit	visit_detector_table	instrument	1

2958 Designed to support both exploratory data access and  
2959 detailed scientific investigation, the Portal delivers an  
2960 intuitive user experience, allowing users to visually ana-  
2961 lyze data while retaining access to underlying metadata  
2962 and query controls.

#### 2963 6.4. Notebook Aspect

2964 The Notebook Aspect provides an interactive, web-  
2965 based environment built on Jupyter Notebooks, en-  
2966 abling users to write and execute Python code directly  
2967 on Rubin and LSST data without downloading it locally.  
2968 It offers programmatic access to Rubin and LSST data  
2969 products, allowing users to query and retrieve datasets,  
2970 manipulate and display images, compute derived prop-

2971 erities, plot results, and reprocess data using the LSST  
 2972 Science Pipelines (§4.1). The environment comes pre-  
 2973 installed with the pipelines and a broad set of widely  
 2974 used astronomical *software* tools, supporting immediate  
 2975 and flexible data analysis.

## 2976 6.5. Databases

2977 The user-facing Aspects of the RSP are supported by  
 2978 several backend databases that store catalog data prod-  
 2979 ucts, image metadata, and other derived datasets. The  
 2980 *schema* for DP1 and other Rubin databases are available  
 2981 online at <https://sdm-schemas.lsst.io>.

### 2982 6.5.1. Qserv

2983 The final 10-year LSST catalog is expected to reach  
 2984 15 PB and contain measurements for billions of stars  
 2985 and galaxies across trillions of detections. To support  
 2986 efficient storage, querying, and analysis of this dataset,  
 2987 Rubin Observatory developed Qserv (D. L. Wang et al.  
 2988 2011; F. Mueller et al. 2023) – a scalable, parallel, dis-  
 2989 tributed SQL database system. Qserv partitions data  
 2990 over approximately equal-area regions of the celestial  
 2991 sphere, replicates data to ensure resilience and high  
 2992 availability, and uses shared scanning to reduce overall  
 2993 I/O load. It also supports a package of scientific user-  
 2994 defined functions (SciSQL: [https://smonkewitz.github.  
 2995 io/scisql/](https://smonkewitz.github.io/scisql/)) simplifying complex queries involving spher-  
 2996 ical geometry, statistics, and photometry. Qserv is  
 2997 built on robust production-quality components, includ-  
 2998 ing MariaDB (<https://www.mariadb.org/>) and XRootD  
 2999 (<https://xrootd.org/>). Qserv runs at the USDF and user  
 3000 access to catalog data is via the TAP service (§6.2.1).  
 3001 This enables catalog-based analysis through both the  
 3002 RSP Portal and Notebook Aspects.

3003 Although the small DP1 dataset does not require  
 3004 Qserv’s full capabilities, we nevertheless chose to use  
 3005 it for DP1 to accurately reflect the future data access  
 3006 environment and to gain experience with scientifically-  
 3007 motivated queries ahead of full-scale deployment. Qserv  
 3008 is open-source and available on GitHub: [https://github.  
 3009 com/lsst/qserv](https://github.com/lsst/qserv).

## 3010 7. SUPPORT FOR COMMUNITY SCIENCE

3011 Rubin Observatory has a science community that en-  
 3012 compasses thousands of individuals worldwide, with a  
 3013 broad range of experience and expertise in astronomy  
 3014 in general, and in the analysis of optical imaging data  
 3015 specifically.

3016 Rubin’s model to support this diverse community to  
 3017 access and analyze DP1 emphasizes self-help via docu-  
 3018 mentation and tutorials, and employs an open platform  
 3019 for asynchronous issue reporting that enables crowd-

3020 sourced solutions. These two aspects of community sup-  
 3021 port are augmented by virtual engagement activities. In  
 3022 addition, Rubin supports its Users Committee to advo-  
 3023 cate on behalf of the science community, and supports  
 3024 the eight LSST Science Collaborations (§7.6).

3025 All of the resources for scientists that are discussed in  
 3026 this section are discoverable by browsing the *For Scien-*  
 3027 *tists* pages of the Rubin Observatory website<sup>106</sup>.

### 3028 7.1. Documentation

3029 The data release documentation for DP1<sup>107</sup> provides  
 3030 an overview of the LSSTComCam observations, detailed  
 3031 descriptions of the data products, and a high-level sum-  
 3032 mary of the processing pipelines. Although much of its  
 3033 content overlaps significantly with this paper, the doc-  
 3034 umentation is presented as a searchable, web-based re-  
 3035 source built using Sphinx<sup>108</sup>, with a focus on enabling  
 3036 scientific use of the data products.

### 3037 7.2. Tutorials

3038 A suite of tutorials (NSF-DOE Vera C. Rubin Ob-  
 3039 servatory 2021) that demonstrate how to access and  
 3040 analyze DP1 using the RSP accompanies the DP1 re-  
 3041 lease<sup>109</sup>. Jupyter Notebook tutorials are available via  
 3042 the “Tutorials” drop-down menu within the Notebook  
 3043 aspect of the RSP. Tutorials for the Portal and API  
 3044 aspects of the RSP can be found in the data release  
 3045 documentation.

3046 These tutorials are designed to be inclusive, accessi-  
 3047 ble, clear, focused, and consistent. Their format and  
 3048 contents follow a set of guidelines (M. L. Graham et al.  
 3049 2026) that are informed by modern standards in techni-  
 3050 cal writing.

### 3051 7.3. Community Forum

3052 The venue for all user support is the Rubin Commu-  
 3053 nity Forum<sup>110</sup>. Questions about any and all aspects of  
 3054 the Rubin data products, pipelines, and services, includ-  
 3055 ing DP1, should be posted as new topics in the Support  
 3056 category. This includes beginner-level and “how-to”  
 3057 questions, advanced scientific analysis questions, techni-  
 3058 cal bug reports, account and data access issues, and  
 3059 everything in between. The Support category of the Fo-  
 3060 rum is monitored by Rubin staff, who follow an estab-  
 3061 lished internal workflow for following-up and resolving  
 3062 all reported issues.

<sup>106</sup> <https://rubinobservatory.org/for-scientists>

<sup>107</sup> <https://dp1.lsst.io>

<sup>108</sup> <https://www.sphinx-doc.org/>

<sup>109</sup> <https://dp1.lsst.io/tutorials>

<sup>110</sup> <https://community.lsst.org/>

The Rubin Community Forum is built on the open-source Discourse platform. It was chosen because, for a worldwide community of ten thousand Rubin users, a traditional (i.e., closed) help desk represents a risk to Rubin science (e.g., many users with the same question having to wait for responses). The open nature of the Forum enables self-help by letting users search for similar issues, and enables crowd-sourced problem solving (and avoids knowledge bottlenecks) by letting users help users.

The Rubin Community Forum, and the internal staff workflows for user support, were set up, tested, and refined with DP0 so that it was ready for use with DP1.

#### 7.4. Engagement Activities

A variety of live virtual and in-person workshops and seminars offer learning opportunities to scientists and students working with the Rubin data products, services, and tools.

- Rubin Science Assemblies (weekly, virtual, 1 hour): alternates between hands-on tutorials based on the most recent data release and open drop-in “office hours” with Rubin staff.
- Rubin Data Academy (annual, virtual, 3-4 days): an intense set of hands-on tutorials based on the most recent data release, along with co-working and networking sessions.
- Rubin Community Workshop (annual, virtual, 5 days), a science-focused conference of contributed posters, talks, and sessions led by members of the Rubin science community and Rubin staff.

Following the release of DP1, all of these engagement activities focused on use of DP1 by the science community. In particular, the 2025 Rubin Data Academy was run the week of the DP1 release, in order to immediately facilitate community access. The 2025 Rubin Community Workshop had several sessions to introduce people to the DP1 dataset and demonstrate how to access and analyze it with the RSP.

For schedules, connection information, zoom recordings, and associated materials, visit the *For Scientists* pages of the Rubin Observatory website<sup>111</sup>. Requests for custom tutorials and presentations for research groups are also accommodated.

#### 7.5. Users Committee

This committee is charged with soliciting feedback from the science community, advocating on their behalf,

and recommending science-driven improvements to the LSST data products and the Rubin Science Platform tools and services. Community members are encouraged to attend their virtual meetings and raise issues to their attention, so they can be included in the committee’s twice-yearly reports to the Rubin Observatory Director.

Like the Forum, the Users Committee was established and began its work with DP0, and that feedback was implemented for DP1. The community’s response to DP1 will be especially valuable input to DP2 and DR1, and the Users Committee encourages all users to interact with them. For a list of members and contact information, visit the *For Scientists* pages of the Rubin Observatory website.

#### 7.6. Science Collaborations

The eight LSST Science Collaborations are independent, worldwide communities of scientists, self-organized into collaborations based on their research interests and expertise. Members work together to apply for funding, build software infrastructure and analysis algorithms, and incorporate external data sets into their LSST-based research.

The Science Collaborations also provide valuable advice to Rubin Observatory on the operational strategies and data products to accomplish specific science goals, and Rubin Observatory supports the collaborations via staff liaisons and regular virtual meetings with Rubin operations leadership.

The Science Collaborations have been functioning for many years, and their engagement and feedback on DP0 was implemented into the community science model for DP1, as it will for future data releases.

## 8. SUMMARY AND FUTURE RELEASES

Rubin Data Preview 1 offers an initial look at the first on-sky data products and access services from the Vera C. Rubin Observatory. DP1 forms part of Rubin’s Early Science Program, and provides the scientific community with an early opportunity to familiarize themselves with the data formats and access infrastructure for the forthcoming Legacy Survey of Space and Time. This early release has a proprietary period of two years, during which time it is available to Rubin data rights holders only via the cloud-based RSP.

In this paper we have described the completion status of the observatory at the time of data acquisition, the commissioning campaign that forms the basis of DP1, and the processing pipelines used to produce early versions of data products. We provide details on the data products, their characteristics and known issues, and

<sup>111</sup> <https://rubinobservatory.org/for-scientists/events-deadlines>

3159 describe the Rubin Science Platform for access to and  
3160 analysis of DP1.

3161 The data products described in this paper derive from  
3162 observations obtained by LSSTComCam. LSSTCom-  
3163 Cam contains only around 5% the number of CCDs as  
3164 the full LSST Science Camera (LSSTCam), yet the DP1  
3165 dataset that it has produced will already enable a very  
3166 broad range of science. At 3.5 TB in size, DP1 covers  
3167 a total area of  $\sim 15$  deg<sup>2</sup> and contains 1792 single-epoch  
3168 images, 2644 deep coadded images and 2.3 million dis-  
3169 tinct astrophysical objects, including 93 new asteroid  
3170 discoveries.

3171 While some data products anticipated from the LSST  
3172 are not yet available, e.g., cell-based coadds, DP1 in-  
3173 cludes several products that will not be provided in fu-  
3174 ture releases. Notably, difference images are included in  
3175 DP1 as pre-generated products; in future releases, these  
3176 will instead be generated on demand via dedicated ser-  
3177 vices. The inclusion of pre-generated difference images  
3178 in DP1 is feasible due to the relatively small size of the  
3179 dataset, an approach that will not scale to the signifi-  
3180 cantly larger data volumes expected in subsequent re-  
3181 leases.

3182 The RSP is continually under development, and new  
3183 functionality will continue to be deployed incrementally  
3184 as it becomes available, and independent of the future  
3185 data release schedule. User query history capabilities,  
3186 context-aware documentation and a bulk cutout services  
3187 are just a few of the services currently under develop-  
3188 ment.

3189 Coincident with the release of DP1, Rubin Obser-  
3190 vatory begins its Science Validation Surveys with the  
3191 LSST Science Camera (i.e., LSSTCam). This final com-  
3192 missioning phase will produce a dataset that will form  
3193 the foundation for the second Rubin Data Preview, DP2.  
3194 Full operations, marking the start of the LSST, are ex-  
3195 pected to commence in 2026.

## ACKNOWLEDGMENTS

3197 . This material is based upon work supported in part by  
3198 the National Science Foundation through Cooperative  
3199 Agreements AST-1258333 and AST-2241526 and Co-  
3200 operative Support Agreements AST-1202910 and AST-  
3201 2211468 managed by the Association of Universities for  
3202 Research in Astronomy (AURA), and the Department of  
3203 Energy under Contract No. DE-AC02-76SF00515 with  
3204 the SLAC National Accelerator Laboratory managed  
3205 by Stanford University. Additional Rubin Observatory  
3206 funding comes from private donations, grants to univer-  
3207 sities, and in-kind support from LSST-DA Institutional  
3208 Members.

3209 This work has been supported by the French Na-  
3210 tional Institute of Nuclear and Particle Physics (IN2P3)  
3211 through dedicated funding provided by the National  
3212 Center for Scientific Research (CNRS).

3213 This work has been supported by STFC fund-  
3214 ing for UK participation in LSST, through grant  
3215 ST/Y00292X/1.

3216 *Facilities:* Rubin:Simonyi (LSSTComCam), Ru-  
3217 bin:USDAC

3218 *Software:* Rubin Data Butler (T. Jenness et al.  
3219 2022), LSST Science Pipelines (Rubin Observatory Sci-  
3220 ence Pipelines Developers 2025), LSST Feature Based  
3221 Scheduler v3.0 (P. Yoachim et al. 2024; E. Naghib et al.  
3222 2019) Astropy (Astropy Collaboration et al. 2013, 2018,  
3223 2022) PIFF (M. Jarvis et al. 2021), GBDES (G. M.  
3224 Bernstein 2022), Qserv (D. L. Wang et al. 2011; F.  
3225 Mueller et al. 2023), Slurm, HTCondor, CVMFS, FTS3,  
3226 ESNNet

## APPENDIX

## REFERENCES

- 3228 Abazajian, K., Adelman-McCarthy, J. K., Agüeros, M. A.,  
3229 et al. 2004, AJ, 128, 502, doi: [10.1086/421365](https://doi.org/10.1086/421365)
- 3230 Ahumada, R., Allende Prieto, C., Almeida, A., et al. 2020,  
3231 ApJS, 249, 3, doi: [10.3847/1538-4365/ab929e](https://doi.org/10.3847/1538-4365/ab929e)
- 3232 Aihara, H., AlSayyad, Y., Ando, M., et al. 2022, PASJ, 74,  
3233 247, doi: [10.1093/pasj/psab122](https://doi.org/10.1093/pasj/psab122)
- 3234 Allbery, R. 2023, IVOA SODA implementation experience,  
3235 SQuARE Technical Note SQR-063, NSF-DOE Vera C.  
3236 Rubin Observatory. <https://sqr-063.lsst.io/>
- 3237 Allbery, R. 2024, Draft IVOA SODA web service  
3238 specification, SQuARE Technical Note SQR-093,  
3239 NSF-DOE Vera C. Rubin Observatory.  
3240 <https://sqr-093.lsst.io/>

- 3241 AlSayyad, Y. 2018, Coaddition Artifact Rejection and  
3242 CompareWarp, Data Management Technical Note  
3243 DMTN-080, NSF-DOE Vera C. Rubin Observatory,  
3244 doi: [10.71929/rubin/2583441](https://doi.org/10.71929/rubin/2583441)
- 3245 Ansel, J., Yang, E., He, H., et al. 2024, in 29th ACM  
3246 International Conference on Architectural Support for  
3247 Programming Languages and Operating Systems, Volume  
3248 2 (ASPLOS '24) (ACM), doi: [10.1145/3620665.3640366](https://doi.org/10.1145/3620665.3640366)
- 3249 Antilogus, P., Astier, P., Doherty, P., Guyonnet, A., &  
3250 Regnault, N. 2014, *Journal of Instrumentation*, 9,  
3251 C03048, doi: [10.1088/1748-0221/9/03/C03048](https://doi.org/10.1088/1748-0221/9/03/C03048)
- 3252 Astropy Collaboration, Robitaille, T. P., Tollerud, E. J.,  
3253 et al. 2013, *A&A*, 558, A33,  
3254 doi: [10.1051/0004-6361/201322068](https://doi.org/10.1051/0004-6361/201322068)
- 3255 Astropy Collaboration, Price-Whelan, A. M., Sipőcz, B. M.,  
3256 et al. 2018, *AJ*, 156, 123, doi: [10.3847/1538-3881/aabc4f](https://doi.org/10.3847/1538-3881/aabc4f)
- 3257 Astropy Collaboration, Price-Whelan, A. M., Lim, P. L.,  
3258 et al. 2022, *ApJ*, 935, 167, doi: [10.3847/1538-4357/ac7c74](https://doi.org/10.3847/1538-4357/ac7c74)
- 3259 Baumann, M., Boch, T., Pineau, F.-X., et al. 2022, in  
3260 *Astronomical Society of the Pacific Conference Series*,  
3261 Vol. 532, *Astronomical Data Analysis Software and*  
3262 *Systems XXX*, ed. J. E. Ruiz, F. Pierfederici, &  
3263 P. Teuben, 7
- 3264 Bechtol, K., Sevilla-Noarbe, I., Drlica-Wagner, A., et al.  
3265 2025, arXiv e-prints, arXiv:2501.05739,  
3266 doi: [10.48550/arXiv.2501.05739](https://doi.org/10.48550/arXiv.2501.05739)
- 3267 Berk, A., Anderson, G. P., Bernstein, L. S., et al. 1999, in  
3268 *Society of Photo-Optical Instrumentation Engineers*  
3269 *(SPIE) Conference Series*, Vol. 3756, *Optical*  
3270 *Spectroscopic Techniques and Instrumentation for*  
3271 *Atmospheric and Space Research III*, ed. A. M. Larar,  
3272 348–353, doi: [10.1117/12.366388](https://doi.org/10.1117/12.366388)
- 3273 Bernstein, G. M. 2022, gbdes: DECam instrumental  
3274 signature fitting and processing programs,, *Astrophysics*  
3275 *Source Code Library*, record ascl:2210.011  
3276 <http://ascl.net/2210.011>
- 3277 Bernstein, G. M., & Jarvis, M. 2002, *AJ*, 123, 583,  
3278 doi: [10.1086/338085](https://doi.org/10.1086/338085)
- 3279 Bernstein, G. M., Armstrong, R., Plazas, A. A., et al. 2017,  
3280 *PASP*, 129, 074503, doi: [10.1088/1538-3873/aa6c55](https://doi.org/10.1088/1538-3873/aa6c55)
- 3281 Bertin, E. 2011, in *Astronomical Society of the Pacific*  
3282 *Conference Series*, Vol. 442, *Astronomical Data Analysis*  
3283 *Software and Systems XX*, ed. I. N. Evans,  
3284 A. Accomazzi, D. J. Mink, & A. H. Rots, 435
- 3285 Bianco, F. B., Ivezić, Ž., Jones, R. L., et al. 2022, *ApJS*,  
3286 258, 1, doi: [10.3847/1538-4365/ac3e72](https://doi.org/10.3847/1538-4365/ac3e72)
- 3287 Blum, R., & the Rubin Operations Team. 2020, Vera C.  
3288 Rubin Observatory Data Policy, Data Management  
3289 Operations Controlled Document RDO-013, NSF-DOE  
3290 Vera C. Rubin Observatory. <https://ls.st/RDO-013>
- 3291 Boch, T., & Fernique, P. 2014, in *Astronomical Society of*  
3292 *the Pacific Conference Series*, Vol. 485, *Astronomical*  
3293 *Data Analysis Software and Systems XXIII*, ed.  
3294 N. Manset & P. Forshay, 277
- 3295 Bonnarel, F., Dowler, P., Demleitner, M., Tody, D., &  
3296 Dempsey, J. 2017, IVOA Server-side Operations for Data  
3297 Access Version 1.0., IVOA Recommendation 17 May 2017  
3298 doi: [10.5479/ADS/bib/2017ivoa.spec.0517B](https://doi.org/10.5479/ADS/bib/2017ivoa.spec.0517B)
- 3299 Bonnarel, F., Fernique, P., Bienaymé, O., et al. 2000,  
3300 *A&AS*, 143, 33, doi: [10.1051/aas:2000331](https://doi.org/10.1051/aas:2000331)
- 3301 Bosch, J., Armstrong, R., Bickerton, S., et al. 2018, *PASJ*,  
3302 70, S5, doi: [10.1093/pasj/psx080](https://doi.org/10.1093/pasj/psx080)
- 3303 Broughton, A., Utsumi, Y., Plazas Malagón, A. A., et al.  
3304 2024, *PASP*, 136, 045003, doi: [10.1088/1538-3873/ad3aa2](https://doi.org/10.1088/1538-3873/ad3aa2)
- 3305 Burke, D. L., Rykoff, E. S., Allam, S., et al. 2018, *AJ*, 155,  
3306 41, doi: [10.3847/1538-3881/aa9f22](https://doi.org/10.3847/1538-3881/aa9f22)
- 3307 Chambers, K. C., Magnier, E. A., Metcalfe, N., et al. 2016,  
3308 arXiv e-prints, arXiv:1612.05560,  
3309 doi: [10.48550/arXiv.1612.05560](https://doi.org/10.48550/arXiv.1612.05560)
- 3310 Choi, Y., Olsen, K. A. G., Carlin, J. L., et al. 2025, arXiv  
3311 e-prints, arXiv:2507.01343,  
3312 doi: [10.48550/arXiv.2507.01343](https://doi.org/10.48550/arXiv.2507.01343)
- 3313 de Vaucouleurs, G. 1948, *Annales d'Astrophysique*, 11, 247
- 3314 de Vaucouleurs, G. 1953, *MNRAS*, 113, 134,  
3315 doi: [10.1093/mnras/113.2.134](https://doi.org/10.1093/mnras/113.2.134)
- 3316 Dowler, P., Bonnarel, F., & Tody, D. 2015, IVOA Simple  
3317 Image Access Version 2.0., IVOA Recommendation 23  
3318 December 2015  
3319 doi: [10.5479/ADS/bib/2015ivoa.spec.1223D](https://doi.org/10.5479/ADS/bib/2015ivoa.spec.1223D)
- 3320 Dowler, P., Rixon, G., Tody, D., & Demleitner, M. 2019,  
3321 Table Access Protocol Version 1.1., IVOA  
3322 Recommendation 27 September 2019  
3323 doi: [10.5479/ADS/bib/2019ivoa.spec.0927D](https://doi.org/10.5479/ADS/bib/2019ivoa.spec.0927D)
- 3324 Eggl, S., Juric, M., Moeyens, J., & Jones, L. 2020, in  
3325 *AAS/Division for Planetary Sciences Meeting Abstracts*,  
3326 Vol. 52, *AAS/Division for Planetary Sciences Meeting*  
3327 *Abstracts*, 211.01
- 3328 Esteves, J. H., Utsumi, Y., Snyder, A., et al. 2023, *PASP*,  
3329 135, 115003, doi: [10.1088/1538-3873/ad0a73](https://doi.org/10.1088/1538-3873/ad0a73)
- 3330 Euclid Collaboration, Romelli, E., Kümmel, M., et al. 2025,  
3331 arXiv e-prints, arXiv:2503.15305,  
3332 doi: [10.48550/arXiv.2503.15305](https://doi.org/10.48550/arXiv.2503.15305)
- 3333 Fagrelus, P., & Rykoff, E. S. 2025, Rubin Observatory  
3334 Baseline Calibration Plan, Commissioning Technical  
3335 Note SITCOMTN-086, NSF-DOE Vera C. Rubin  
3336 Observatory, doi: [10.71929/rubin/2583850](https://doi.org/10.71929/rubin/2583850)

- 3337 Ferguson, P. S., Rykoff, E. S., Carlin, J. L., Saunders, C., &  
3338 Parejko, J. K. 2025, The Monster: A reference catalog  
3339 with synthetic ugrizy-band fluxes for the Vera C. Rubin  
3340 observatory, Data Management Technical Note  
3341 DMTN-277, NSF-DOE Vera C. Rubin Observatory,  
3342 doi: [10.71929/rubin/2583688](https://doi.org/10.71929/rubin/2583688)
- 3343 Fernique, P., Allen, M. G., Boch, T., et al. 2015, *A&A*, 578,  
3344 A114, doi: [10.1051/0004-6361/201526075](https://doi.org/10.1051/0004-6361/201526075)
- 3345 Fernique, P., Allen, M., Boch, T., et al. 2017, HiPS -  
3346 Hierarchical Progressive Survey Version 1.0., IVOA  
3347 Recommendation 19 May 2017  
3348 doi: [10.5479/ADS/bib/2017ivoa.spec.0519F](https://doi.org/10.5479/ADS/bib/2017ivoa.spec.0519F)
- 3349 Fortino, W. F., Bernstein, G. M., Bernardinelli, P. H., et al.  
3350 2021, *AJ*, 162, 106, doi: [10.3847/1538-3881/ac0722](https://doi.org/10.3847/1538-3881/ac0722)
- 3351 Gaia Collaboration, Montegriffo, P., Bellazzini, M., et al.  
3352 2023a, *A&A*, 674, A33,  
3353 doi: [10.1051/0004-6361/202243709](https://doi.org/10.1051/0004-6361/202243709)
- 3354 Gaia Collaboration, Vallenari, A., Brown, A. G. A., et al.  
3355 2023b, *A&A*, 674, A1, doi: [10.1051/0004-6361/202243940](https://doi.org/10.1051/0004-6361/202243940)
- 3356 Górski, K. M., Hivon, E., Banday, A. J., et al. 2005, *ApJ*,  
3357 622, 759, doi: [10.1086/427976](https://doi.org/10.1086/427976)
- 3358 Graham, A. W., & Driver, S. P. 2005, *PASA*, 22, 118,  
3359 doi: [10.1071/AS05001](https://doi.org/10.1071/AS05001)
- 3360 Graham, M., Plante, R., Tody, D., & Fitzpatrick, M. 2014,  
3361 PyVO: Python access to the Virtual Observatory,,  
3362 Astrophysics Source Code Library, record ascl:1402.004
- 3363 Graham, M. L., Carlin, J. L., Adair, C. L., et al. 2026,  
3364 Guidelines for User Tutorials, Technical Note RTN-045,  
3365 NSF-DOE Vera C. Rubin Observatory,  
3366 doi: [10.71929/rubin/2584020](https://doi.org/10.71929/rubin/2584020)
- 3367 Gray, B. 2025, find\_orb: Orbit determination from  
3368 observations, [https://github.com/Bill-Gray/find\\_orb](https://github.com/Bill-Gray/find_orb)
- 3369 Guy, L. P., Bechtol, K., Bellm, E., et al. 2026, Rubin  
3370 Observatory Plans for an Early Science Program,  
3371 Technical Note RTN-011, NSF-DOE Vera C. Rubin  
3372 Observatory, doi: [10.71929/rubin/2584021](https://doi.org/10.71929/rubin/2584021)
- 3373 Heinze, A., Eggl, S., Juric, M., et al. 2022, in *AAS/Division*  
3374 *for Planetary Sciences Meeting Abstracts*, Vol. 54,  
3375 *AAS/Division for Planetary Sciences Meeting Abstracts*,  
3376 504.04
- 3377 Heinze, A., Juric, M., & Kurlander, J. 2023, helioliinx: Open  
3378 Source Solar System Discovery Software,  
3379 <https://github.com/helioliinx/helioliinx>
- 3380 Hirata, C., & Seljak, U. 2003, *MNRAS*, 343, 459,  
3381 doi: [10.1046/j.1365-8711.2003.06683.x](https://doi.org/10.1046/j.1365-8711.2003.06683.x)
- 3382 Holman, M. J., Payne, M. J., Blankley, P., Janssen, R., &  
3383 Kuindersma, S. 2018, *AJ*, 156, 135,  
3384 doi: [10.3847/1538-3881/aad69a](https://doi.org/10.3847/1538-3881/aad69a)
- 3385 Howard, J., Reil, K., Claver, C., et al. 2018, in *Society of*  
3386 *Photo-Optical Instrumentation Engineers (SPIE)*  
3387 *Conference Series*, Vol. 10700, *Ground-based and*  
3388 *Airborne Telescopes VII*, ed. H. K. Marshall &  
3389 J. Spyromilio, 107003D, doi: [10.1117/12.2312684](https://doi.org/10.1117/12.2312684)
- 3390 Illingworth, G., Magee, D., Bouwens, R., et al. 2016, arXiv  
3391 e-prints, arXiv:1606.00841,  
3392 doi: [10.48550/arXiv.1606.00841](https://doi.org/10.48550/arXiv.1606.00841)
- 3393 Ingraham, P., Fagrelis, P., Stubbs, C. W., et al. 2022, in  
3394 *Society of Photo-Optical Instrumentation Engineers*  
3395 *(SPIE) Conference Series*, Vol. 12182, *Ground-based and*  
3396 *Airborne Telescopes IX*, ed. H. K. Marshall,  
3397 J. Spyromilio, & T. Usuda, 121820R,  
3398 doi: [10.1117/12.2630185](https://doi.org/10.1117/12.2630185)
- 3399 Ivezić, Ž., Kahn, S. M., Tyson, J. A., et al. 2019a, *ApJ*,  
3400 873, 111, doi: [10.3847/1538-4357/ab042c](https://doi.org/10.3847/1538-4357/ab042c)
- 3401 Ivezić, Ž., Kahn, S. M., Tyson, J. A., et al. 2019b, *ApJ*,  
3402 873, 111, doi: [10.3847/1538-4357/ab042c](https://doi.org/10.3847/1538-4357/ab042c)
- 3403 Jarvis, M., et al. 2021, *Mon. Not. Roy. Astron. Soc.*, 501,  
3404 1282, doi: [10.1093/mnras/staa3679](https://doi.org/10.1093/mnras/staa3679)
- 3405 Jenness, T., & Dubois-Felsmann, G. P. 2025, IVOA  
3406 Identifier Usage at the Rubin Observatory, Data  
3407 Management Technical Note DMTN-302, NSF-DOE Vera  
3408 C. Rubin Observatory, doi: [10.71929/rubin/2583848](https://doi.org/10.71929/rubin/2583848)
- 3409 Jenness, T., Voutsinas, S., Dubois-Felsmann, G. P., &  
3410 Salnikov, A. 2024, arXiv e-prints, arXiv:2501.00544,  
3411 doi: [10.48550/arXiv.2501.00544](https://doi.org/10.48550/arXiv.2501.00544)
- 3412 Jenness, T., Bosch, J. F., Salnikov, A., et al. 2022, in  
3413 *Society of Photo-Optical Instrumentation Engineers*  
3414 *(SPIE) Conference Series*, Vol. 12189, *Software and*  
3415 *Cyberinfrastructure for Astronomy VII*, 1218911,  
3416 doi: [10.1117/12.2629569](https://doi.org/10.1117/12.2629569)
- 3417 Jones, R. L., Yoachim, P., Ivezić, Ž., Neilsen Jr., E. H., &  
3418 Ribeiro, T. 2021, Survey Strategy and Cadence Choices  
3419 for the Vera C. Rubin Observatory Legacy Survey of  
3420 Space and Time (LSST), Project Science Technical Note  
3421 PSTN-051, NSF-DOE Vera C. Rubin Observatory,  
3422 doi: [10.71929/rubin/2584084](https://doi.org/10.71929/rubin/2584084)
- 3423 Juric, M. 2025, mpsky: Multi-purpose sky catalog  
3424 cross-matching, <https://github.com/mjuric/mpsky>
- 3425 Jurić, M., Ciardi, D., Dubois-Felsmann, G., & Guy, L.  
3426 2019, LSST Science Platform Vision Document, Systems  
3427 Engineering Controlled Document LSE-319, NSF-DOE  
3428 Vera C. Rubin Observatory, doi: [10.71929/rubin/2587242](https://doi.org/10.71929/rubin/2587242)
- 3429 Jurić, M., Axelrod, T. S., Becker, A. C., et al. 2023, Data  
3430 Products Definition Document, Systems Engineering  
3431 Controlled Document LSE-163, NSF-DOE Vera C. Rubin  
3432 Observatory, doi: [10.71929/rubin/2587118](https://doi.org/10.71929/rubin/2587118)

- 3433 Kannawadi, A. 2025, Consistent galaxy colors with  
3434 Gaussian-Aperture and PSF photometry, Data  
3435 Management Technical Note DMTN-190, NSF-DOE Vera  
3436 C. Rubin Observatory, doi: [10.71929/rubin/2583849](https://doi.org/10.71929/rubin/2583849)
- 3437 Kron, R. G. 1980, *ApJS*, 43, 305, doi: [10.1086/190669](https://doi.org/10.1086/190669)
- 3438 Kuijken, K. 2008, *A&A*, 482, 1053,  
3439 doi: [10.1051/0004-6361:20066601](https://doi.org/10.1051/0004-6361:20066601)
- 3440 Lange, T., Nordby, M., Pollek, H., et al. 2024, in *Society of  
3441 Photo-Optical Instrumentation Engineers (SPIE)  
3442 Conference Series*, Vol. 13096, Ground-based and  
3443 Airborne Instrumentation for Astronomy X, ed. J. J.  
3444 Bryant, K. Motohara, & J. R. D. Vernet, 130961O,  
3445 doi: [10.1117/12.3019302](https://doi.org/10.1117/12.3019302)
- 3446 Léget, P. F., Astier, P., Regnault, N., et al. 2021, *A&A*,  
3447 650, A81, doi: [10.1051/0004-6361/202140463](https://doi.org/10.1051/0004-6361/202140463)
- 3448 Lim, K.-T. 2023, Proposal and Prototype for Prompt  
3449 Processing, Data Management Technical Note  
3450 DMTN-219, NSF-DOE Vera C. Rubin Observatory,  
3451 doi: [10.71929/rubin/2585429](https://doi.org/10.71929/rubin/2585429)
- 3452 Louys, M., Tody, D., Dowler, P., et al. 2017, Observation  
3453 Data Model Core Components, its Implementation in the  
3454 Table Access Protocol Version 1.1., IVOA  
3455 Recommendation 09 May 2017  
3456 doi: [10.5479/ADS/bib/2017ivoa.spec.0509L](https://doi.org/10.5479/ADS/bib/2017ivoa.spec.0509L)
- 3457 LSST Dark Energy Science Collaboration (LSST DESC),  
3458 Abolfathi, B., Alonso, D., et al. 2021, *ApJS*, 253, 31,  
3459 doi: [10.3847/1538-4365/abd62c](https://doi.org/10.3847/1538-4365/abd62c)
- 3460 Lupton, R., Blanton, M. R., Fekete, G., et al. 2004, *PASP*,  
3461 116, 133, doi: [10.1086/382245](https://doi.org/10.1086/382245)
- 3462 Lust, N. B., Jenness, T., Bosch, J. F., et al. 2023, *arXiv  
3463 e-prints*, arXiv:2303.03313,  
3464 doi: [10.48550/arXiv.2303.03313](https://doi.org/10.48550/arXiv.2303.03313)
- 3465 Mandelbaum, R., Hirata, C. M., Seljak, U., et al. 2005,  
3466 *MNRAS*, 361, 1287,  
3467 doi: [10.1111/j.1365-2966.2005.09282.x](https://doi.org/10.1111/j.1365-2966.2005.09282.x)
- 3468 Megias Homar, G., Kahn, S. M., Meyers, J. M., Crenshaw,  
3469 J. F., & Thomas, S. J. 2024, *The Astrophysical Journal*,  
3470 974, 108, doi: [10.3847/1538-4357/ad6cdc](https://doi.org/10.3847/1538-4357/ad6cdc)
- 3471 Megias Homar, G., Tighe, R., Thomas, S., et al. 2024, in  
3472 *Ground-based and Airborne Telescopes X*, ed. H. K.  
3473 Marshall, J. Spyromilio, & T. Usuda, Vol. 13094,  
3474 *International Society for Optics and Photonics (SPIE)*,  
3475 130943C, doi: [10.1117/12.3019031](https://doi.org/10.1117/12.3019031)
- 3476 Melchior, P., Moolekamp, F., Jerdee, M., et al. 2018,  
3477 *Astronomy and Computing*, 24, 129,  
3478 doi: [10.1016/j.ascom.2018.07.001](https://doi.org/10.1016/j.ascom.2018.07.001)
- 3479 Mueller, F., et al. 2023, in *ASP Conf. Ser.*, Vol. TBD,  
3480 *ADASS XXXII*, ed. S. Gaudet, S. Gwyn, P. Dowler,  
3481 D. Bohlender, & A. Hincks (San Francisco: ASP), in  
3482 press. <https://dmtn-243.lsst.io>
- 3483 Naghib, E., Yoachim, P., Vanderbei, R. J., Connolly, A. J.,  
3484 & Jones, R. L. 2019, *The Astronomical Journal*, 157, 151,  
3485 doi: [10.3847/1538-3881/aafece](https://doi.org/10.3847/1538-3881/aafece)
- 3486 NSF-DOE Vera C. Rubin Observatory. 2021, *Rubin  
3487 Observatory LSST Tutorials [Computer Software]*,  
3488 NSF-DOE Vera C. Rubin Observatory,  
3489 doi: [10.11578/rubin/dc.20250909.20](https://doi.org/10.11578/rubin/dc.20250909.20)
- 3490 NSF-DOE Vera C. Rubin Observatory. 2025a, *Legacy  
3491 Survey of Space and Time Data Preview 1 [Data set]*,  
3492 NSF-DOE Vera C. Rubin Observatory,  
3493 doi: [10.71929/RUBIN/2570308](https://doi.org/10.71929/RUBIN/2570308)
- 3494 NSF-DOE Vera C. Rubin Observatory. 2025b, *Legacy  
3495 Survey of Space and Time Data Preview 1: raw dataset  
3496 type [Data set]*, NSF-DOE Vera C. Rubin Observatory,  
3497 doi: [10.71929/RUBIN/2570310](https://doi.org/10.71929/RUBIN/2570310)
- 3498 NSF-DOE Vera C. Rubin Observatory. 2025c, *Legacy  
3499 Survey of Space and Time Data Preview 1: visit\_image  
3500 dataset type [Data set]*, NSF-DOE Vera C. Rubin  
3501 Observatory, doi: [10.71929/RUBIN/2570311](https://doi.org/10.71929/RUBIN/2570311)
- 3502 NSF-DOE Vera C. Rubin Observatory. 2025d, *Legacy  
3503 Survey of Space and Time Data Preview 1:  
3504 template\_coadd dataset type [Data set]*, NSF-DOE Vera  
3505 C. Rubin Observatory, doi: [10.71929/RUBIN/2570314](https://doi.org/10.71929/RUBIN/2570314)
- 3506 NSF-DOE Vera C. Rubin Observatory. 2025e, *Legacy  
3507 Survey of Space and Time Data Preview 1:  
3508 difference\_image dataset type [Data set]*, NSF-DOE Vera  
3509 C. Rubin Observatory, doi: [10.71929/RUBIN/2570312](https://doi.org/10.71929/RUBIN/2570312)
- 3510 NSF-DOE Vera C. Rubin Observatory. 2025f, *Legacy  
3511 Survey of Space and Time Data Preview 1: Source  
3512 searchable catalog [Data set]*, NSF-DOE Vera C. Rubin  
3513 Observatory, doi: [10.71929/RUBIN/2570323](https://doi.org/10.71929/RUBIN/2570323)
- 3514 NSF-DOE Vera C. Rubin Observatory. 2025g, *Legacy  
3515 Survey of Space and Time Data Preview 1: Object  
3516 searchable catalog [Data set]*, NSF-DOE Vera C. Rubin  
3517 Observatory, doi: [10.71929/RUBIN/2570325](https://doi.org/10.71929/RUBIN/2570325)
- 3518 NSF-DOE Vera C. Rubin Observatory. 2025h, *Legacy  
3519 Survey of Space and Time Data Preview 1: ForcedSource  
3520 searchable catalog [Data set]*, NSF-DOE Vera C. Rubin  
3521 Observatory, doi: [10.71929/RUBIN/2570327](https://doi.org/10.71929/RUBIN/2570327)
- 3522 NSF-DOE Vera C. Rubin Observatory. 2025i, *Legacy  
3523 Survey of Space and Time Data Preview 1: DiaSource  
3524 searchable catalog [Data set]*, NSF-DOE Vera C. Rubin  
3525 Observatory, doi: [10.71929/RUBIN/2570317](https://doi.org/10.71929/RUBIN/2570317)
- 3526 NSF-DOE Vera C. Rubin Observatory. 2025j, *Legacy  
3527 Survey of Space and Time Data Preview 1: DiaObject  
3528 searchable catalog [Data set]*, NSF-DOE Vera C. Rubin  
3529 Observatory, doi: [10.71929/RUBIN/2570319](https://doi.org/10.71929/RUBIN/2570319)

- 3530 NSF-DOE Vera C. Rubin Observatory. 2025k, Legacy  
3531 Survey of Space and Time Data Preview 1:  
3532 ForcedSourceOnDiaObject searchable catalog [Data set],  
3533 NSF-DOE Vera C. Rubin Observatory,  
3534 doi: [10.71929/RUBIN/2570321](https://doi.org/10.71929/RUBIN/2570321)
- 3535 NSF-DOE Vera C. Rubin Observatory. 2025l, Legacy  
3536 Survey of Space and Time Data Preview 1: SSOBJect  
3537 searchable catalog [Data set], NSF-DOE Vera C. Rubin  
3538 Observatory, doi: [10.71929/RUBIN/2570335](https://doi.org/10.71929/RUBIN/2570335)
- 3539 NSF-DOE Vera C. Rubin Observatory. 2025m, Legacy  
3540 Survey of Space and Time Data Preview 1: SSSource  
3541 searchable catalog [Data set], NSF-DOE Vera C. Rubin  
3542 Observatory, doi: [10.71929/RUBIN/2570333](https://doi.org/10.71929/RUBIN/2570333)
- 3543 NSF-DOE Vera C. Rubin Observatory. 2025n, Legacy  
3544 Survey of Space and Time Data Preview 1: CcdVisit  
3545 searchable catalog [Data set], NSF-DOE Vera C. Rubin  
3546 Observatory, doi: [10.71929/RUBIN/2570331](https://doi.org/10.71929/RUBIN/2570331)
- 3547 NSF-DOE Vera C. Rubin Observatory. 2025o, Legacy  
3548 Survey of Space and Time Data Preview 1: survey  
3549 property dataset type [Data set], NSF-DOE Vera C.  
3550 Rubin Observatory, doi: [10.71929/RUBIN/2570315](https://doi.org/10.71929/RUBIN/2570315)
- 3551 Oke, J. B., & Gunn, J. E. 1983, *ApJ*, 266, 713,  
3552 doi: [10.1086/160817](https://doi.org/10.1086/160817)
- 3553 O'Mullane, W., Economou, F., Huang, F., et al. 2024a, in  
3554 *Astronomical Society of the Pacific Conference Series*,  
3555 Vol. 535, *Astronomical Data Analysis Software and Systems*  
3556 XXXI, ed. B. V. Hugo, R. Van Rooyen, & O. M.  
3557 Smirnov, 227, doi: [10.48550/arXiv.2111.15030](https://doi.org/10.48550/arXiv.2111.15030)
- 3558 O'Mullane, W., AlSayyad, Y., Chiang, J., et al. 2024b, in  
3559 *Society of Photo-Optical Instrumentation Engineers*  
3560 (SPIE) Conference Series, Vol. 13101, *Software and*  
3561 *Cyberinfrastructure for Astronomy VIII*, ed. J. Ibsen &  
3562 G. Chiozzi, 131012B, doi: [10.1117/12.3018005](https://doi.org/10.1117/12.3018005)
- 3563 Onken, C. A., Wolf, C., Bessell, M. S., et al. 2019, *PASA*,  
3564 36, e033, doi: [10.1017/pasa.2019.27](https://doi.org/10.1017/pasa.2019.27)
- 3565 Park, H. Y., Nomerotski, A., & Tsybychev, D. 2017,  
3566 *Journal of Instrumentation*, 12, C05015,  
3567 doi: [10.1088/1748-0221/12/05/C05015](https://doi.org/10.1088/1748-0221/12/05/C05015)
- 3568 Petrosian, V. 1976, *ApJL*, 210, L53,  
3569 doi: [10.1086/18230110.1086/182253](https://doi.org/10.1086/18230110.1086/182253)
- 3570 Plazas, A. A., Shapiro, C., Smith, R., Huff, E., & Rhodes,  
3571 J. 2018, *Publications of the Astronomical Society of the*  
3572 *Pacific*, 130, 065004, doi: [10.1088/1538-3873/aab820](https://doi.org/10.1088/1538-3873/aab820)
- 3573 Plazas Malagón, A. A., Digel, S. W., Roodman, A.,  
3574 Broughton, A., & LSST Camera Team. 2025, *LSSTCam*  
3575 *and LSSTComCam Focal Plane Layouts*, Camera  
3576 Technical Note CTN-001, NSF-DOE Vera C. Rubin  
3577 Observatory, doi: [10.71929/rubin/2584019](https://doi.org/10.71929/rubin/2584019)
- 3578 Plazas Malagón, A. A., Waters, C., Broughton, A., et al.  
3579 2025, *Journal of Astronomical Telescopes, Instruments,*  
3580 *and Systems*, 11, 011209,  
3581 doi: [10.1117/1.JATIS.11.1.011209](https://doi.org/10.1117/1.JATIS.11.1.011209)
- 3582 Porter, M. N., Tucker, D. L., Smith, J. A., & Adair, C. L.  
3583 2026, *Photometric Transformation Relations for the*  
3584 *LSST Data Preview 1*, Technical Note RTN-099,  
3585 NSF-DOE Vera C. Rubin Observatory,  
3586 doi: [10.71929/rubin/3006074](https://doi.org/10.71929/rubin/3006074)
- 3587 Refregier, A. 2003, *ARA&A*, 41, 645,  
3588 doi: [10.1146/annurev.astro.41.111302.102207](https://doi.org/10.1146/annurev.astro.41.111302.102207)
- 3589 Reiss, D. J., & Lupton, R. H. 2016, *Implementation of*  
3590 *Image Difference Decorrelation*, Data Management  
3591 Technical Note DMTN-021, NSF-DOE Vera C. Rubin  
3592 Observatory, doi: [10.71929/rubin/2586490](https://doi.org/10.71929/rubin/2586490)
- 3593 Roodman, A., Rasmussen, A., Bradshaw, A., et al. 2024, in  
3594 *Society of Photo-Optical Instrumentation Engineers*  
3595 (SPIE) Conference Series, Vol. 13096, *Ground-based and*  
3596 *Airborne Instrumentation for Astronomy X*, ed. J. J.  
3597 Bryant, K. Motohara, & J. R. D. Vernet, 130961S,  
3598 doi: [10.1117/12.3019698](https://doi.org/10.1117/12.3019698)
- 3599 Rubin, V. C., & Ford, Jr., W. K. 1970, *ApJ*, 159, 379,  
3600 doi: [10.1086/150317](https://doi.org/10.1086/150317)
- 3601 Rubin, V. C., Ford, Jr., W. K., & Thonnard, N. 1980, *ApJ*,  
3602 238, 471, doi: [10.1086/158003](https://doi.org/10.1086/158003)
- 3603 Rubin Observatory Science Pipelines Developers. 2025, *The*  
3604 *LSST Science Pipelines Software: Optical Survey*  
3605 *Pipeline Reduction and Analysis Environment*, Project  
3606 Science Technical Note PSTN-019, NSF-DOE Vera C.  
3607 Rubin Observatory, doi: [10.71929/rubin/2570545](https://doi.org/10.71929/rubin/2570545)
- 3608 Rubin's Survey Cadence Optimization Committee, Bauer,  
3609 F. E., Brough, S., et al. 2022, *Survey Cadence*  
3610 *Optimization Committee's Phase 1 Recommendation*,  
3611 Project Science Technical Note PSTN-053, NSF-DOE  
3612 Vera C. Rubin Observatory, doi: [10.71929/rubin/2584276](https://doi.org/10.71929/rubin/2584276)
- 3613 Rubin's Survey Cadence Optimization Committee, Bauer,  
3614 F. E., Bianco, F. B., et al. 2023, *Survey Cadence*  
3615 *Optimization Committee's Phase 2 Recommendations*,  
3616 Project Science Technical Note PSTN-055, NSF-DOE  
3617 Vera C. Rubin Observatory, doi: [10.71929/rubin/2585249](https://doi.org/10.71929/rubin/2585249)
- 3618 Rubin's Survey Cadence Optimization Committee, Bianco,  
3619 F. B., Jones, R. L., et al. 2025, *Survey Cadence*  
3620 *Optimization Committee's Phase 3 Recommendations*,  
3621 Project Science Technical Note PSTN-056, NSF-DOE  
3622 Vera C. Rubin Observatory, doi: [10.71929/rubin/2585402](https://doi.org/10.71929/rubin/2585402)
- 3623 Rykoff, E. S., Tucker, D. L., Burke, D. L., et al. 2023, *arXiv*  
3624 *e-prints*, arXiv:2305.01695,  
3625 doi: [10.48550/arXiv.2305.01695](https://doi.org/10.48550/arXiv.2305.01695)

- 3626 Saunders, C. 2024, Astrometric Calibration in the LSST  
3627 Pipeline, Data Management Technical Note DMTN-266,  
3628 NSF-DOE Vera C. Rubin Observatory,  
3629 doi: [10.71929/rubin/2583846](https://doi.org/10.71929/rubin/2583846)
- 3630 Schutt, T., Jarvis, M., Roodman, A., et al. 2025, The Open  
3631 Journal of Astrophysics, 8, 26, doi: [10.33232/001c.132299](https://doi.org/10.33232/001c.132299)
- 3632 Sérsic, J. L. 1963, Boletín de la Asociación Argentina de  
3633 Astronomía La Plata Argentina, 6, 41
- 3634 Sersic, J. L. 1968, Atlas de Galaxias Australes (Cordoba,  
3635 Argentina: Observatorio Astronomico)
- 3636 Shanks, T., Metcalfe, N., Chehade, B., et al. 2015,  
3637 MNRAS, 451, 4238, doi: [10.1093/mnras/stv1130](https://doi.org/10.1093/mnras/stv1130)
- 3638 SLAC National Accelerator Laboratory, & NSF-DOE Vera  
3639 C. Rubin Observatory. 2024, LSST Commissioning  
3640 Camera, SLAC National Accelerator Laboratory (SLAC),  
3641 Menlo Park, CA (United States),  
3642 doi: [10.71929/RUBIN/2561361](https://doi.org/10.71929/RUBIN/2561361)
- 3643 Slater, C. T., Ivezić, Ž., & Lupton, R. H. 2020, AJ, 159, 65,  
3644 doi: [10.3847/1538-3881/ab6166](https://doi.org/10.3847/1538-3881/ab6166)
- 3645 Smith, G. E. 2010, Rev. Mod. Phys., 82, 2307,  
3646 doi: [10.1103/RevModPhys.82.2307](https://doi.org/10.1103/RevModPhys.82.2307)
- 3647 Stalder, B., Reil, K., Claver, C., et al. 2020, in Society of  
3648 Photo-Optical Instrumentation Engineers (SPIE)  
3649 Conference Series, Vol. 11447, Ground-based and  
3650 Airborne Instrumentation for Astronomy VIII, ed. C. J.  
3651 Evans, J. J. Bryant, & K. Motohara, 114470L,  
3652 doi: [10.1117/12.2561132](https://doi.org/10.1117/12.2561132)
- 3653 Stalder, B., Reil, K., Aguilar, C., et al. 2022, in Society of  
3654 Photo-Optical Instrumentation Engineers (SPIE)  
3655 Conference Series, Vol. 12184, Ground-based and  
3656 Airborne Instrumentation for Astronomy IX, ed. C. J.  
3657 Evans, J. J. Bryant, & K. Motohara, 121840J,  
3658 doi: [10.1117/12.2630184](https://doi.org/10.1117/12.2630184)
- 3659 Stalder, B., Munoz, F., Aguilar, C., et al. 2024, in Society  
3660 of Photo-Optical Instrumentation Engineers (SPIE)  
3661 Conference Series, Vol. 13094, Ground-based and  
3662 Airborne Telescopes X, ed. H. K. Marshall, J. Spyromilio,  
3663 & T. Usuda, 1309409, doi: [10.1117/12.3019266](https://doi.org/10.1117/12.3019266)
- 3664 Swinbank, J. D., Axelrod, T. S., Becker, A. C., et al. 2020,  
3665 Data Management Science Pipelines Design, Data  
3666 Management Controlled Document LDM-151, NSF-DOE  
3667 Vera C. Rubin Observatory, doi: [10.71929/rubin/2587108](https://doi.org/10.71929/rubin/2587108)
- 3668 Taranu, D. S. 2025, The MultiProFit astronomical source  
3669 modelling code, Data Management Technical Note  
3670 DMTN-312, NSF-DOE Vera C. Rubin Observatory,  
3671 doi: [10.71929/rubin/2584108](https://doi.org/10.71929/rubin/2584108)
- 3672 Taylor, M. 2011, TOPCAT: Tool for OPerations on  
3673 Catalogues And Tables,, Astrophysics Source Code  
3674 Library, record ascl:1101.010
- 3675 Thomas, S., Connolly, A., Crenshaw, J. F., et al. 2023, in  
3676 Adaptive Optics for Extremely Large Telescopes  
3677 (AO4ELT7), 67, doi: [10.13009/AO4ELT7-2023-069](https://doi.org/10.13009/AO4ELT7-2023-069)
- 3678 Tonry, J. L., Denneau, L., Heinze, A. N., et al. 2018, PASP,  
3679 130, 064505, doi: [10.1088/1538-3873/aabadf](https://doi.org/10.1088/1538-3873/aabadf)
- 3680 Wainer, T. M., Davenport, J. R. A., Bellm, E. C., et al.  
3681 2025, Research Notes of the American Astronomical  
3682 Society, 9, 171, doi: [10.3847/2515-5172/adecef](https://doi.org/10.3847/2515-5172/adecef)
- 3683 Wang, D. L., Monkewitz, S. M., Lim, K.-T., & Becla, J.  
3684 2011, in State of the Practice Reports, SC '11 (New  
3685 York, NY, USA: ACM), 12:1–12:11,  
3686 doi: [10.1145/2063348.2063364](https://doi.org/10.1145/2063348.2063364)
- 3687 Waters, C. Z., Magnier, E. A., Price, P. A., et al. 2020,  
3688 ApJS, 251, 4, doi: [10.3847/1538-4365/abb82b](https://doi.org/10.3847/1538-4365/abb82b)
- 3689 Whitaker, K. E., Ashas, M., Illingworth, G., et al. 2019,  
3690 ApJS, 244, 16, doi: [10.3847/1538-4365/ab3853](https://doi.org/10.3847/1538-4365/ab3853)
- 3691 Wu, X., Roby, W., Goldian, T., et al. 2019, in Astronomical  
3692 Society of the Pacific Conference Series, Vol. 521,  
3693 Astronomical Data Analysis Software and Systems  
3694 XXVI, ed. M. Molinaro, K. Shortridge, & F. Pasian, 32
- 3695 Xin, B., Claver, C., Liang, M., et al. 2015, ApOpt, 54,  
3696 9045, doi: [10.1364/AO.54.009045](https://doi.org/10.1364/AO.54.009045)
- 3697 Yoachim, P. 2022, Survey Strategy: Rolling Cadence,  
3698 Project Science Technical Note PSTN-052, NSF-DOE  
3699 Vera C. Rubin Observatory, doi: [10.71929/rubin/2584109](https://doi.org/10.71929/rubin/2584109)
- 3700 Yoachim, P., Jones, L., Eric H. Neilsen, J., & Becker, M. R.  
3701 2024, lsst/rubin\_scheduler: v3.0.0, v3.0.0 Zenodo,  
3702 doi: [10.5281/zenodo.13985198](https://doi.org/10.5281/zenodo.13985198)
- 3703 Zhang, T., Almoubayyed, H., Mandelbaum, R., et al. 2023,  
3704 MNRAS, 520, 2328, doi: [10.1093/mnras/stac3350](https://doi.org/10.1093/mnras/stac3350)